

A Measurement of Nuclear Structure Functions in the Large x Large
 Q^2 Kinematic Region in Neutrino Deep Inelastic Scattering

A dissertation submitted to the

Division of Research and Advanced Studies
of the University of Cincinnati

in partial fulfillment of the
requirements for the degree of

DOCTORATE OF PHILOSOPHY (Ph.D.)

in the Department of Physics
of the College of Arts and Sciences

1997

by

Masoud Vakili

B.S. Sharif University of Technology, 1991
M.S. University of Cincinnati, 1993

Committee Chair: Dr. Randy Johnson

Abstract

Data from the CCFR E770 Neutrino Deep Inelastic Scattering (DIS) experiment at Fermilab contain large Bjorken x , high Q^2 events. A comparison of the data with a model, based on no nuclear effects at large x , shows an excess of events in the data. Addition of Fermi gas motion of the nucleons in the nucleus to the model does not explain the model's deficit. Adding higher momentum tail due to the formation of "quasi-deuterons" makes the agreement better. Certain models based on "multi-quark clusters" and "few-nucleon correlations" predict an exponentially falling behavior for F_2 as $F_2 \sim e^{s(x-x_0)}$ at large x . We measure a $s = 8.3 \pm 0.8$ for the best fit to our data. This corresponds to a value of $F_2(x = 1, Q^2 > 50) \approx 2 \times 10^{-3}$ in neutrino DIS. These values agree with results from theoretical models and the SLAC E133 experiment but seem to be different from the result of the BCDMS experiment.

Acknowledgments

My first and foremost thank goes to my thesis advisor, Randy Johnson, for his support and guidance throughout my graduate study. Randy's deep insight into physics and analysis methods was always there when I needed it. He was quite democratic and always left the final decisions up to me in practically every issue. He read everything I wrote very many times with great patience and gave me invaluable advice and suggestions. He always made sure I make no "big mistakes". I cannot possibly count everything Randy has done to help this analysis.

I would also like to thank my thesis committee professors, Brian Meadows, Rohana Wijewardana, and Fu-Chun Zhang for their continued review and support of my work. Mike Sokoloff, though not on my committee, certainly contributed as if he were.

Mike Shaevitz was indeed my second advisor and provided me with all kinds of support whenever I needed it. Mike had three students of his own during this time. Other CCFR/NuTeV senior collaborators including Wesley Smith, Arie Bodek, Heidi Shellman, Bob Bernstein and Tim Bolton were always helpful and encouraging. Wesley and Arie provided invaluable input to this analysis. Mike and Heidi volunteered to write letters of recommendation for me. They both read and commented on my thesis. Bob helped me out in many ways including helping to make my parents trip to the U.S. possible. Tim's clear advice was very useful in many occasions.

I had the pleasure of working with Bob Drucker, Janet Conrad, and Donna Naples on different projects and gained valuable experience. Other postdocs, Lucy de Bar-

baro, Debbie Harris, Kevin McFarland, Panagiotis Spentzouris, and Jae Yu were very nice and helped me in different ways. Fellow graduate students John Kim, Cindy McNulty, Alex Romosan, and Un-ki Yang were very helpful. We were of the same generation and shared vast amounts of information. Later on, Todd Adams, Sergey Avvakumov, Dave Mason, Artur Vaitaitis, Vincent Wu, and Sam Zeller joined NuTeV and I enjoyed working with them.

I appreciated the help provided by the Fermilab technicians, Ken Gray, Andy Lathrop, Chris Richardson, Jerry Sasak, and Jeanie Wilson during my graduate studies. Their experience and expertise helped on many occasions.

I benefited a lot from the work of previous CCFR students, Carlos Arroyo, Andrew Bazarko, Bruce King, Wing-Cheong Leung, Paul Quintas, and particularly Bill Seligman.

On the personal side I am most grateful to my family for their support in Iran and encouraging me for graduate study in the States. It was great to have my sister, Margrit, and her family here in the States. Every now and then I went to visit them and together we observed many Kurdish and Iranian celebrations. My aunts and cousins in D.C. were always kind and supportive. My friends from Sharif University of Technology, Ali, Ashkan, Niki and Reza always kept in touch with me and boosted my morale. Toward the end of my study, thanks to Simin, I got to know a few more friends (“geedar”) from Chicago and elsewhere and our get togethers were great fun.

Finally I would like to thank Rozita for giving me the final boosts that I really

needed to finish this thesis. Getting to know her was certainly a great blessing to me.

During my study I went to other countries for conferences and vacations. Although it was very hard for me to get a visa and I faced some harsh treatments, no one treated me as humanistic and fair as the Canadians. I would like to thank the people and the government of Canada for that.

Contents

1	Introduction	1
1.1	The Standard Model	1
1.2	Deep Inelastic Scattering	3
1.3	Nuclear Effects on DIS	4
2	Theoretical Background	7
2.1	Neutrino DIS Cross Section	7
2.2	The Quark-Parton Model (QPM)	13
2.2.1	Helicity and y Distributions in Center of Momentum Frame	14
2.3	QPM and the Bjorken Scaling Variable, x	16
2.3.1	QPM and Structure Functions	17
2.4	Large x Kinematic Region	24
2.5	Models for High x Structure	26
2.5.1	Fermi Motion	27
2.5.2	Few Nucleon Correlation (FNC)	29
2.5.3	Multi-quark Clusters(Bags)	31
3	Experimental Apparatus	34
3.1	Overview	34
3.2	Fermilab Tevatron	34
3.2.1	Fermilab Neutrino Beam Line	37

3.3	CCFR Detector	39
3.4	Target Calorimeter	40
3.4.1	Scintillation Counter	41
3.4.2	Drift Chambers	45
3.5	Toroidal Magnet Spectrometer	47
4	Data Analysis	49
4.1	Overview	49
4.2	Hadronic Energy Measurement	49
4.2.1	Counter Gain Calibration	51
4.2.2	Calorimeter Energy Calibration	54
4.3	Hadronic Energy Calculation	58
4.4	Muon Angle and Momentum Measurement	58
4.4.1	Muon Tracking and Angle Measurement in the Calorimeter	59
4.4.2	Muon Energy Measurement	61
4.4.3	Muon Energy Loss in Target	66
4.5	Reconstruction of Kinematics in the Data	67
4.6	Cuts	68
4.6.1	Fiducial Volume Cuts	68
4.6.2	Kinematic Cuts	70
5	Monte Carlo Simulation	74

5.1	Event Generation	75
5.2	Resolution Smearing Simulation	77
5.3	Radiative Correction	79
6	Results	87
6.1	Data-Monte Carlo Comparison	87
6.1.1	Comparison With the Buras-Gaemers Model	87
6.1.2	Comparison with Buras-Gaemers Model Plus Fermi Motion	89
6.1.3	Comparison with Exponentially Falling \mathbf{F}_2 Models	92
6.1.4	Dependence of \mathbf{s} on Q^2	103
6.2	Systematic Errors	108
6.2.1	Energy Scale Error	109
6.2.2	Relative Calibration	109
6.2.3	Incoming Neutrino Angle	109
6.2.4	Outgoing Muon Angle	111
6.2.5	Hadronic Energy Mismeasurement	111
6.2.6	Radiative Corrections	112
6.2.7	Other Systematic Studies	113
6.2.8	Final Value of \mathbf{s}	117
6.2.9	Calculation of \mathbf{F}_2	117
6.3	Comparison With Theory and Other Measurements	122
6.3.1	Comparison of \mathbf{s}	122

6.3.2	Comparison of F_2	122
-------	-------------------------------	-----

List of Tables

1	Angular dependence of cross sections for neutrino and anti-neutrino scattering from partons in the CMF frame. Cross sections are in units of $\frac{1}{(1+Q^2/M_W^2)^2} \frac{G_F^2 s q}{\pi}$	17
2	CCFR calibration constants and resolutions for hadronic, electromagnetic, and MIP energy deposition in the target calorimeter.	56
3	Muon angular resolution parameters. These are used in equation 80 to find the resolution for different muon momenta and traveling lengths in the target calorimeter.	62
4	Cuts and their rejections.	72
5	The behavior of s with increasing Q^2	103
6	Systematic errors.	117

List of Figures

1	Kinematic variables of deep inelastic scattering. The struck quark carries a fraction x of the nucleon's momentum P	7
2	Possible interactions of high energy (anti)neutrinos and partons. . . .	16
3	The shape of the valance and sea quark distribution.	20
4	Comparison between F_2 and xF_3 from [13]. Error bars are statistical only. The curves are QCD fits (solid) and their extrapolations (dashed).	22
5	Fermi motion. The effect of other nucleons on the interacting nucleon.	26
6	Distance behavior of the nucleon-nucleon interaction potential.	30
7	The Fermilab Tevatron and neutrino beam-line.	35
8	Tevatron magnet current versus time during fixed target operation. P1, P2, and P3 are the ping extraction times. BESPL and ENSPL are the beginning and the end of the spill respectively.	36
9	The E770 quadrupole-triplet beam line following the primary proton beam line. Dipole magnets are indicated by prisms and quadrupole magnets are indicated by concave and convex lenses.	37
10	The neutrino and anti-neutrino event rates in the CCFR detector. The muon neutrinos and anti-neutrinos (ν_μ and $\bar{\nu}_\mu$) come predominantly from two body decays of pions and kaons. The electron neutrinos and anti-neutrinos (ν_e and $\bar{\nu}_e$) come from the three body decays of kaons and the muon decays.	39

11	Schematic representation of the CCFR detector. The neutrino beam enters from the left. The target-calorimeter is on the left and the muon spectrometer (toroid) is on the right. The two rightmost sets of drift chambers are known as the blue cart.	40
12	Layout of a CCFR target module. A scintillation counter is positioned after every two steel plates and a drift chamber is found after every four.	41
13	Schematic sketch of a scintillation counter. Four PMT's at the four corners collect the light output carried by wave shifter bars.	42
14	Readout electronics for a scintillation counter. Each counter is digitized by seven ADC channels. The threshold of the s-bit discriminator is set at one quarter minimum ionizing level.	44
15	(a) CCFR target drift chamber. There are two orthogonally oriented planes for each chamber consisting of three-wire cells. (b) A three-wire drift chamber cell.	46
16	Event displays of charged current event (bottom of the page) in the CCFR detector, used for the structure function analysis. A neutral current event is also shown (top of the page) for contrast.	50
17	Muon energy loss distribution in a scintillation counter.	52

18	Relative muon response for counter number 37. The contours show the response of the region relative to the response in the center of the counter. The response is higher near the edges because of proximity to the phototubes.	54
19	Energy response of the calorimeter for E744(squares) and E770(diamonds). The mean is 4.74 MIP's per GeV. The fractional deviation for E770 is about 0.7%.	55
20	The Calorimeter measured energy distributions of 25 and 200 GeV test beam hadrons. The particles were momentum analyzed in the test beam spectrometer independently. The curves represent Poisson-like parameterizations of the resolutions.	56
21	The hadronic energy measurement resolution of the calorimeter. The curve represents the fit of equation 75.	57
22	Experimental resolution function of the muon spectrometer for 120 GeV/c muons. The points are measurements of test beam muons, the solid line is an independent Monte Carlo prediction. The tail on the negative side is due to hard single scatters, and the tail on the positive side is due to catastrophic energy losses.	65
23	The x_{meas} distribution after all cuts.	73

24	Comparison between The Monte Carlo modeling of the muon energy resolution function, $f_{res} = \frac{1/p_{toroid}-1/p_{testbeam}}{1/p_{testbeam}}$ (the bar charts) and the Monte Carlo reconstructed resolution function (solid histogram). . . .	78
25	The muon bremsstrahlung radiative effect in charged current neutrino DIS. The radiated energy is absorbed inside the hadronic shower and causes a reduction in the observed muon energy and an increase in the observed hadronic energy.	80
26	The percentage of the radiative correction as a function of y for different x bins, for 200 GeV neutrino charged current events. The radiative correction modifies the cross section by the percentage shown. . . .	81
27	Event vertex radius in the data (solid histogram) and the Monte Carlo (discrete error bars). The horizontal axis is the vertex radius in inches.	82
28	Event vertex longitudinal coordinate in the data (error bars) and the Monte Carlo (solid histogram). Counter 1 is the most downstream. The fiducial volume cuts eliminate 4 most upstream and 20 most downstream counters (section 4.6).	83
29	End of the hadronic shower in the data (error bars) and the Monte Carlo (solid histogram). Counter 1 is the most downstream. There is no shower passed counter 6 and the hadronic shower is completely contained in the target.	84

30	Muon position at front face of the toroid in the data (error bars) and the Monte Carlo (solid histogram).	85
31	Muon track azimuthal angle at the event vertex in the data (error bars) and the Monte Carlo (solid histogram).	86
32	The generated x_g distribution in the the Buras-Gaemers model. This model forces the x_g distribution to go to zero at $x_g = 1.0$	88
33	The effect of smearing on a steeply falling histogram. The original histogram is shown with dotted lines. More events migrate from more populous bins to less populous bins than vise versa. The resulting histogram is shown with solid lines.	89
34	The observed x distribution in the data (solid histogram) and the Buras-Gaemers model (error bars).	90
35	The generated x_g distribution in Buras-Gaemers with Fermi gas motion of the nucleons (discrete bars) and without Fermi motion (solid histogram).	91
36	The observed x distribution in the data (solid histogram) and the Buras-Gaemers model with added nucleon Fermi gas distribution (error bars).	92
37	The generated x_g distribution in the Buras-Gaemers model with (discrete bars) and without (solid histogram) Fermi gas motion plus quasi-deuterons.	93

38	The observed x distribution in the data (solid histogram) and the Buras-Gaemers model with added nucleon Fermi gas distribution plus quasi-deuteron states (error bars).	94
39	The χ^2 of the Monte Carlo fit to the data x distribution as a function of s , the exponent coefficient of the exponentially falling F_2	95
40	The x distribution in the data (solid histogram) and the exponentially falling F_2 model with input value of $s = 8$	97
41	Neutrino energy in the data (solid histogram) and the exponentially falling F_2 model (discrete error bars) for the $x > 0.6$ region.	98
42	Q^2 in the data (solid histogram) and the exponentially falling F_2 model (discrete error bars) for the $x > 0.6$ region.	99
43	Muon energy in the data (solid histogram) and the exponentially falling F_2 model (discrete error bars) for the $x > 0.6$ region.	100
44	Hadronic energy in the data (solid histogram) and the exponentially falling F_2 model (discrete error bars) for the $x > 0.6$ region.	101
45	y distribution in the data (solid histogram) and the exponentially falling F_2 model (discrete error bars) for the $x > 0.6$ region.	102
46	The χ^2 of the Monte Carlo fit to the data x distribution as a function of s for $50 < Q^2 < 100$	104
47	The χ^2 of the Monte Carlo fit to the data x distribution as a function of s for $100 < Q^2 < 400$	105

48	The x distribution in the data (solid histogram) and the exponentially falling F_2 model with input value of $s = 8$ for $50 < Q^2 < 100$ (GeV) ² .	106
49	The x distribution in the data (solid histogram) and the exponentially falling F_2 model with input value of $s = 8$ for high $100 < Q^2 < 400$ (GeV) ² .	107
50	The value of s as a function of the percentage change in the energy scale.	110
51	Difference between E_{had} measured in (SHEND-5) and 20-counter formalisms.	112
52	Number of event in run blocks for all events (top), for large x events (middle), and the ratio of the two (bottom).	115
53	Muon azimuthal angle for all events (top) and for large x events (middle) and the ration of the two (bottom).	116
54	Contour plots of χ^2 as a function of the change in s and the percentage change in N .	119
55	Calculated F_2 within the exponentially falling model. The band shows the prediction of the model for $x > 0.75$ and $Q^2 = 80$ (GeV) ² .	120
56	Calculated F_2 within the exponentially falling model. The band shows the prediction of the model for $x > 0.75$ and $Q^2 = 125$ (GeV) ² .	121

1 Introduction

This thesis presents the measurement of nuclear structure functions at high x and high Q^2 in neutrino-iron deep inelastic scattering. The structure functions have been rarely explored in this region because of experimental difficulties. They have never been measured in neutrino deep inelastic scattering in the large x region. Neutrino scattering is a well suited process for this kind of measurement since, due to the large momentum transfer (Q^2) of its nature, it can resolve shorter subnuclear distances. By measuring nuclear structure functions in this region, one should elucidate nuclear effects in deep inelastic scattering processes. These nuclear effects manifest themselves very clearly in this region since the contribution from single, isolated nucleons would vanish at large x .

The data used in this thesis was collected during the 1987-1988 fixed target run in the Fermilab E770 experiment. The CCFR detector was used for this measurement. During the E770 run about one million neutrino charged current events were accumulated. The latest structure function analysis on these events is found in [13].

1.1 The Standard Model

The Standard Model (SM) of particle physics is the corner stone of our understanding of elementary particles and their interactions. There are 6 quarks, each with three different degrees of freedom (called color), and 6 leptons in this model. All quarks have electric charge of magnitude $\frac{1}{3}e$ or $\frac{2}{3}e$ and their masses range from less than 1

GeV/c² to 175 GeV/c² for the newly observed top quark. Three of the leptons have electric charge of magnitude e and their masses range from 0.5 MeV to 1.8 GeV. Other three leptons are neutrinos with no electric charge and there is no solid evidence to date of them having any mass.

Four different types of interaction are known between these particles. These interactions have different strengths at the currently available energies. In order of increasing strength, the interactions and participating particles are:

1. Gravitation, mediated by the graviton; all particles take part;¹
2. Weak, mediated by vector bosons, Z and W^\pm ; all quarks and leptons take part;
3. Electromagnetic, mediated by the photon; all charged particles² take part; and,
4. Strong, mediated by gluons; all quarks take part.³

The SM of these interactions are renormalizable and capable of making predictions. Because of the large coupling of strong interaction and the fact that gluons themselves participate, the strong interaction is less well understood than weak and electromagnetic interactions. The theories of electromagnetic and weak interactions were combined into a single “electroweak” interactions theory by Salam and Weinberg in the 70’s. Many efforts are currently going on to unify the strong interactions with the electroweak interactions.

¹Gravitation is not a part of the SM.

²This includes charged vector boson W^\pm .

³Gluons carry color and could further interact with quarks and other gluons.

1.2 Deep Inelastic Scattering

Quarks and gluons form into bound states of nucleons (protons and neutrons), which in turn, bind together to form nuclei. Scattering processes are important means of exploring the substructure of the nucleus and nucleons. To probe the substructure, the interactions of the probe should be as well-understood as possible. Leptons seem to have no internal structure, even at the high energies (small wavelengths) currently available. They do not interact strongly and, therefore, their interactions can be calculated very well with perturbation theory. Since they are point-like and their interactions are well understood, high energy leptons are best suited for probing deep into the structure of matter. High energy and high intensity beams of leptons (up to several hundred GeV) are produced in accelerator laboratories. These beams hit fixed nuclear targets (hydrogen, deuteron, carbon, aluminum, iron, ...) and interact with target nucleons. The lepton scattering processes of interest with nucleons are:

$$e + N \rightarrow e + X \quad ,$$

$$\mu + N \rightarrow \mu + X \quad ,$$

$$\nu_\mu + N \rightarrow \mu^- + X \quad ,$$

$$\bar{\nu}_\mu + N \rightarrow \mu^+ + X \quad ,$$

$$\nu_e + N \rightarrow e^- + X \quad ,$$

$$\bar{\nu}_e + N \rightarrow e^+ + X \quad .$$

At high momentum transfer, leptons can resolve small distances inside the nucleon and reveal the nature of its constituents, the quarks. Such interactions are “inelastic”.

The struck quark hadronizes in the target and produces a large number of outgoing hadrons, called the “hadronic shower”. There is a final state lepton in all these interactions along with the hadronic shower and these together form the products of the interaction.

From the knowledge of the lepton beam⁴ and of the kinematic variables which describe the interaction products, one can extract the structure of the target. This thesis is based on the last of these processes, the neutrino charged current deep inelastic scattering (DIS).⁵

1.3 Nuclear Effects on DIS

In the late 60’s, it was thought that the deep inelastic scattering of leptons from nucleons can be considered as elastic scattering from point-like nucleon constituents, partons. This phenomenon was called “scaling”. The structure of proton seemed to be thoroughly explained with one variable (Bjorken scaling variable, x) which scaled with energy.

Later on when higher momentum transfers were available, the effect of the rest of the nucleon on the interacting parton was elucidated. Each time the momentum transfer (and therefore the resolution) increases, it reveals more of the structure of previously virtual quarks and gluons. It was clear then that the struck parton cannot

⁴In the case of charged leptons, one knows the initial energy of the incoming lepton, whereas, in the case of neutrino scattering, this energy is reconstructed from the energy measurement of final state products. In both cases the direction of the the incoming particles is known.

⁵Neutrino neutral current DIS also makes up a sizable portion of the neutrino DIS data but it is not used in this analysis since one cannot reconstruct the kinematics of the outgoing neutrino.

be considered as an isolated particle. The nucleon environment affects the DIS process in such a way that the structure functions drop logarithmically as a function of Q^2 . This was known as “scaling violation”.

Because the nucleon itself is inside the nucleus, the nuclear environment affects DIS processes as well. In the mid 80’s the European Muon Collaboration (EMC) [21] reported that the structure function F_2 measured in DIS from hydrogen is different from the one measured in DIS from heavy nuclear target. This disagreement is often depicted as a dip in the ratio of $\frac{F_2^A}{F_2^p}$ below one in $0.3 < x < 0.7$ region. It was known ever since as EMC effect and was confirmed in other experiments. This effect is a result of nuclear environment on DIS. Later on other nuclear effects such as shadowing were observed in different kinematic regions in different experiments. The effect of the nuclear environment on DIS was shown to be significant and clear. Many theoretical works were done consequently to parameterize these effects.

To understand the nuclear effects in DIS, measurement of nuclear structure functions in the large x and large Q^2 kinematic region is beneficial. It can discriminate between competing models. This is because if there were no nuclear effects, the structure functions would vanish in this region. Therefore almost all the events that occur in large x region are due to nuclear effects. These effects are parameterized in different forms such as:

- Fermi motion; the motion of nucleon with respect to the center-of-mass of the nucleus;

- few-nucleon correlations; the effect of adjacent nucleons on the patron distribution in a nucleon; and,

- multi-quark clusters; the formation of bound states of more than three valence quarks in the nucleus.

All these effects could explain the occurrence of large x events in DIS to some extents. In this analysis the data from Fermilab E770 experiment are used to compare the observed distributions with the predictions of these nuclear models and a model with no nuclear effects. The data has been used to fix free parameters of these models when applicable and a measurement of the structure functions is presented within the framework of these models.

2 Theoretical Background

2.1 Neutrino DIS Cross Section

Figure 1 shows the Feynman diagram for a charged current DIS event. At the top of the figure is the leptonic vertex. The incoming neutrino (anti-neutrino) emits a charged vector boson, $W^+(W^-)$, and turns into a muon. Both the electric charge and the lepton number are conserved. The $W^+(W^-)$ carries a four momentum q which is the difference between the four momenta of the incoming neutrino and the outgoing muon. At the lower vertex, the $W^+(W^-)$ gets absorbed by a quark inside

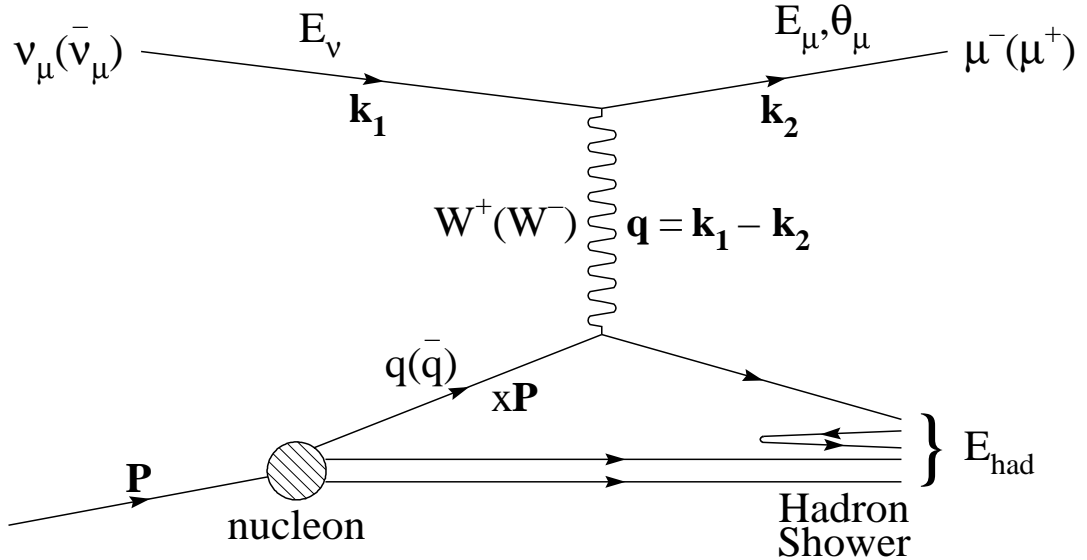


Figure 1: Kinematic variables of deep inelastic scattering. The struck quark carries a fraction x of the nucleon's momentum P .

the nucleon. The quark type changes after the absorption such that the electric charge is conserved. The situation could be illustrated in a four quark picture with u , d , s , and c quarks. The W^+ could couple to d or s quarks, or \bar{u} or \bar{c} anti-quarks. The

outgoing particle will then be a u or a c quark, or a \bar{d} or \bar{s} anti-quark respectively. The W^- could couple to u or c quarks, or \bar{d} or \bar{s} anti-quarks. The product is a d or s quark, or a \bar{u} or \bar{c} anti-quark respectively. The four-momentum of the W particle is transferred to the struck quark or anti-quark. The struck particle is scattered away from the rest of the nucleon and, as a result, additional quark-antiquark pairs are produced. This happens because quarks and anti-quarks cannot exist by themselves and they have to hadronize. The quark pair production and hadronization continues until the system runs out of energy. A myriad of outgoing hadrons results from the process.

The detailed calculation of the Born level cross section for the above process is given in many text books (*e.g.* [18]). Consider the case of a charged current neutrino scattering from a nucleon. The leptonic vertex factor consists of the annihilation of a neutrino with four-momentum p and creation of a muon with a four-momentum p' . The leptonic part of the interaction takes the form:

$$\frac{g}{\sqrt{2}}\bar{\mu}(p')\gamma_\alpha\frac{1-\gamma_5}{2}\nu(p) \quad (1)$$

where g is the weak interaction coupling constant, $\bar{\mu}(p')$ is the wave function of the outgoing muon, and $\nu(p)$ is the wave function of the incoming neutrino. Squaring this, the covariant leptonic tensor then becomes:

$$\left(\frac{g}{\sqrt{2}}\bar{\mu}(p')\gamma_\alpha\frac{1-\gamma_5}{2}\nu(p)\right)\left(\frac{g}{\sqrt{2}}\bar{\mu}(p')\gamma_\beta\frac{1-\gamma_5}{2}\nu(p)\right)^\dagger. \quad (2)$$

After summing over the outgoing muon's spins this reduces to:

$$L_{\alpha\beta} = g^2(p'_{\alpha}p_{\beta} + p_{\alpha}p'_{\beta} - p' \cdot p g_{\alpha\beta} - i\varepsilon_{\alpha\beta\gamma\rho}p'^{\gamma}p^{\rho}) \quad . \quad (3)$$

As hadrons are not point-like particles one needs a more general expression for the hadronic tensor. The most general hadronic tensor for inclusive, parity violating, lepton-nucleon scattering is:

$$W_{\alpha\beta} = g_{\alpha\beta}V_1 - P_{\alpha}P_{\beta}V_2 + (P_{\alpha}q_{\beta} + P_{\beta}q_{\alpha})V_3 + q_{\alpha}q_{\beta}V_4 + i\varepsilon_{\alpha\beta\gamma\rho}P^{\gamma}q^{\rho}V_5 \quad , \quad (4)$$

where P is the four-momentum of the nucleon before the interaction and q is the transferred four-momentum. The V_i are arbitrary functions of scalar kinematic variables made from the four-vectors P and q . Since they represent the substructure of the nucleon, the V_i are called “structure functions” (SF). There are two independent scalar variables made from P and q , say, q^2 , the squared momentum transfer of the scattering process, and $P \cdot q$.⁶ Therefore the SF's could be functions of only two variables, q^2 and $P \cdot q$, or equivalently any linearly independent pair of combinations of these two.

The cross section could be calculated from the leptonic and hadronic covariant tensors and the W propagator:

$$\frac{g_{\alpha\beta} + q_{\alpha}q_{\beta}/M_W^2}{q^2 - M_W^2} \quad . \quad (5)$$

Because the W mass is large ($M_W \sim 80$ GeV), the second term in the numerator can

⁶Since the nucleon is assumed to be on mass shell, $P^2 = M_N^2$ is not variable.

be neglected. The differential cross section becomes:

$$\frac{d^2\sigma}{dE_\mu d\Omega} = \frac{1}{2} \left(\frac{g}{2}\right)^2 \frac{E_\mu}{(4\pi)^2 E_\nu} \left(\frac{1}{q^2 - M_W^2}\right)^2 L^{\alpha\beta} W_{\alpha\beta} \quad . \quad (6)$$

Contraction of the leptonic and the hadronic tensors yields:

$$L^{\alpha\beta} W_{\alpha\beta} = g^2 \left[-2(p' \cdot p)V_1 + [2(p' \cdot P)(p \cdot P) - M_N^2(p \cdot p')]V_2 + \varepsilon_{\rho\gamma}^{\alpha\beta} \varepsilon_{\alpha\beta\sigma\eta} p^\rho q^\gamma P^\sigma q^\eta V_3 \right] \quad . \quad (7)$$

The contribution from V_3 and V_4 terms are proportional to the square of the muon mass and have been neglected.

In the laboratory frame, taking the z direction to be the direction of the neutrino momentum and assuming that the nucleon is at rest, we have (see figure 1):

$$k = (E_\nu; 0, 0, E_\nu) \quad , \quad (8)$$

$$k' = (E_\mu; p_\mu \sin \theta \cos \phi, p_\mu \sin \theta \sin \phi, p_\mu \cos \theta) \quad , \quad (9)$$

$$P = (M_N; 0, 0, 0) \quad , \quad (10)$$

$$P' = P + q = P + (k - k') \quad , \quad (11)$$

where E_ν and E_μ are the neutrino and the muon energy respectively, θ is the (polar) angle between the incoming neutrino and the outgoing muon, and ϕ is the azimuthal angle of the muon in the laboratory frame. The four momentum transfer in terms of these laboratory quantities is:

$$q^2 = -Q^2 = -4E_\nu E_\mu \sin^2 \frac{\theta}{2} \quad (12)$$

There are a few other useful variables. One is:

$$\nu = \frac{P \cdot q}{M_N} \quad , \quad (13)$$

which in the laboratory frame translates into the hadronic energy:

$$\nu = E_{had} \quad , \quad (14)$$

The other one is the inelasticity defined as:

$$y = \frac{P \cdot q}{k \cdot q} \quad , \quad (15)$$

which is related to the neutrino-quark center-of-mass frame scattering angle by:

$$1 - y = \frac{1 + \cos(\theta^*)}{2} \quad . \quad (16)$$

In the laboratory frame, y is the ratio of the energy transferred to the nucleon (hadronic shower energy) to the total neutrino energy (hadronic energy plus muon energy).

$$y = \frac{E_\nu - E_\mu}{E_\nu} \simeq \frac{E_{had}}{E_\nu} \quad . \quad (17)$$

Finally, the Bjorken scaling variable is defined as:

$$x = \frac{Q^2}{2P \cdot q} \quad . \quad (18)$$

This variable measured in the laboratory frame becomes:

$$x_{meas} = \frac{Q^2}{2M_N \nu} = \frac{4E_\nu E_\mu \sin^2 \theta / 2}{2M_N E_{had}} \quad . \quad (19)$$

The variables Q^2 , y , and x are Lorentz scalars.

Before proceeding further with the cross section and the structure functions a few words about the Bjorken scaling variable, x , are in order. For elastic scattering x is simply unity:

$$x = \frac{-q^2}{2P \cdot q} = \frac{-q^2}{-q^2} = 1 \quad . \quad (20)$$

In lepton-nucleon DIS however, the restriction is that x should be less than one:

$$0 < x \leq 1 \quad (21)$$

This is a result of the fact that the nucleon is the lightest baryon. According to the conservation of baryon number there should be at least one baryon in the final state. The invariant mass of the hadronic final state is always larger than the mass of the nucleon:

$$M_X = \sqrt{(P+q)^2} > M_N \quad . \quad (22)$$

The variable x_{meas} then becomes:

$$x_{meas} = \frac{Q^2}{(P+q)^2 - P^2 + Q^2} = \frac{Q^2}{M_X^2 - M_N^2 + Q^2} = \frac{1}{1 + \frac{M_X^2 - M_N^2}{Q^2}} \quad , \quad (23)$$

and hence the inequality 21.

The structure functions will have a rather simple form when parameterized in terms of the negative square of four-momentum transfer Q^2 and x . It is also customary to make the following replacements to get dimensionless structure functions :

$$-M_N V_1 = F_1 \quad , \quad -\frac{\nu V_2}{M_N^2} = F_2 \quad , \quad \frac{\nu V_5}{2M_N^2} = F_3 \quad . \quad (24)$$

Using these along with equations 6 and 7, the cross section becomes:

$$\frac{d^2\sigma}{dx dQ^2} = \frac{G_F^2}{\pi(1 + Q^2/M_W^2)^2} \left[y^2 x F_1^{\nu(\bar{\nu})}(x, Q^2) + \left(1 - y - \frac{M_N xy}{2E_\nu}\right) F_2^{\nu(\bar{\nu})}(x, Q^2) \pm y \left(1 - \frac{y}{2}\right) x F_3^{\nu(\bar{\nu})}(x, Q^2) \right] \quad (25)$$

where

$$G_F = \frac{g^2}{4\sqrt{2}M_W^2} \quad , \quad (26)$$

is the Fermi constant. The minus sign in equation 25 is for anti-neutrino scattering.

In terms of x and y variables the double differential cross section becomes:

$$\frac{d^2\sigma}{dxdy} = \frac{G_F^2 M_N E_\nu}{\pi(1 + Q^2/M_W^2)^2} \left[y^2 x F_1^{\nu(\bar{\nu})}(x, Q^2) + \left(1 - y - \frac{M_N xy}{2E_\nu}\right) F_2^{\nu(\bar{\nu})}(x, Q^2) \pm y \left(1 - \frac{y}{2}\right) x F_3^{\nu(\bar{\nu})}(x, Q^2) \right] . \quad (27)$$

One interesting feature of the neutrino DIS is that, unlike electron and muon DIS, the coefficient in front of the brackets does not fall as $1/Q^4$ and, for fixed energy, it is flat for $Q^2 \ll M_W^2$. This gives the neutrino DIS process a unique capability to probe the target matter with very large momentum transfer and resolve much smaller distances. This makes one able to explore high x events at high momentum transfer.

Another manner in which equation 25 differs from charged lepton DIS, is the appearance of $x F_3$ in this cross section formula. This is the result of the V-A structure of weak interactions and, as such, only occurs in neutrino DIS. This feature allows a direct measurement of the valence quark distributions. This is very important in the parameterizations of parton density functions.

2.2 The Quark-Parton Model (QPM)

The “naive” quark-parton model (QPM) is a simplified model of lepton-nucleon DIS. It is based on neglecting the QCD radiative effects inside the nucleon. The lepton inelastic scattering from a nucleon is considered to be the elastic scattering from “partons”, the constituents of the nucleon.

2.2.1 Helicity and y Distributions in Center of Momentum Frame

The V-A structure of the weak interactions is implied by the parity violating $\frac{1-\gamma_5}{2}$ factor in equation 1. In Dirac algebra γ_5 is:

$$\gamma_5 = i\gamma_0\gamma_1\gamma_2\gamma_3 \quad , \quad (28)$$

where the Dirac matrices fulfill the anti-commutation relations:

$$\{\gamma_\alpha, \gamma_\beta\} = 2g_{\alpha\beta} \quad , \quad \alpha, \beta = 1, 4 \quad . \quad (29)$$

These last two equations imply:

$$\gamma_5^2 = 1 \quad . \quad (30)$$

The fact that the square of γ_5 is the identity operator causes the operator $\frac{1-\gamma_5}{2}$ and its complement $\frac{1+\gamma_5}{2}$ to act as projection operators with the following properties:

$$\left(\frac{1-\gamma_5}{2}\right)^2 = \frac{1-\gamma_5}{2}, \quad \left(\frac{1+\gamma_5}{2}\right)^2 = \frac{1+\gamma_5}{2} \quad , \quad (31)$$

$$\left(\frac{1-\gamma_5}{2}\right)\left(\frac{1+\gamma_5}{2}\right) = \left(\frac{1+\gamma_5}{2}\right)\left(\frac{1-\gamma_5}{2}\right) = 0 \quad . \quad (32)$$

They also obey the completeness relation:

$$\frac{1-\gamma_5}{2} + \frac{1+\gamma_5}{2} = 1 \quad . \quad (33)$$

When $\frac{1-\gamma_5}{2}$ acts on a neutrino spinor it selects its negative helicity⁷ (left-handed) component. Similarly $\frac{1+\gamma_5}{2}$ selects the positive helicity (right-handed) component of

⁷Helicity is the normalized projection of a particle's spin along its direction of motion. For massless particles helicity and chirality (handedness) are the same [20].

the neutrino spinor. As a result, only left-handed neutrinos and right-handed anti-neutrinos can take part in weak interactions. In the DIS regime we can neglect the mass of the quarks. Therefore the same thing can be said about them; only left-handed quarks and right-handed anti-quarks can partake in weak interactions.

The cross section for neutrino elastic scattering from point-like partons in principle could depend on the center-of-momentum frame (CMF) energy and scattering angle. The spin of the (anti)neutrino and the parton constituent of the nucleon are both $1/2$. The helicity considerations stated above determine possible interactions between neutrino (anti-neutrino) and partons. This gives the angular dependence of the differential cross section in the CMF. In the CMF the direction of the colliding particles are necessarily opposite. Figure 2 shows possible helicity configurations of (anti)neutrino scattering from partons. We also consider the possibility of spin-0 constituents of the nucleon and denote them by k .

In the case of neutrino scattering from a quark, both particles should be left-handed. The direction of the spins are also opposite and the total angular momentum of the system is zero. This implies that the differential cross section can depend only on the neutrino-quark CMF energy-squared, s_q , and not the CMF angle, θ^* . The same argument holds for anti-neutrino scattering from anti-quarks. For neutrino scattering from anti-quarks or anti-neutrino scattering from quarks, the total angular momentum of the system is 1 and the cross section is angle dependence. If there are particles, k , of spin-0 in the nucleon, the total angular momentum of the ν -

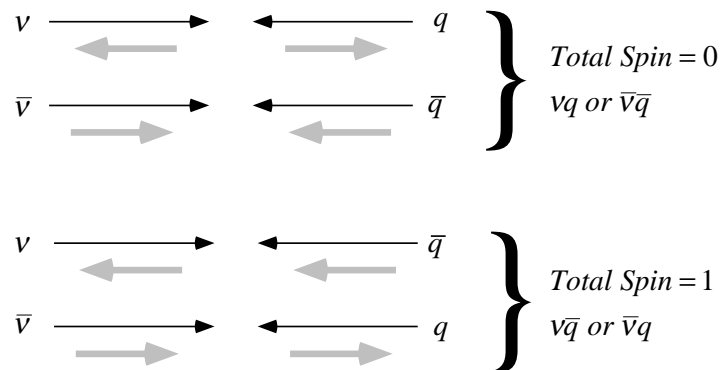


Figure 2: Possible interactions of high energy (anti)neutrinos and partons.

k or the $\bar{\nu}-k$ systems will be $1/2$ and the cross section would be angle dependent.

Table 1 summarizes possible interactions along with their total spin and the angular dependence of the cross sections.

2.3 QPM and the Bjorken Scaling Variable, x

The significance of x in DIS becomes clear if we consider the parton model in the “infinite momentum frame”. If we assume that the transverse momentum of the parton inside the proton is negligible compared with its longitudinal momentum, the initial momentum of the i_{th} parton, P_i , is simply a fraction ξ_i of the momentum of

Interaction	Total Spin	$\frac{d\sigma}{d\cos\theta^*}$	$\frac{d\sigma}{dy}$
$\nu-q$ or $\bar{\nu}-\bar{q}$	0	1	1
$\nu-\bar{q}$ or $\bar{\nu}-q$	1	$\left(\frac{1+\cos\theta^*}{2}\right)^2$	$(1-y)^2$
$k-q$ or $k-\bar{q}$	1/2	$1 + \cos\theta^*$	$2(1-y)$

Table 1: Angular dependence of cross sections for neutrino and anti-neutrino scattering from partons in the CMF frame. Cross sections are in units of $\frac{1}{(1+Q^2/M_W^2)^2} \frac{G_F^2 s q}{\pi}$.

the nucleon P :

$$P_i = \xi_i P \quad (34)$$

The final momentum of the struck parton is:

$$P'_i = P_i + q \quad . \quad (35)$$

Neglecting the mass of the parton and nucleon one gets:

$$0 \approx P'^2_i = (P_i + q)^2 = (\xi_i P + q)^2 \approx 2\xi_i P \cdot q + q^2 \quad (36)$$

and hence:

$$\xi_i = \frac{Q^2}{2P \cdot q} = x \quad . \quad (37)$$

This means that in a reference frame with large nucleon momentum (infinite momentum frame), according to the parton model, x is simply the fractional momentum of the nucleon carried by the parton.

2.3.1 QPM and Structure Functions

According to what was shown in the foregoing section, the differential cross sections for the neutrino-parton or antineutrino-parton interactions in the CMF are given by:

$$\frac{d\sigma^{\nu q}}{d\cos\theta^*} = \frac{d\sigma^{\bar{\nu}\bar{q}}}{d\cos\theta^*} = \frac{G^2 s_q}{\pi(1 + Q^2/M_W^2)^2} , \quad \text{for total spin 0;} \quad (38)$$

$$\frac{d\sigma^{\nu\bar{q}}}{d\cos\theta^*} = \frac{d\sigma^{\bar{\nu}q}}{d\cos\theta^*} = \frac{G^2 s_q}{\pi(1 + Q^2/M_W^2)^2} \left(\frac{1 + \cos\theta^*}{2} \right)^2 , \quad \text{for total spin 1;} \quad (39)$$

$$\frac{d\sigma^{\nu k}}{d\cos\theta^*} = \frac{d\sigma^{\bar{\nu}k}}{d\cos\theta^*} = \frac{G^2 s_q}{\pi(1 + Q^2/M_W^2)^2} (1 + \cos\theta^*) , \quad \text{for total spin 1/2;} \quad (40)$$

where s_q is the E_{CMF}^2 for the neutrino-parton system.

Now consider neutrino or anti-neutrino DIS scattering from a nucleon as the incoherent sum of elastic scatterings from partons. The parton could be a quark, q , an anti-quark, \bar{q} , or a spin-0 constituent, k . If we knew the parton momentum, we could completely constrain the kinematics. Since this momentum is not known, we introduce $f(x)$, the probability of scattering from a parton type f , carrying a fraction x of the total momentum of the nucleon. The function $f(x)$ is called the parton density function. The parton fractional momentum distribution is then $xf(x)$. The cross sections for neutrino and anti-neutrino scattering become:

$$\frac{d^2\sigma^\nu}{dx dy} = \frac{G^2 x s}{\pi(1 + Q^2/M_W^2)^2} \left[q^\nu(x) + (1 - y)^2 \bar{q}^\nu(x) + 2(1 - y)k^\nu(x) \right] , \quad (41)$$

$$\frac{d^2\sigma^{\bar{\nu}}}{dx dy} = \frac{G^2 x s}{\pi(1 + Q^2/M_W^2)^2} \left[\bar{q}^{\bar{\nu}}(x) + (1 - y)^2 q^{\bar{\nu}}(x) + 2(1 - y)k^{\bar{\nu}}(x) \right] . \quad (42)$$

The functions $q(x)$ and $\bar{q}(x)$ are sums of all quark and anti-quark types respectively.

The CMF energy-squared of the neutrino-parton system, s_q , is written in terms of the CMF energy-squared of the neutrino-nucleon system, s . As a function of laboratory quantities, these two quantities are:

$$s = 2M_N E_\nu , \quad (43)$$

$$s_q = xs \quad . \quad (44)$$

Comparing these equations with equation 27 and neglecting the $\frac{M_N xy}{E_\nu}$ term, the structure functions have the following relations with the parton momentum distribution functions:

$$2xF_1^{\nu(\bar{\nu})} = 2 \left[xq^{\nu(\bar{\nu})}(x) + x\bar{q}^{\nu(\bar{\nu})}(x) \right] \quad , \quad (45)$$

$$F_2^{\nu(\bar{\nu})} = 2 \left[xq^{\nu(\bar{\nu})}(x) + x\bar{q}^{\nu(\bar{\nu})}(x) + 2xk^{\nu(\bar{\nu})}(x) \right] \quad , \quad (46)$$

$$xF_3^{\nu(\bar{\nu})} = 2 \left[xq^{\nu(\bar{\nu})}(x) - x\bar{q}^{\nu(\bar{\nu})}(x) \right] \quad . \quad (47)$$

As a consequence of the QPM the structure functions are functions of one variable only:

$$F_i(Q^2, x) \longrightarrow F_i(x) \quad . \quad (48)$$

This feature of the QPM is called scaling [31]. It is a result of neglecting the QCD interactions of partons. The Q^2 dependence of the structure functions stems from QCD radiative effects inside the nucleon [18].

If the scattering was only from spin 1/2 particles, we would have:

$$2xF_1 = F_2 \quad . \quad (49)$$

This is known as the Callan-Gross relation [31]. At low energies this equation does not hold due to the significance of the transverse momentum components of the nucleon. These transverse momenta give the partons apparent spin-0 component in the infinite momentum frame. However this component diminishes as Q^2 is increased.

If the spin-0 component is neglected, the difference between the two structure functions, F_2 and xF_3 , is in the anti-quark components (see equations 46 and 47). Quarks and anti-quarks are produced and annihilated in pairs. These pairs are the quark anti-quark sea of partons in the nucleon. The “sea quarks” carry little momentum and their distribution vanishes rapidly with increasing x . Figure 3 shows a schematic comparison of the valence and the sea quark distributions. As a result of the steeply falling sea quark component at high x , the following approximation holds to very high accuracy:

$$xF_3 \approx F_2 \quad . \quad (50)$$

The equivalence of F_2 and xF_3 has been established in the CCFR data [13] for $x > 0.5$.

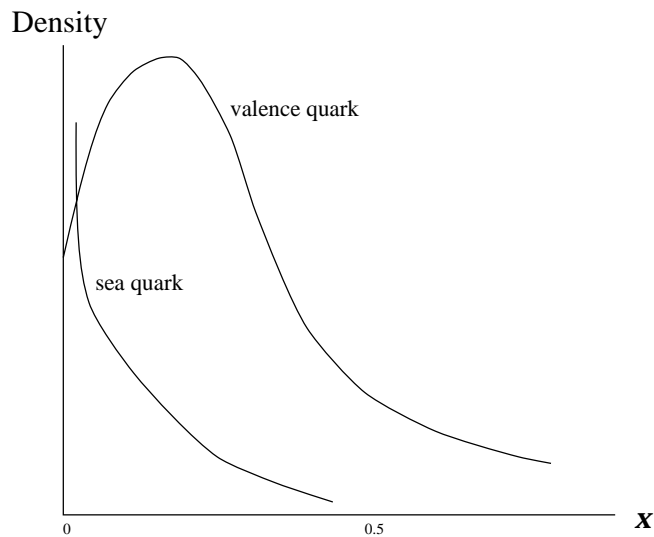


Figure 3: The shape of the valence and sea quark distribution.

Equations 49 and 50 imply that in the DIS regime and in the high x kinematic region,

all three structure functions are the same. This assumption is used in this analysis:

$$2xF_1 = xF_3 = F_2 \quad . \quad (51)$$

An overlay plot of F_2 and xF_3 is shown in figure 4 from [13]. The equality is correct to better than 2%.

As mentioned, neutrino DIS has the unique feature of probing certain flavors of the nucleon constituents. To compare F_2 from neutrino DIS to that of the charged lepton DIS, we write down the quark density functions for a proton target as :

$$\begin{aligned} q^{\nu p}(x) &= d^p(x) + s^p(x) \quad , \\ \bar{q}^{\nu p}(x) &= \bar{u}^p(x) + \bar{c}^p(x) \quad , \\ q^{\bar{\nu} p}(x) &= u^p(x) + c^p(x) \quad , \\ \bar{q}^{\bar{\nu} p}(x) &= \bar{d}^p(x) + \bar{s}^p(x) \quad . \end{aligned}$$

For a four light-quark picture, the strong isospin invariance then determines the neutron density functions to be:

$$\begin{aligned} d(x) &\equiv d^p(x) = u^n(x) \quad , \\ u(x) &\equiv u^p(x) = d^n(x) \quad , \\ \bar{d}(x) &\equiv \bar{d}^p(x) = \bar{u}^n(x) \quad , \\ \bar{u}(x) &\equiv \bar{u}^p(x) = \bar{d}^n(x) \quad . \end{aligned}$$

Assuming the strange and charm quarks content of the proton and neutron to be same, the neutron density functions could be written in terms of the proton density functions:

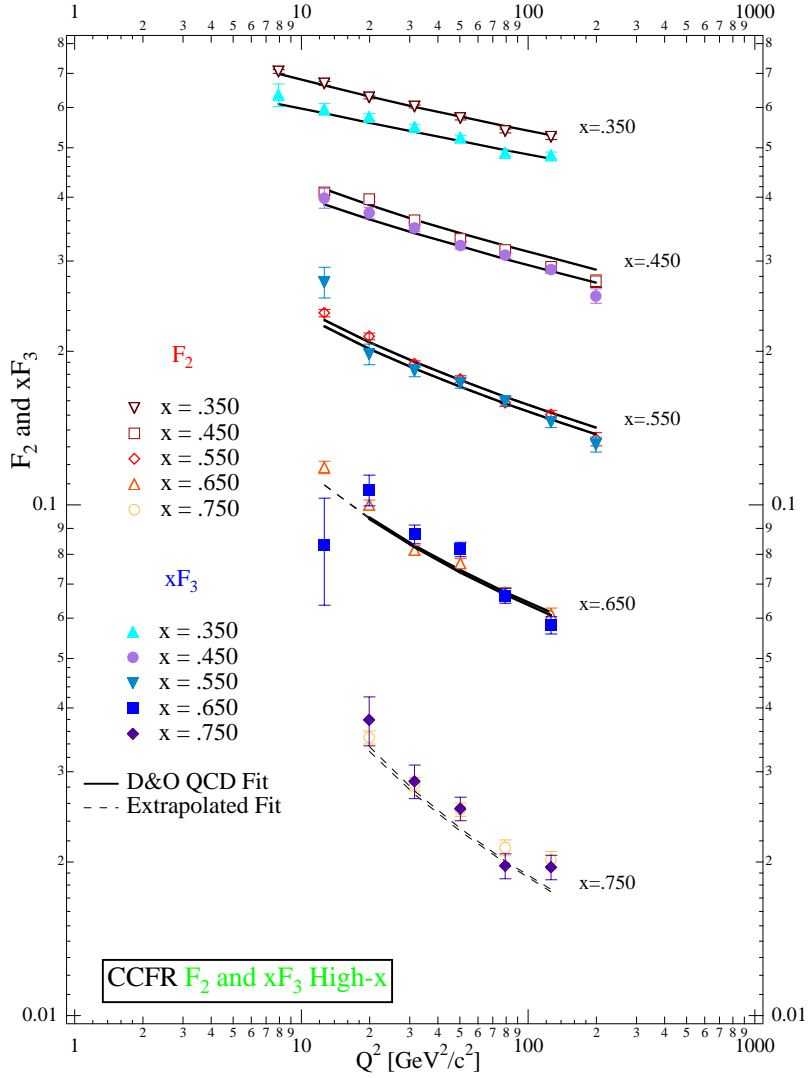


Figure 4: Comparison between F_2 and xF_3 from [13]. Error bars are statistical only. The curves are QCD fits (solid) and their extrapolations (dashed).

$$q^{\nu n}(x) = u(x) + s(x) \quad ,$$

$$\bar{q}^{\nu n}(x) = \bar{d}(x) + \bar{c}(x) \quad ,$$

$$q^{\bar{\nu} n}(x) = d(x) + c(x) \quad ,$$

$$\bar{q}^{\bar{\nu} n}(x) = \bar{u}(x) + \bar{c}(x) \quad .$$

The parton density functions for an isoscalar target (normalized to $\frac{1}{2}$ (proton + neutron)) then become:

$$q^{\nu N}(x) = \frac{1}{2}[u(x) + d(x) + 2s(x)] \quad (52)$$

$$q^{\bar{\nu} N}(x) = \frac{1}{2}[u(x) + d(x) + 2c(x)] \quad (53)$$

$$\bar{q}^{\nu N}(x) = \frac{1}{2}[\bar{u}(x) + \bar{d}(x) + 2\bar{c}(x)] \quad (54)$$

$$\bar{q}^{\bar{\nu} N}(x) = \frac{1}{2}[\bar{u}(x) + \bar{d}(x) + 2\bar{s}(x)] \quad . \quad (55)$$

The isoscalar structure function (SF) then becomes:

$$2xF_1^{\nu N} = xu + x\bar{u} + xd + x\bar{d} + xs + x\bar{s} + xc + x\bar{c} \quad (56)$$

where x arguments are omitted for clarity.

The electromagnetic SF's sample only the charge of the nucleon constituents.

They are written for proton and neutron as:

$$2xF_1^{\ell p} = \left(\frac{1}{3}\right)^2 [xd + x\bar{d} + xs + x\bar{s}] + \left(\frac{2}{3}\right)^2 [xu + x\bar{u} + xc + x\bar{c}] \quad , \quad (57)$$

$$2xF_1^{\ell n} = \left(\frac{1}{3}\right)^2 [xu + x\bar{u} + xc + x\bar{c}] + \left(\frac{2}{3}\right)^2 [xd + x\bar{d} + xs + x\bar{s}] \quad . \quad (58)$$

Averaging for an isoscalar target one gets:

$$2xF_1^{\ell N} = \left(\frac{5}{18}\right) [xu + x\bar{u} + xd + x\bar{d}] + \left(\frac{1}{9}\right) [xs + x\bar{s}] + \left(\frac{4}{9}\right) [xc + x\bar{c}] \quad . \quad (59)$$

Assuming that the ratio of $2xF_1$ for a charged lepton and a neutrino is the same as the ratio of F_2 for the two, this latter ratio becomes:

$$\frac{F_2^{\ell N}}{F_2^{\nu N}} = \frac{2xF_1^{\ell N}}{2xF_1^{\nu N}} = \frac{5}{18} \left(1 - \frac{3}{5} \frac{xs + x\bar{s} - xc - x\bar{c}}{xq + x\bar{q}} \right) . \quad (60)$$

where $2xF_1^{\nu N} = xq + x\bar{q}$. This relationship is known as the $\frac{5}{18}$ th rule. It is used to compare the structure functions from neutrino DIS to charged leptons DIS. The strange and the charm quark densities enter as corrections to the $\frac{5}{18}$ th rule.

2.4 Large x Kinematic Region

In section 2.1 the covariant definition of x (equation 18) and the measured quantity in the laboratory frame x_{meas} (equation 19) were introduced. The conclusion, $0 \leq x_{meas} \leq 1$ (equation 21), was then made based on equality of covariant x and measured x_{meas} . This equality however is based on the assumption that the (anti)neutrino scatters from a free nucleon at rest in the laboratory frame. In nuclear matter (which most DIS experiments use as targets), the nucleons are neither at rest nor free. The nucleons in a nucleus are in constant motion (“Fermi motion”). This motion is affected by nearby nucleons (“few nucleon correlation”). In addition, the nucleons may have emitted a pion and be off-shell when the neutrino hit. Equally the neutrino might have interacted with the pion. In any of these cases, the initial particle’s four-momentum was not $p^\mu = (M; 0, 0, 0)$.

In addition to just the nucleon motion, the motion of the quarks may be affected by the nuclear environment (the higher probability of interacting with an emitted

pion is an example of this). Nucleons which share quark wave functions and bound states of more than three valence quarks (“multi-quark clusters”) present in a nuclear environment are examples of such effects.

The result of all these nuclear effects is to change the structure functions from an incoherent sum of the structure functions of the individual nucleons into a more complicated function. In general, these nuclear effects make small parton momentum fractions more probable (the structure functions go up at small x) and intermediate fractions ($0.3 < x < 0.7$) less probable. These effects were first observed by the EMC collaboration and subsequently confirmed elsewhere ([21]).

This thesis focuses on the very high x region. Here the nucleon structure functions must disappear very rapidly due to kinematic constraints. However, if the partons share momentum among nucleons in the nucleus (either through the motion of the nucleon or through the exchange of partons among nucleons), then this constraint disappears and large x events are more likely. In particular, $x > 1$ is possible. Thus, measuring the nuclear structure functions for $x > 1$ is important for understanding these effects.

The data region beyond $x = 0.8$ has been explored rarely and is understood poorly. The BCDMS collaboration has done a measurement of the structure functions at large x and high Q^2 in muon-carbon DIS [1]. The SLAC E133 has measured the structure functions at high x and $Q^2 = 8, 10$ (GeV)² [2]. It was mentioned in section 2.1 the neutrino DIS cross section is basically constant as a function of Q^2 (equation 25). For

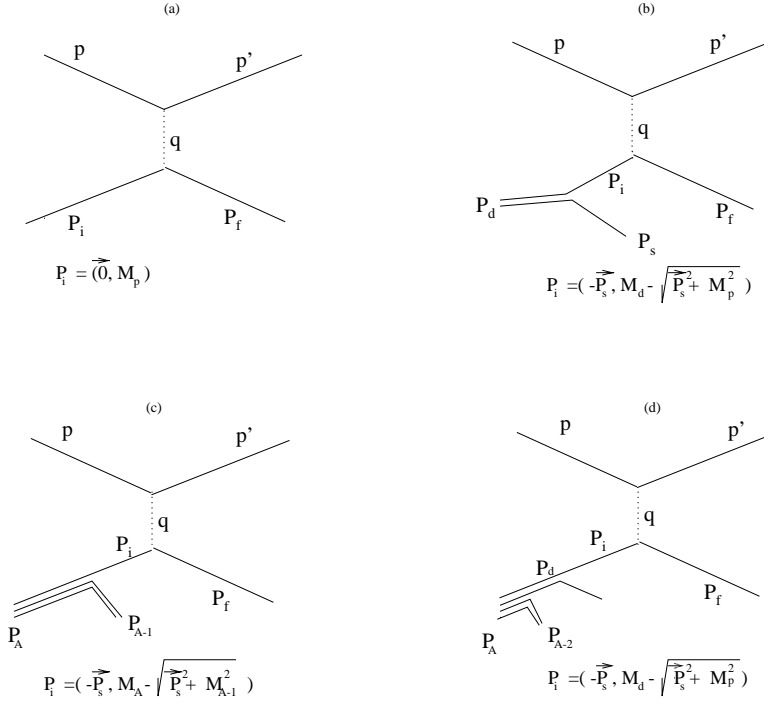


Figure 5: Fermi motion. The effect of other nucleons on the interacting nucleon.

charged leptons however, the cross section falls as $1/Q^4$. Therefore we expect to have a larger sample in the large x and high Q^2 kinematic region than charged lepton DIS experiments.

2.5 Models for High x Structure

The existing models of high x structure are based of generating high nucleon momentum or formation of bags of more than three valence quarks in the nucleus. The “Fermi motion” model and the “few nucleon correlation” are based on the former whereas the “multi-quark cluster” model is based on the latter.

2.5.1 Fermi Motion

Nucleons are known to have relative momenta with respect to nucleus CMF. This motion is referred to as Fermi motion. The nomenclature is because of the similarity of the nucleon momentum distribution to the Fermi gas momentum distribution. The latter is a flat distribution up to the level of the Fermi sphere in momentum space and vanishes beyond that [3]. Modeling the nucleon momentum distribution this way is based on the fermionic behavior of the nucleons. They start filling the lower energy levels in the nucleus, with two opposite-spin nucleons per energy level.

Since a Fermi gas distribution could be true only at zero temperature, an alternative distribution is modeled [4] to include higher momentum components. The high momentum is generated through the formation of quasi-deuteron states in the nucleus. In such a state, the two nucleons could get a high repulsive momentum kick from each other. In both a Fermi gas and a quasi-deuteron state, the spectator (the rest of the nucleus or the remaining nucleon) is assumed to be on mass shell. The constraint set by the total mass of the unit makes the struck nucleon off mass shell. Therefore, “off-shell kinematics” is used to ensure energy-momentum conservation. The nucleon momentum distributions has been experimentally obtained from quasi-elastic electron scattering off heavy nuclei [3].

To illustrate the effects of Fermi motion on DIS processes we consider four different DIS scenarios. The Feynman diagrams for these four cases is shown in Figure 5.

(a) The scattering is from a free proton. The interacting proton is at rest in the

laboratory frame, $P_i = (M_p, \mathbf{0})$ and on the mass shell, $P_i^2 = M_p^2$.

(b) The scattering is from a deuteron. The spectator nucleon is on the mass shell, $P_s = (\sqrt{P_s^2 + M_p^2}, \mathbf{P}_s)$. This causes the interacting nucleon not to be on the mass shell, $P_i = (M_d - \sqrt{P_s^2 + M_p^2}, -\mathbf{P}_s)$.

(c) The scattering is from an off-shell nucleon in the nucleus. The spectator four-momentum is $P_s = (\sqrt{P_s^2 + M_{A-1}^2}, \mathbf{P}_s)$, which is basically the momentum of the rest of the nucleus. The interacting off-shell nucleon has the momentum $P_i = (M_A - \sqrt{P_s^2 + M_{A-1}^2}, -\mathbf{P}_s)$.

(d) The scattering is from a quasi-deuteron state inside the nucleus. The four-momentum of the on-shell spectator nucleon in the quasi-deuteron state is $P_s = (\sqrt{P_s^2 + M_p^2}, \mathbf{P}_s)$, and the interacting off-shell nucleon has the four-momentum $P_i = (M_d - \sqrt{P_s^2 + M_p^2}, -\mathbf{P}_s)$. The rest of the nucleus remains with the four-momentum $P_{A-2} = (M_{A-2}, \mathbf{0})$.

The scenarios of cases “b”, “c”, and “d” show that (except for the case of free nucleon, “a”) there is always a relative momentum component for the struck nucleon in a DIS process. The nucleon momentum distributions, taken from [4], are:

$$|\psi(\mathbf{P})|^2 = \begin{array}{ll} \frac{1}{C} \left[1 - 6 \left(\frac{K_F a}{\pi} \right)^2 \right] & 0 < |\mathbf{P}| < K_F \quad \text{(a)} \\ \frac{1}{C} \left[\left(\frac{K_F a}{\pi} \right)^2 \left(\frac{K_F}{P} \right)^4 \right] & K_F < |\mathbf{P}| < 4 \text{ GeV}/c \quad \text{(b)} \\ 0 & |\mathbf{P}| > 4 \text{ GeV}/c \quad \text{(c)} \end{array} \quad (61)$$

The flat part (equation 61a) represents Fermi motion; the $1/p^4$ part (equation 61b) describes the higher momentum components due to quasi-deuteron states. Both parts can cause an enhancement of observed high x events and in particular can cause $x > 1$

events.

2.5.2 Few Nucleon Correlation (FNC)

All models of short range phenomena in the nucleus are based of nucleon-nucleon (NN) interactions. The reason for this is that unlike the situation in atomic physics, it is not possible to obtain detailed information about the nuclear force by studying the structure of the nucleus. No exact theory on short range effects exists to date. There are ongoing efforts to understand the NN interaction in terms of the quark model but none of these is complete yet [19]. In general, the form of the NN potential could depend on the two positions, momenta, spins, and isospins:

$$v = v(\mathbf{r}, \mathbf{r}', \mathbf{p}, \mathbf{p}', \sigma, \sigma', \tau, \tau') \quad (62)$$

Consideration of different invariances helps one achieve functional forms, a short description of which is given in [19]. However, theories that describe the NN interactions fairly well, fail to account for the structure of nuclei consisting of a large number of nucleons. To describe the structure of the nucleus, phenomenological effective interactions are used which typically depend on the density of the nuclear matter. By the same token these theories cannot be used to describe the NN interactions.

Even though the NN interactions cannot say everything about the structure of the nucleus, looking at these interactions could still give some insight into the nature of the structure. Here we look at some key features of the NN interactions revealed by NN scattering:

- It has a short range of about 1 fm.

- It is attractive with a depth of 40 MeV for larger distances.
- It gets strongly repulsive for distances shorter than 0.5 fm.
- It depends on both spin and isospin of the nucleons.

The distance dependence of this potential is shown in figure 6. The fact that these

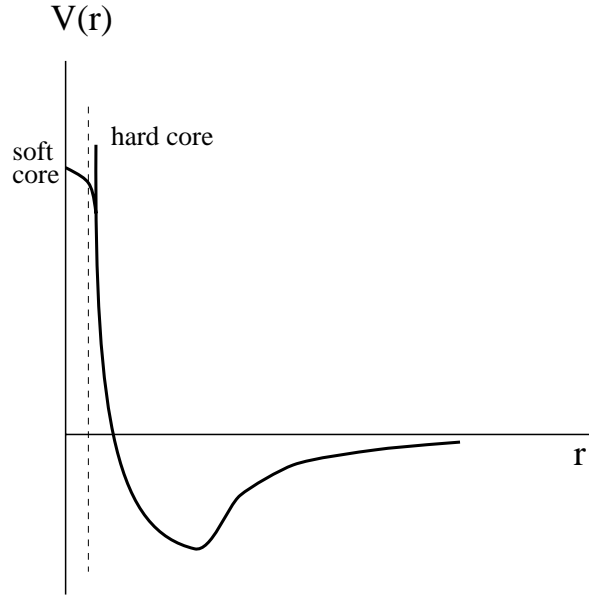


Figure 6: Distance behavior of the nucleon-nucleon interaction potential.

interactions have a hard core, could generate a large relative momentum between two nucleons that happen to be too close together in the nucleus. This is feasible since the NN distance in the nucleus is comparable to the size of the nucleon itself. Therefore, in a DIS process, this could give rise to the lepton probing a high momentum state nucleon. A detailed study of FNC effects in DIS, based on short range nuclear effects is given in [22]. This reference predicts an exponentially falling form for the F_2 structure functions.

2.5.3 Multi-quark Clusters(Bags)

A great deal of theoretical work was done after the observation of the nuclear EMC [21] effect to understand the underlying physics. A class of these theories assumes a sizable probability for the quarks inside the nucleus to tunnel between nucleons. This phenomenon leads to the formation of clusters (or bags) of 6, 9, 12, etc, of quarks. The momentum of the bag is shared amongst its partons. Since a quark in a 6-quark bag could get all the momentum of the bag in a DIS process, x could in principle get as large as 2.

The momentum distribution of the quarks in clusters is usually studied using the MIT bag model or quark models with oscillator potentials [23]. To find a momentum distribution one may assume that the quarks inside the cluster in nuclear matter have some equilibrium distribution. If the number of quarks and quark-antiquark pairs and gluons is sufficiently large then they could be treated as a degenerate Fermi gas with the distribution:

$$n_k^i = \left(\exp \frac{\epsilon_k - \mu_i}{KT} + 1 \right)^{-1} , \quad (63)$$

where k indicates a momentum state and K is the Boltzmann constant. The decay of such a cluster to a system of non-interacting nucleons would correspond to the ground state with $T = 0$. For $(\epsilon_k - \mu_i) \gg KT$, this formula turns to an exponentially falling function. Using this analogy, u and d quarks in a cluster at large momentum state will have the following distribution:

$$\psi_u^2(k) = \psi_d^2(k) \propto \exp \frac{-k}{k_0} . \quad (64)$$

where k_0 is the momentum equivalent of KT in equation 63. For clusters with nonzero isospin the u and d quark distributions can be different.

Assuming that the $3Bq$ quark cluster (where B is the bag number and $3 \times B$ is the number of quarks in the bag) wave function is the product of single-particle functions and taking the quarks to be in s wave to omit the angular variables, the invariant mass will be:

$$M(\mathbf{k}) = (\mathbf{k}^2 + m_q^2)^{1/2} + (\mathbf{k}^2 + m_{3Bq-1}^2)^{1/2} \quad . \quad (65)$$

It is convenient to relate k to the light cone variables k_\perp and

$$z = [(\mathbf{k}^2 + m_q^2)^{1/2} - k_3]/M(\mathbf{k}) \quad , \quad (66)$$

which is the fraction of the cluster momentum carried by a quark in the infinite momentum frame. We assume the static limit $M(\mathbf{k}) = BM_N$ with:

$$|\mathbf{k}| = \frac{1}{2}M_B z \left[1 + \frac{1}{M_B^2} \left(\mathbf{p}_\perp - \frac{1}{2}\mathbf{k}_\perp \right)^2 \right] \quad (67)$$

where p_\perp is the transverse momentum of the cluster. The Bjorken variable $x = q^2/2M_N\nu$ is related to z via:

$$x = Bz \quad (68)$$

where $B = M_b/M_N$ is the ‘‘atomic weight’’ of the cluster.

The cluster structure function F_{2B} (normalized to a single nucleon) is:

$$F_{2B}(x) = \frac{1}{B} \sum_i \int d^2k_\perp \psi_i^2(k_\perp, x) \quad . \quad (69)$$

Using equation 64, the valance quark structure function is:

$$F_{2B}(x) = \rho_v a x \ln[1 + \exp\{-a(x - x_0)\}] \quad (70)$$

where:

$$\rho_v = C_v/B, \quad a = M_N/2k_0, \quad x_0 = \mu/2M_N$$

and C_v is determined by the normalization condition:

$$\int_0^B dx F_{2B}^v(x)/x = 1 \quad . \quad (71)$$

For $a(x - x_0) \gg 1$ the valance quark structure function has the exponential form:

$$F_{2B}(x) = \rho_v a x \exp\{-a(x - x_0)\} \quad (72)$$

This exponentially falling behavior at large x is used in a parameterization for F_2 used for the structure function analysis in this thesis.

3 Experimental Apparatus

3.1 Overview

Neutrinos interact with matter only weakly. The neutrino nucleon cross section is on the order of $\sim 10^{-38}$ cm²/GeV. Two factors are used to increase the number of interactions in neutrino DIS experiments: an intense beam of neutrinos and anti-neutrinos, and a massive target. The Fermilab high energy, high intensity neutrino beam and the CCFR massive detector together serve as tools for neutrino DIS measurements.

3.2 Fermilab Tevatron

The Fermilab mixed neutrino and anti-neutrino beam originates from the Fermilab Tevatron proton beam. Figure 7 shows the Fermilab Tevatron along with the neutrino beam line.

This primary proton beam is a 800 GeV/c, high intensity beam produced from hydrogen gas ionized to H^- ions. The acceleration of the beam is achieved by the following gradation:

- The Cockroft Walton electrostatic accelerator boosts the H^- ions to a momentum of 750 KeV/c.
- The “Linac” (linear accelerator) boosts the momentum of the H^- ions to 200 MeV/c. At the exit point, a carbon foil strips the two electrons off the ions, resulting in a proton beam.
- The Booster, a 140 m diameter synchrotron ring, accelerates the proton beam to a momentum of 8 GeV/c.

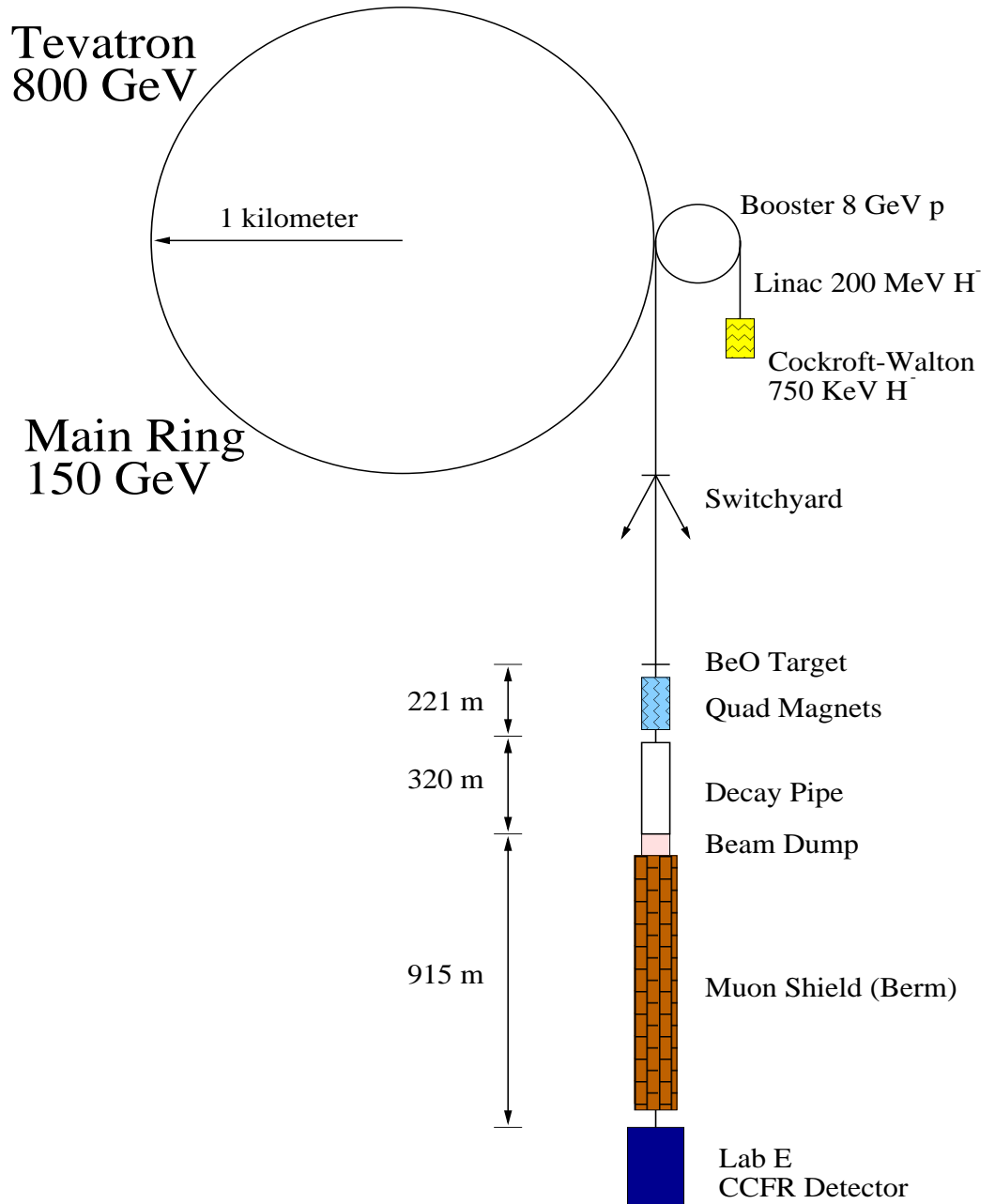


Figure 7: The Fermilab Tevatron and neutrino beam-line.

- The Main Ring, a 2 km diameter synchrotron, accelerates protons to a momentum of 150 GeV/c.

- The Tevatron ring, a superconducting synchrotron, is the final stage where the beam's momentum reaches 800 GeV/c .

The protons are then extracted from the Tevatron in two different modes: slow spill and fast spill. The neutrino beam line uses the fast spill (ping) extraction. Each ping is two milliseconds long. Figure 8 shows one beam cycle.

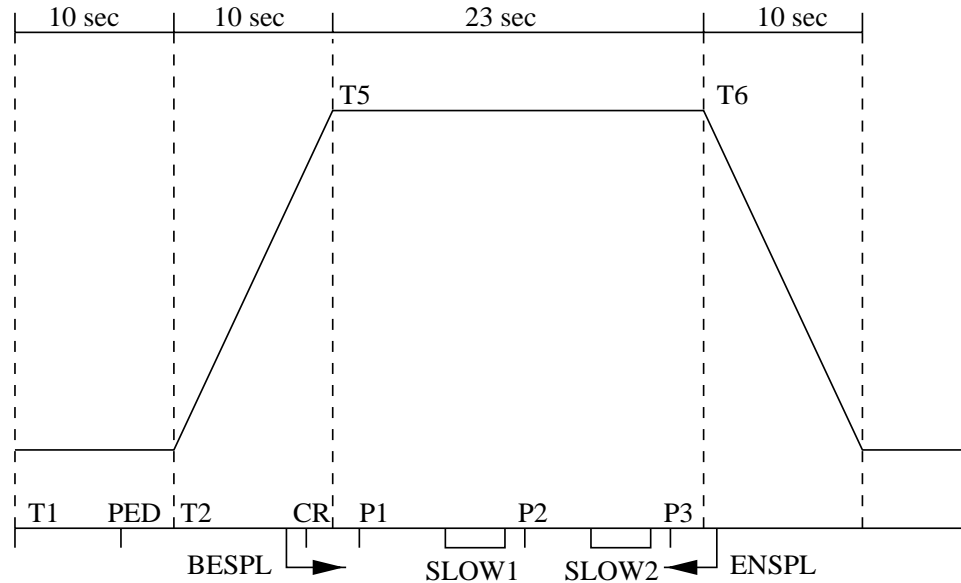


Figure 8: Tevatron magnet current versus time during fixed target operation. P1, P2, and P3 are the ping extraction times. BESPL and ENSPL are the beginning and the end of the spill respectively.

In a 60 second cycle, the Fermilab Tevatron sends pencil size beam with a total intensity of $\sim 10^{13}$ protons in three pings to the neutrino beam line. Fast spill extraction is crucial for neutrino experiments since neutrinos interact only weakly but the background does not necessarily. The background of the neutrino interactions in

the CCFR detector are mostly cosmic ray muons and air showers. In each cycle (three pings) there are about 20 neutrino and anti-neutrino events. The near vertical cosmic ray flux [28] is about $2 \times 10^2 \text{ m}^{-2} \text{ s}^{-1}$. Integrated over the $3 \text{ m} \times 17 \text{ m}$ horizontal cross section of the CCFR detector, this yields about 10 particles per millisecond which is comparable to the neutrino rate. Therefore it is desirable to have all the neutrino interactions in the shortest possible period of time. The neutrino data is taken only during the fast spill.

3.2.1 Fermilab Neutrino Beam Line

The neutrino Quad Triplet⁸ beam line is shown in figure 9 (downstream or to the right of the BeO target) along with the proton primary beam line (upstream of the BeO target). The purpose of this beam line is to capture and focus the secondary beam particles into a parallel beam.

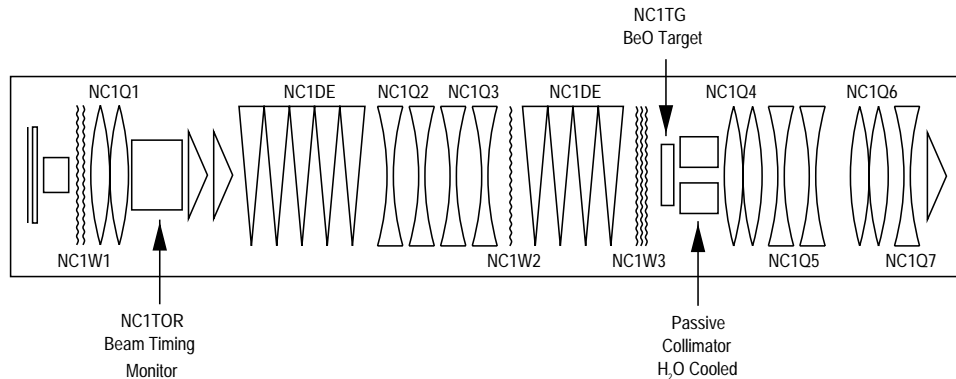


Figure 9: The E770 quadrupole-triplet beam line following the primary proton beam line. Dipole magnets are indicated by prisms and quadrupole magnets are indicated by concave and convex lenses.

The primary proton beam impinges upon a one-interaction length BeO target.

⁸Despite the name “Quad Triplet”, there are really four quadrupole magnets in this beam-line !

Most of the outgoing particles are pions and kaons. More positive mesons are produced than negative. The focusing of the beam is done by means of four quadrupoles. After the magnetic elements, the beam enters a 320 m long, 1.83 m wide, decay pipe. Here a large fraction of pions and kaons decay. The muon neutrinos and anti-neutrinos (ν_μ and $\bar{\nu}_\mu$) are produced mainly in the following decay modes⁹:

$$\pi^+ \longrightarrow \mu^+ , \nu_\mu \quad 99.9\% \text{ Branching Ratio}$$

$$K^+ \longrightarrow \mu^+ , \nu_\mu \quad 63.5\% \text{ Branching Ratio}$$

along with their corresponding CP decay.

After the decay pipe there is a 1 km long shield of dirt, fortified with concrete and lead. All the charged and neutral particles in the beam are absorbed in this berm except for neutrinos and anti-neutrinos. The neutrino and anti-neutrino event rates are shown in figure 10.

⁹A small fraction of the beam's muon neutrinos and anti-neutrinos is produced in three body kaon decays, known as $K_{\mu 3}$ decays.

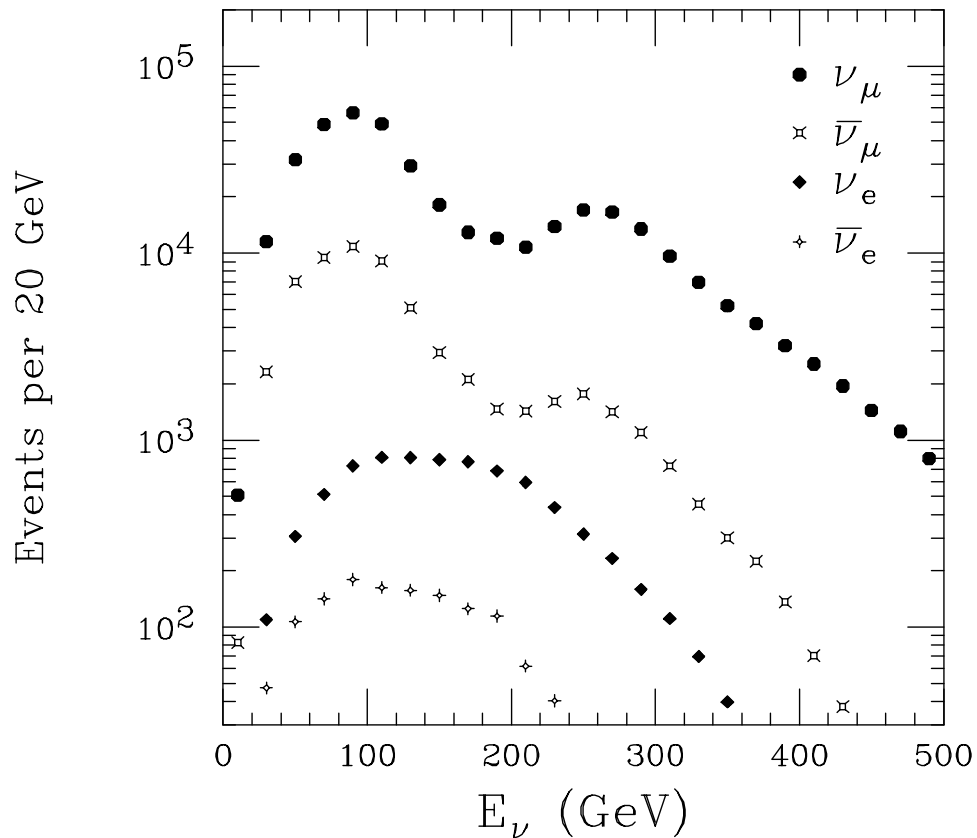


Figure 10: The neutrino and anti-neutrino event rates in the CCFR detector. The muon neutrinos and anti-neutrinos (ν_μ and $\bar{\nu}_\mu$) come predominantly from two body decays of pions and kaons. The electron neutrinos and anti-neutrinos (ν_e and $\bar{\nu}_e$) come from the three body decays of kaons and the muon decays.

3.3 CCFR Detector

The CCFR detector is a relatively coarse and massive detector designed for high statistics measurements of neutrino and anti-neutrino DIS interactions. It consists of a 690 ton target calorimeter followed by a toroidal magnet spectrometer (figure 11).

The energy of the hadronic shower plus the angle of the outgoing muon are measured in the target calorimeter. The toroidal magnet spectrometer is used to measure the momentum of the outgoing muon.

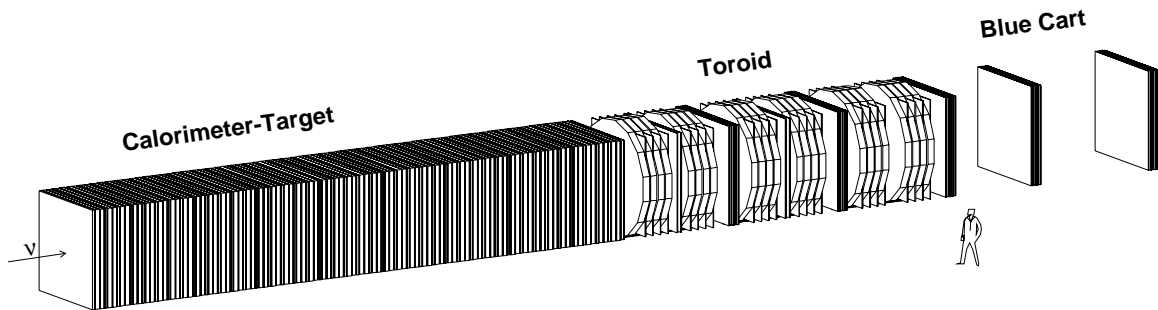


Figure 11: Schematic representation of the CCFR detector. The neutrino beam enters from the left. The target-calorimeter is on the left and the muon spectrometer (toroid) is on the right. The two rightmost sets of drift chambers are known as the blue cart.

3.4 Target Calorimeter

The target calorimeter of the CCFR detector is built to serve the following purposes:

- a massive target for the neutrino beam;
- a calorimeter to measure the total energy of the hadronic shower;
- a device to measure energy loss of the penetrating muon; and
- a tracker to measure the position of the outgoing muon throughout the target.

The target calorimeter consists of 690 tons of steel in the form of 5.15 cm thick plates, 84 liquid scintillation counters, and 42 drift chambers. The calorimeter cross section is a square 3 m by 3 m and has a length of 17.7 m. The steel slabs are distributed throughout this length and are interspersed with scintillation counters and drift chambers. Figure 12 shows the arrangement of these elements.



Figure 12: Layout of a CCFR target module. A scintillation counter is positioned after every two steel plates and a drift chamber is found after every four.

3.4.1 Scintillation Counter

Figure 13 shows the schematic sketch of a CCFR scintillation counter. The 2.5 cm thick scintillation counters are acrylic tanks filled with mineral oil doped with scintillation fluors. Traversing charged particles excite the primary fluors and they radiate ultraviolet light. This radiation is absorbed by secondary fluors which in turn radiate blue light with a longer attenuation length of ~ 50 cm. This light is transferred to the edges of the counter by total internal reflection. The blue light is then absorbed by plastic bars, called “wave shifter bars” which emit green light instead. The wave shifter bars finally act as a wave guide to transfer the light to the four corners of the counter. The four photo-multiplier tubes (PMT) at the corners collect the light output of the counter.

The PMT signal is digitized by Fast Encoding Readout, Analog-Digital Converters

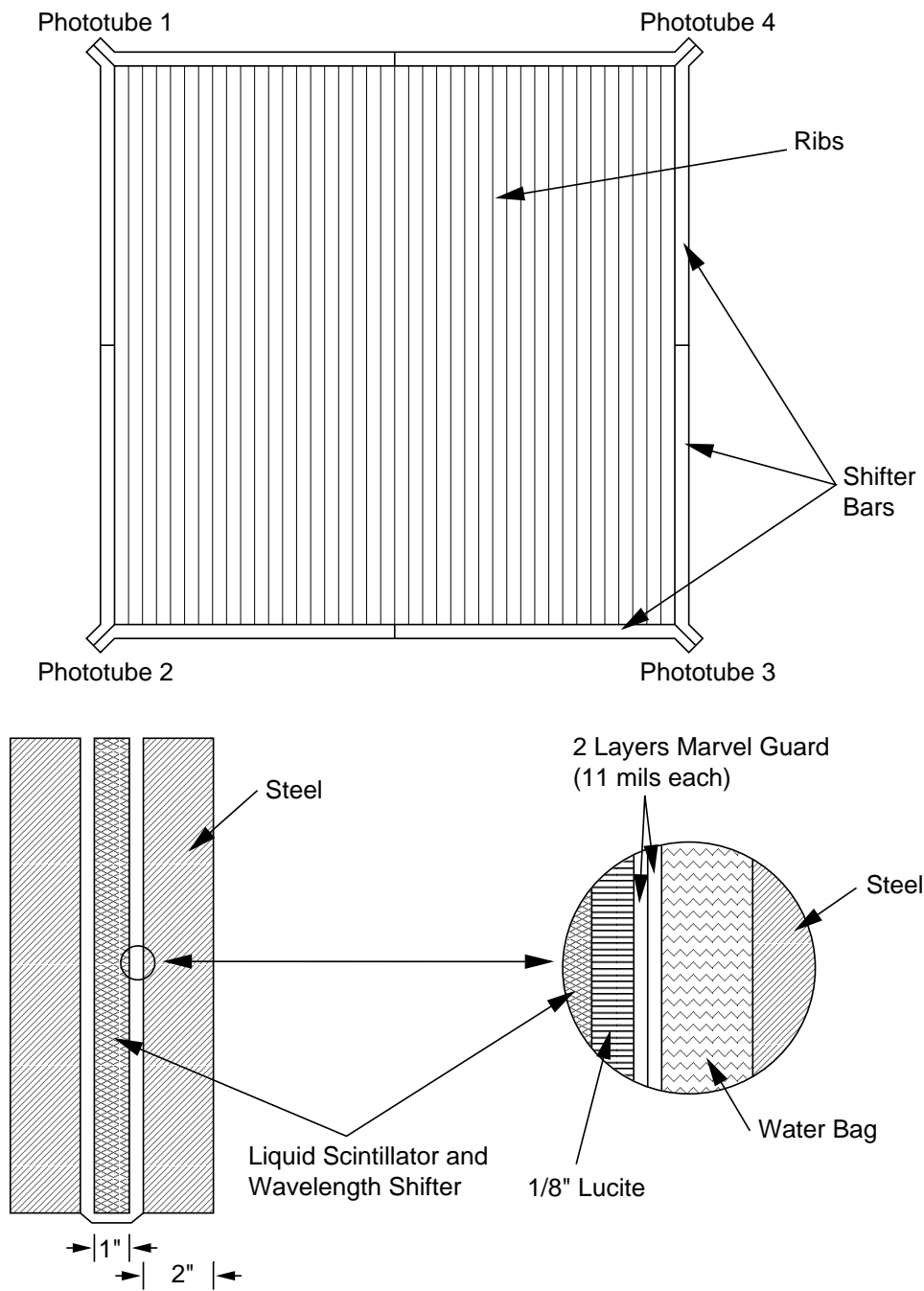


Figure 13: Schematic sketch of a scintillation counter. Four PMT's at the four corners collect the light output carried by wave shifter bars.

(FERA ADC system, LeCroy 4300, 4301, 4302) with 11 bits of dynamic range. The charge integration time of an ADC is 215 ns. The time it takes for the capacitor to discharge through a resistor is the basis of analog-digital conversion. The digitization takes $8.5 \mu\text{s}$. Another $3.2 \mu\text{s}$ is needed to buffer the data, resulting in $11.7 \mu\text{s}$ of read-out time.

Figure 14 shows the logical diagram of the FERA system readout of a counter. The analog signal from each PMT is read out in a “low” gain ADC. The analog sum of the four PMT signals in each counter is digitized twice. First it is directly digitized into a “combination low” ADC channel. It is also amplified by a factor of 10 and digitized in a “high” ADC channel. The signals from similar corners of several counters PMT signals are attenuated by a factor of 10 and summed into “Superlow” signals.

The variation in readout sensitivity allows for different sensitivity measurements. A typical hadron shower produces between 1000 to 2000 ADC counts. If the signal is greater than $2^{11}=2048$ counts, the super-low channels are used to measure the deposited energy. The high channel is used to measure the energy deposited by muons. This energy ($\sim 2 \text{ MeV}/(\text{gm}/\text{cm}^2)$) is too small to be measured by the low channels. For triggering, the combination-low signal is amplified by a factor of 100. The produced signal is called scintillator-bit or “s-bit”.

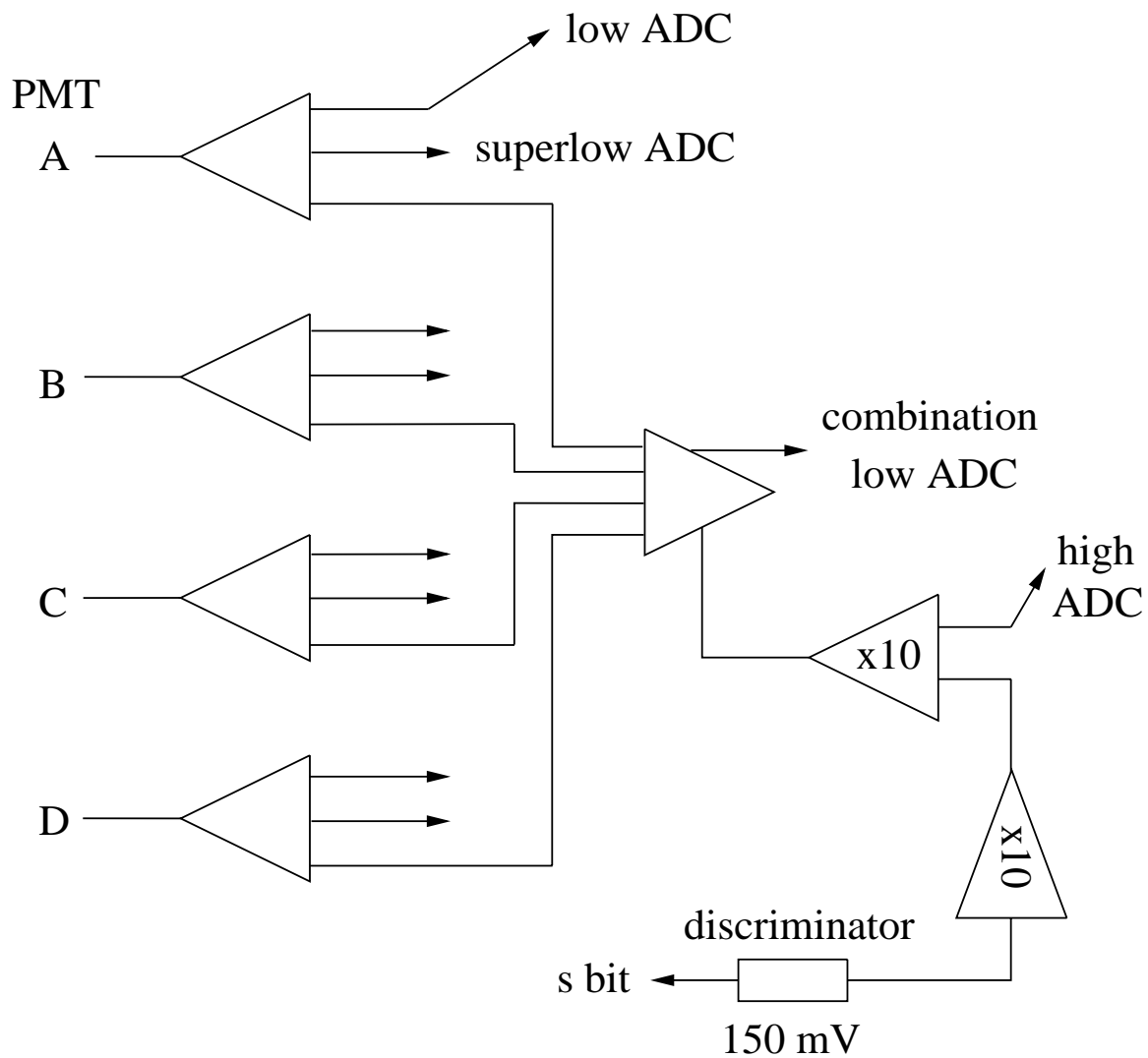


Figure 14: Readout electronics for a scintillation counter. Each counter is digitized by seven ADC channels. The threshold of the s-bit discriminator is set at one quarter minimum ionizing level.

3.4.2 Drift Chambers

There are 42 drift chambers inter-spaced throughout the calorimeter which are used to measure the position of the outgoing muon as it traverses the calorimeter. Figure 15 shows the schematic of a drift chamber.

Each drift chamber has two planes, x and y, consisting of 24 two-wire cells. These two sense wires are 30 μm diameter gold-plated tungsten and are kept at +1750 Volts. There is field shaping wire kept at +350 Volts between the two sense wires in each cell. The cathodes are strips of copper clad on the G-10 cover and are held at specific voltages to create a 690 Volts/meter uniform electric field. The G-10 cover is supported by parallel aluminum I-beams kept at -4500 Volts.

The chambers use a 50-50 argon/ethane gas, a mixture of a noble gas that does not have rotational or vibrational excitation modes, and a quenching organic compound. When a charged particle passes through a chamber, the atoms (mostly argon) in the gas get ionized. The liberated electrons drift toward the anode wires and ionize other atoms. An avalanche of electrons is produced this way. The ethane atoms de-excite the argon before it can produce X-ray. The avalanche of electrons induces a “signal” voltage on the sense wire.

The signal on the hit wire is amplified immediately at the pre-amplifier cards located on the chambers. It is then sent to two coupled time-digital converters. To measure the position to an accuracy better than the cell size, the drift times are used. The drift time is measured on the basis of the delay between the event time (from

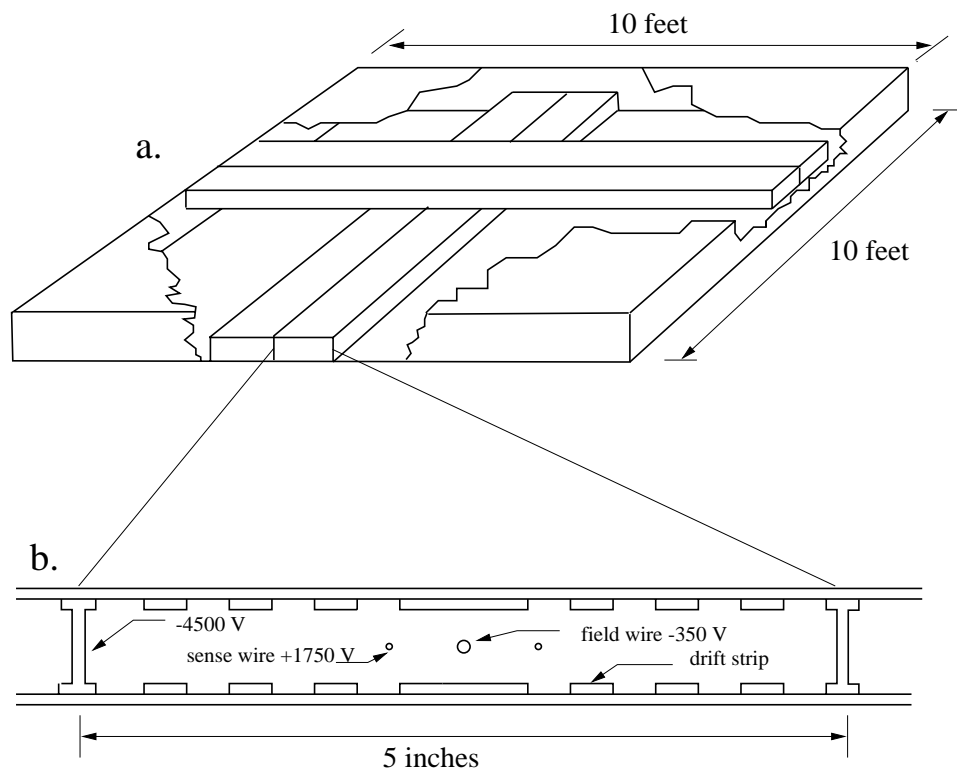


Figure 15: **(a)** CCFR target drift chamber. There are two orthogonally oriented planes for each chamber consisting of three-wire cells. **(b)** A three-wire drift chamber cell.

the scintillation counter signal) and the registration of the drift chamber signal. The two sense wires in the cell remove the left-right ambiguity of the hit.

3.5 Toroidal Magnet Spectrometer

The magnet spectrometer of the CCFR detector measures the momentum of the outgoing muon as it emerges from the calorimeter. The average energy loss of a muon in the CCFR detector is about ~ 10 GeV. Most of the muons, therefore, make it through the calorimeter. If they remain inside the fiducial volume of the detector, the muons then traverse the momentum spectrometer. The spectrometer consists of three toroidal iron magnet segments and five sets of drift chambers. After each magnet segment, there is a set of drift chambers which measure the position of the muon. Two additional sets of chambers, 3 and 7 meters further downstream of the end of the toroid, are used to measure the final angle of the muon after it is bent in the magnet.

Each magnet consist of eight cylinders, 20.3 cm thick and 3.6 m in diameter. There is a 25 cm diameter hole in each cylinder. The magnet iron is magnetized to saturation by four copper coils. Each coil carries a DC current of 1500 A. The magnetic field ranges between 1.55 Tesla near the outer radius, to 1.9 Tesla near the center of the cylinder. The average value of the field is about 1.7 Tesla. The field is azimuthally symmetric throughout the magnet except for a small deviations near the two iron legs which support the magnet.

As a muon traverses the length of the toroid, it gets a transverse momentum kick

of about 2.4 GeV/c. The muon momentum, p in GeV/c, is roughly given by the following formula:

$$\theta_{bend} \sim \frac{p_{kick}}{p} \sim \frac{2.4 \text{ GeV/c}}{p} . \quad (73)$$

4 Data Analysis

4.1 Overview

The topology of a neutrino charged current event in the CCFR detector is depicted in figure 16. A neutral current event is also shown in the picture for contrast. The typical charged current event consists of three parts. The most upstream part is the hadronic energy shower region in the calorimeter where the shower particles are absorbed. This is followed by the portion of the calorimeter where the muon travels in a relatively straight line. Finally there is the toroid spectrometer where the muon is bent by the magnetic field. The hadronic energy is measured in the hadronic shower region. The muon production angle is measured in the remainder of the calorimeter. The muon momentum is calculated from the bend of the track in the toroid.

4.2 Hadronic Energy Measurement

The hadronic energy in a neutrino DIS event in the CCFR detector is measured via the energy deposited in the scintillation counters in the target calorimeter. If the event occurs within the fiducial volume (away from the edges), the hadronic shower is completely contained within the calorimeter. The produced hadrons travel through and interact in slabs of steel, scintillation counters, and drift chambers. The hadronic energy measurement is based on measuring the energy deposited in the counters, and from it, inferring the original hadronic energy. The counters sample about 3% of the energy of the hadronic shower.

The response of a counter is not the same everywhere in the counter; it is higher

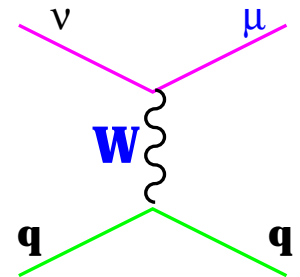
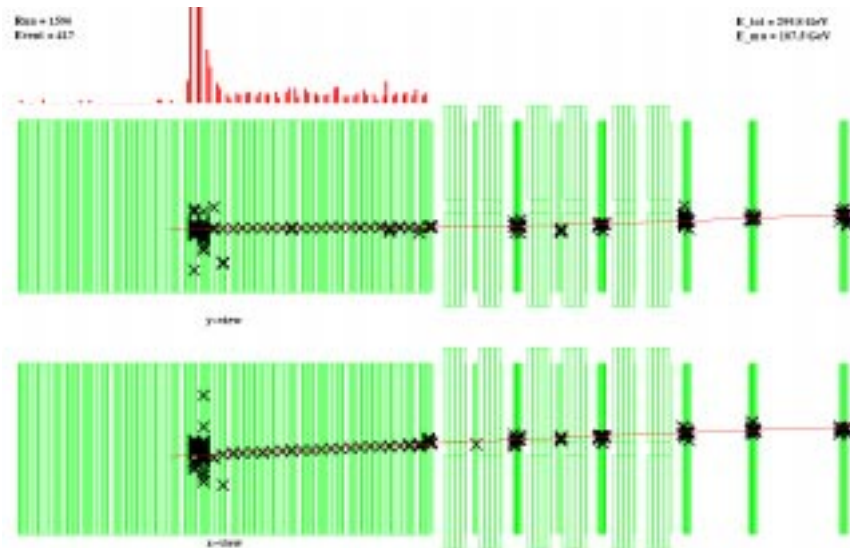
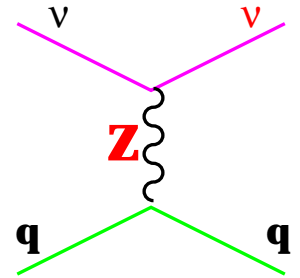
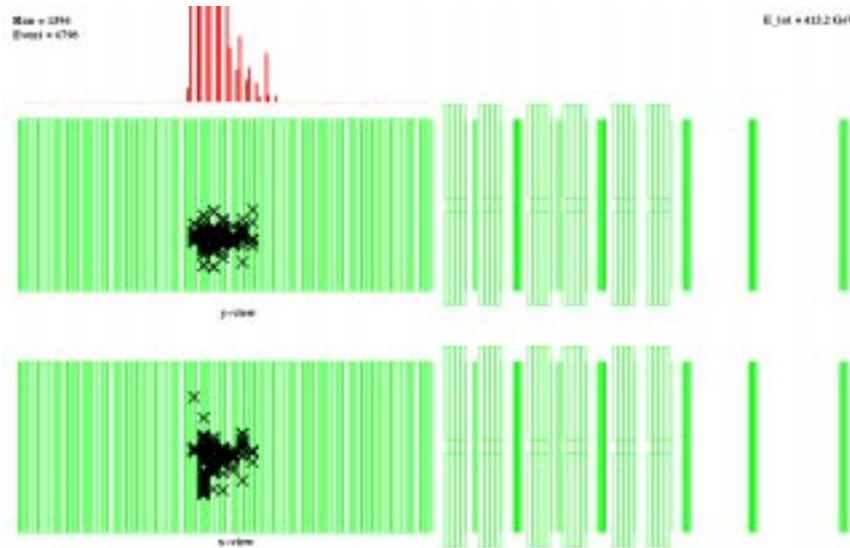


Figure 16: Event displays of charged current event (bottom of the page) in the CCFR detector, used for the structure function analysis. A neutral current event is also shown (top of the page) for contrast.

near the edges where phototubes are located and lower in the middle. For an accurate measurement of the hadronic energy one has to correct for the variations of a counter's response across the face of the counter. Then, variations from counter to counter also have to be corrected. Finally, time variations in the response should be accounted for. These corrections result in a uniform energy measurement throughout the detector and in the course of time. The corrections are done by continuous calibration of the counter gains with a sample of muons. A special trigger was designed to register "straight through" muons. These muons are produced from neutrino charged current interactions in the berm upstream of the detector. They usually traverse the whole length of the detector and are momentum analyzed in the toroid. The energy of the sample is $75 < E_\mu < 200$ GeV. For a high energy muon the amount of the deposited energy in a scintillator is almost constant and does not vary much with energy. This amount is referred to as "minimum ionizing particle" or MIP response. Using the muons, corrections to the gain of each counter in different positions were made.

The overall calibration of the calorimeter as a hadronic measurement device was done with test beam hadrons. The measured energy in the calorimeter is compared with that determined from the test beam spectrometer. The gains are calibrated using this comparison.

4.2.1 Counter Gain Calibration

Different counters have different responses to the passage of charged particles. This is due to the slight geometric and phototube gain differences and electronics differences

in the amplifying and summing circuits. The counter response to MIP varies within a single counter as well. This is due to various factors such as attenuation of the light in the scintillator oil, and different phototube responses. Finally the response may change with time because of the degradation of the scintillation oil and the time variations in the phototube gains. Therefore each counter gain (response to MIP) is calibrated separately. The calibration is done as function of the position in the counter and of time.

Muons are used for gain calibration. The muon energy loss spectrum is a Landau distribution (figure 17). The long tail of the distribution is due to stochastic losses from bremsstrahlung, pair production, and delta-ray production. The muons were

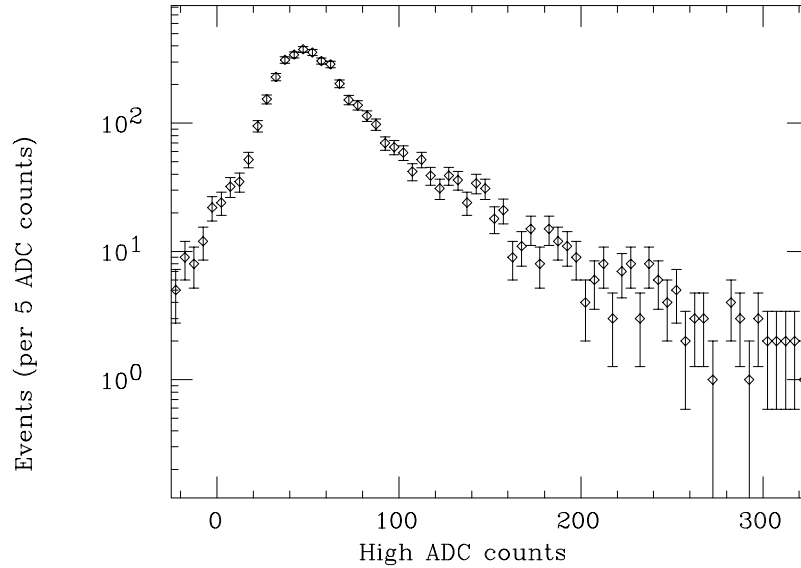


Figure 17: Muon energy loss distribution in a scintillation counter.

momentum analyzed in the toroid spectrometer and small energy dependence corrections were made. The counter’s response to MIP is determined from the “truncated

mean” of the muon energy loss distribution. This eliminates the stochastic part of the muon energy loss. To determine the truncated mean, an iterative process has been used. In each step the data between 0.2 and 2.0 times the previous mean are used to determine the new mean. This is continued until the mean converges. The truncated mean is then taken to be equivalent to one MIP in the counter. This mean is position and time dependent and is denoted by $\Delta E_i(x, y, t)$.

To make the response of a counter uniform the response at different positions in the counter are normalized to that of the center. Each counter is segmented into squares of 22.9 cm \times 22.9 cm. The MIP response in each segment is then measured. The map of the ratio of the response at position (x, y) to the response at the center, $(x, y) = (0, 0)$ at $t = 0$ is formed:

$$R_i^{map}(x, y, 0) = \frac{\Delta E_i(x, y, t = 0)}{\Delta E_i(0, 0, t = 0)} . \quad (74)$$

This is called a “counter map” and is used to make the counter response uniform. A typical counter map is shown in figure 18. Contours in the figure show the response of different segments relative to the center. As seen from the map, the response is higher toward the edges than in the center because of proximity to the phototubes.

The time variations are handled by frequent measurements of the phototube gains. These measurements were done in the center of each counter where the rate is highest. The response at the center of all counters are then normalized to get uniform MIP response in the entire detector.

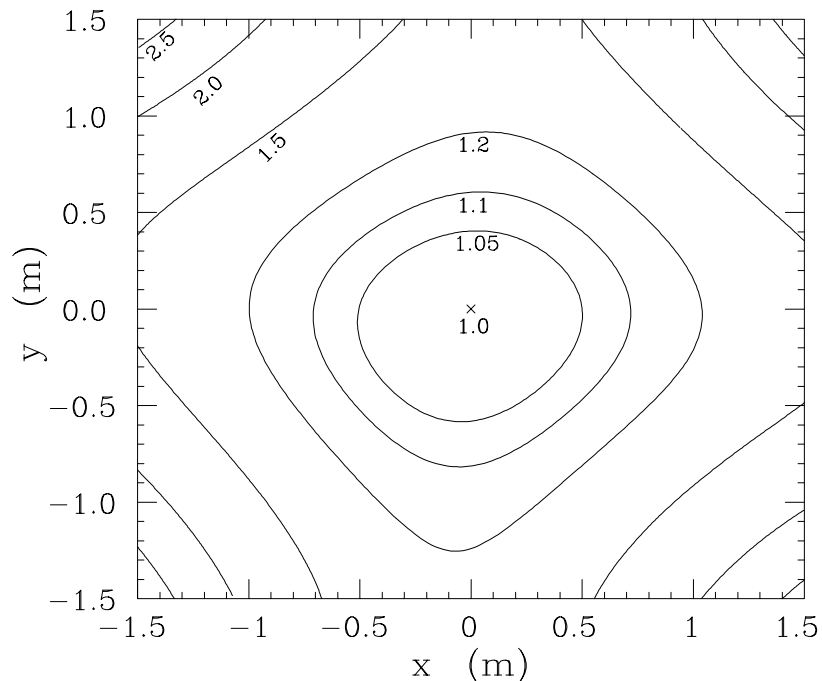


Figure 18: Relative muon response for counter number 37. The contours show the response of the region relative to the response in the center of the counter. The response is higher near the edges because of proximity to the phototubes.

4.2.2 Calorimeter Energy Calibration

The absolute calibration of the calorimeter was done with the test beam of hadrons [33]. The whole length of the calorimeter was scanned. The test beam (Fermilab NTW beam) was a secondary beam of mostly pions. The proton content of the beam was about 20% at 100 GeV/c and it grew with the beam energy. The electron content of the beam was about 10% at 50 GeV/c and higher at lower energies.

The target calorimeter consists of six identical movable segments. The entire calorimeter was moved out of the test beam path and different calorimeter segments were moved in the path for calibration. All six parts were calibrated independently.

The energy response of the calorimeter was measured by comparing the hadrons'

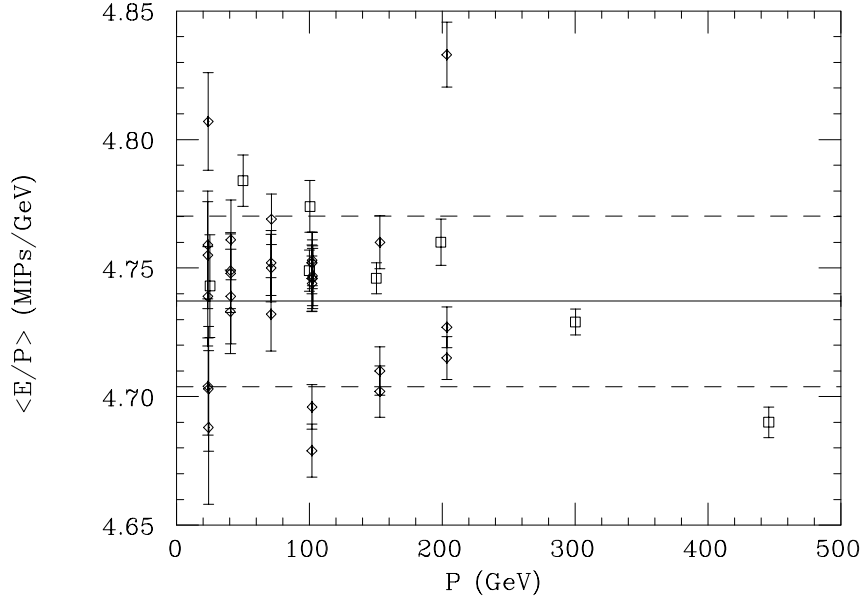


Figure 19: Energy response of the calorimeter for E744(squares) and E770(diamonds). The mean is 4.74 MIP's per GeV. The fractional deviation for E770 is about 0.7%.

momenta and the measured energy in the calorimeter. Figure 19 shows the ratio of the calorimeter energy to the test beam momentum, $\langle E/p \rangle$, as a function of the test beam momentum, p . The ratio is constant within 1% and the MIP-to-GeV conversion factor is about 4.74 MIP's/GeV. Hence the response of the calorimeter is known to 1%. No measurement differences were seen in different segments. The distributions of the measured energy for 25 and 200 GeV/c momentum analyzed beam are shown in figure 20.

The energy resolution was found to be:

$$\frac{\sigma}{E} = \frac{0.847 \pm 0.015}{\sqrt{E}} + \frac{0.30 \pm 0.12}{E} \quad (75)$$

where E is in GeV. The first term represent the sampling fluctuation and the second

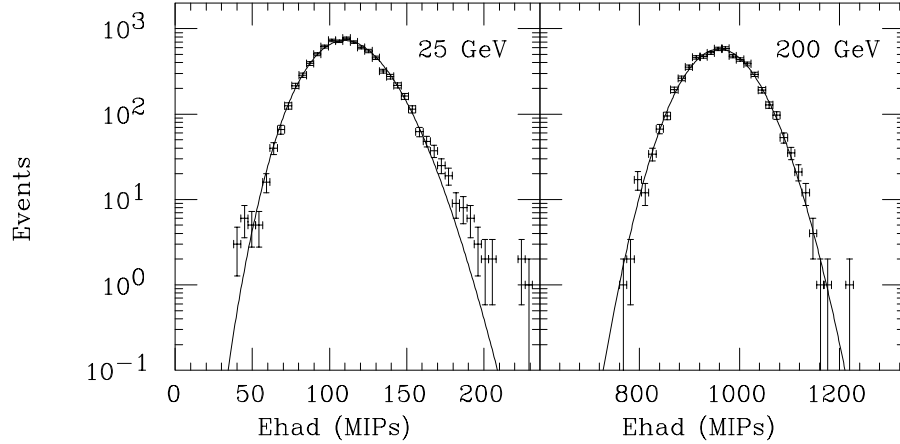


Figure 20: The Calorimeter measured energy distributions of 25 and 200 GeV test beam hadrons. The particles were momentum analyzed in the test beam spectrometer independently. The curves represent Poisson-like parameterizations of the resolutions.

one is from the electronics noise. Different values of $\frac{\sigma}{E}$ are shown in figure 21.

The calorimeter's response to electromagnetic shower was calculated from the electron component of the 25 and 50 GeV test beam [33]. The resolution was found to be:

$$\frac{\sigma_e}{E} = \frac{0.60}{\sqrt{E}} \quad . \quad (76)$$

Type of Signal	Calibration (MIP/GeV)	σ/E
π	4.73 ± 0.02	$0.847/\sqrt{E} + 0.03/E$
e	5.25 ± 0.10	$0.60/\sqrt{E}$
μ	6.33 ± 0.17	0.17

Table 2: CCFR calibration constants and resolutions for hadronic, electromagnetic, and MIP energy deposition in the target calorimeter.

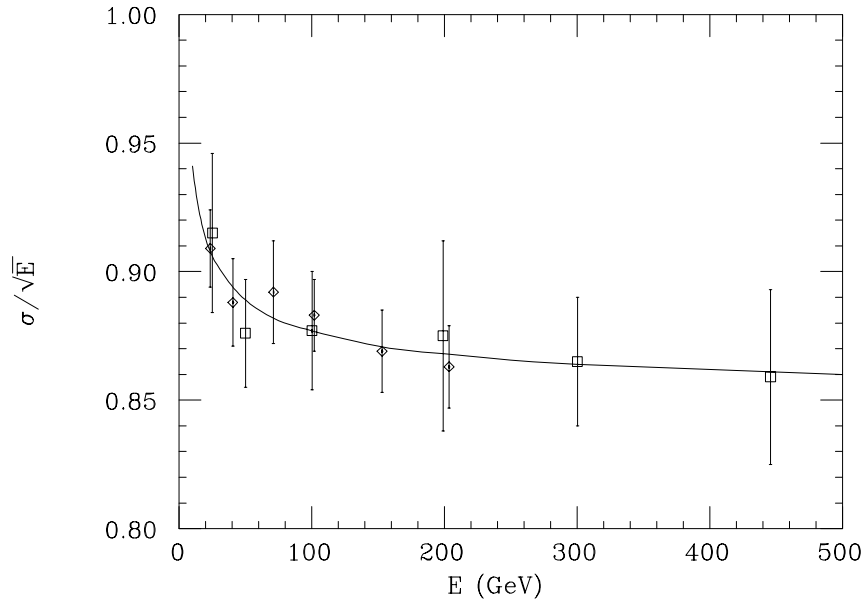


Figure 21: The hadronic energy measurement resolution of the calorimeter. The curve represents the fit of equation 75.

Finally the detector response to minimum MIP was measured with a sample of range-out muons. In this sample, low energy muons from charged current events emerge away from the hadronic shower but their energy is small and they get absorbed in the target [34]. Since they have small energy, the muons are assumed to deposit energy only through ionization. The average deposited energy in a counter is therefore taken to be basically one MIP. The resolution for this sample was found to be

$$\frac{\sigma_{\mu}}{E} = 0.17 \quad . \quad (77)$$

Table 2 shows the CCFR calibration constants for hadronic showers (π), electromagnetic showers (e), and MIP (μ). The given error values contain statistical and dominant systematic errors from [33] and [34]. The ratio of electromagnetic to

hadronic response in the calorimeter, denoted by e/π , is 1.1.

4.3 Hadronic Energy Calculation

To measure the hadronic energy from the counter pulse heights the hadronic shower region is first determined. Two variables are used to determine the shower region: PLACE and SHEND. PLACE indicates the beginning of the shower. It is the counter before the most upstream counter with 4 MIPs energy deposition. SHEND (short for “SHower END”) indicates the end of the shower region. This is the first counter downstream of PLACE, which is followed by three consecutive counters with less than 4 MIPs energy deposition. The shower region is then defined to be from PLACE down to 5 counters after SHEND . This inclusion of the extra 5 counters is to account for the low energy particles at the end of the shower.

Once the shower region is isolated, the hadronic energy is calculated by adding the LOW (section 3.4.1) pulse heights in the shower region. A pulse height of one MIP is attributed to the muon energy in each counter and is subtracted from the hadronic energy.

4.4 Muon Angle and Momentum Measurement

The passage of a muon in the CCFR detector has a clear signature. Muons are penetrating particles; muon average energy loss in a medium is about $2 \text{ MeV}/(\text{gm}/\text{cm}^2)$. Therefore the muons normally traverse the whole length of the detector, losing about 10 GeV of their energy in the process. In this analysis we require that the muon have

a track in the target calorimeter and all segments of the toroid spectrometer. There is a minimum muon energy cut of 15 GeV but the average muon energy for large x and large Q^2 sample is much higher than that.

The measurement of the muon angle and momentum are interdependent. The momentum measurement is based on the angles with which the muon enters and leaves the toroid. The beginning of the muon track in the toroid is the end of the calorimeter track. This makes the momentum measurement dependent on the angle measurement in the calorimeter.

The muon trajectory in the calorimeter and the toroid is subject to Multiple Coulomb Scattering (MCS). MCS is the result of Coulomb forces from the nuclei on the muon. It causes the muon to go through many small deflections as it travels through matter. The size of these deflections depends on the muon momentum and this makes the error on the angle measurement depend on the momentum measurement.

4.4.1 Muon Tracking and Angle Measurement in the Calorimeter

The muon tracking in the target calorimeter and toroid are done using the hits in the drift chamber. In the calorimeter, the muon track is a straight line subject to MCS. Since it is impossible to find the muon drift chamber hits in the hadronic shower region, the fitting starts from the most downstream end of the calorimeter. The track is then extrapolated toward the centroid of the shower region by searching for in-time hits in the next upstream chambers. If no hit is found in one chamber, that

chamber is skipped and the search continues in the next upstream one. The chamber efficiencies are normally very high (above 98%) and usually all chambers register hits. The upstream end of the track is taken to be between the PLACE and the counter upstream of that. For high hadronic energy ($E_{had} > 50$ GeV), all but the two most upstream chambers are used in track reconstruction. For hadronic energy range of $25 < E_{had} < 50$ GeV, only the most upstream chamber is eliminated.

In the next step the MCS effects are taken into account. The calorimeter tracking formalism uses the first pass toroid momentum measurement, p_μ , to find the MCS deflection width:

$$\sigma_i = \frac{0.015}{p_\mu} \sqrt{L_i/X_0} \quad , \quad (78)$$

where X_0 is the radiation length of the medium and L_i is the length of material between hits. The mean MCS deflection over each track segment was used to form the χ^2 function:

$$\chi^2 = \sum_i \frac{(x_i - x_i^p)^2}{\sigma_i^2} \quad (79)$$

where the x_i are the chamber hit positions and the x_i^p are the fitted track positions.

To fit the track the χ^2 function is minimized.

The line fitting the six most upstream chamber hits is used to determine the muon angle. The track angle at the front face of the toroid is determined using the six most downstream target chambers. The procedure is iterated, using the new p_μ from the toroid measurement in each step, until the angles converge.

The tracking accuracy is limited by MCS and the hadronic shower. The hadronic

shower effect on tracking is worst at high hadronic energies due to higher hit multiplicity. As seen from equation 78, the MCS effects are most severe at lower muon momenta where the deflections are more significant compared to the muon momentum.

The muon angle measurement resolution was determined from the “straight through” muon sample (section 4.2). The angular resolution was determined by taking the middle of the track in the calorimeter and comparing the angle found from the downstream portion with that of the upstream portion of the muon track. The actual resolution in a charged current event depends on the size of the hadronic energy. This is because for larger E_{had} , one or two chambers closest to the event vertex are eliminated. It also depends on the muon track length. At least 6 chamber hits are needed for the best resolution. Therefore high E_{had} events need at least 7 or 8 chamber hits for best measurement. A quantitative analysis [6] shows that the resolution can be parameterized as:

$$\sigma_{\theta} = a + \frac{b}{p_{\mu}} K \text{ (mrad)} \quad , \quad (80)$$

where a and b are functions of the hadronic energy and track length as given in table 3.

4.4.2 Muon Energy Measurement

Since the muon momentum measurement is based on the bending angle of the muon in the toroid, an accurate knowledge of the magnetic field of the toroid is necessary.

To achieve this a map of the magnetic field was prepared by numerous Hall probe

Track Length (chambers)	$E_{had} < 25$ GeV		$25 < E_{had} < 50$ GeV		$E_{had} > 50$ GeV	
	a	b	a	b	a	b
4	.535	35.4	.547	46.0	.407	75.0
5	.366	49.5	.393	57.3	.343	77.8
6	.294	56.6	.361	59.4	.260	84.9
7	.235	61.5	.337	62.2	.235	87.0
8	.235	61.5	.337	65.8	.235	87.7

Table 3: Muon angular resolution parameters. These are used in equation 80 to find the resolution for different muon momenta and traveling lengths in the target calorimeter.

measurements at different positions. Also the electrical current in the magnet coils were measured. These two gave an accurate knowledge of the relative strength of the magnetic field as a function of position. To normalize the magnetic field values, test beam muons were used.

A simplified version of the muon momentum determination and resolution measurement is as follows. As the muon traverses the entire toroid which is 500 cm of steel, it gets about 2.4 GeV/c transverse momentum. Therefore the momentum is:

$$p_\mu = \frac{p_\perp}{\theta_{bend}} = \frac{2.4 \text{ GeV}/c}{\theta_{bend}} \quad , \quad (81)$$

The momentum measurement errors are due to two different effects. Up to several hundred GeV/c, the error is dominated by the MCS effect. The muon angular deflection due to MCS is about:

$$\theta_{MCS} = \frac{0.015}{p_\mu} \sqrt{500/1.76} = \frac{0.25}{p_\mu} \quad . \quad (82)$$

where 500 cm is the total length of the toroid steel and 1.76 cm is one radiation length

in steel. Therefore the resolution can be estimated as:

$$\frac{\sigma}{p_\mu} = \frac{\theta_{MCS}}{\theta_{bend}} \approx 10\% \quad . \quad (83)$$

The size of this effect is independent of the muon momentum. At very high energies however, a second effect sets in which depends on position measurement resolution before and after the bend. This error is caused by the fact that at very high energies the error on the bending angle is comparable with the angle itself. For the CCFR toroid, this term gets significant near TeV energies [35] which is out of the range of the data sample used in this analysis.

The actual momentum measurement algorithm starts with finding a first pass momentum estimate from the bending angle in the first toroid segment. The entering position and angle of the track are taken from track fitting in the target. The exiting position is taken from drift chamber hits right after the first toroid segment. The first pass momentum is calculated via the formula:

$$p_\mu = \frac{0.3\langle B\rangle L_k}{\Delta\theta_{bend}} \quad , \quad (84)$$

where L_k is the distance traversed in the magnetic field in centimeters, and $\langle B\rangle$ is the average magnetic field strength in kilogauss, namely 17 kG. This is used in the next iteration tracking which includes MCS effects. In the following iterations of the toroid track fitting and momentum finding, all magnets are used. The muon trajectory is extrapolated through the magnets in steps of 10 cm. The muon energy loss is each

step is taken into account via the formula:

$$\Delta E_\mu = LENGTH \times \left(1.27 \times 10^{-2} + 1.27 \times 10^{-3} \times \ln(p_\mu) \right) \quad , \quad (85)$$

where $LENGTH = 10$ cm. This is a parameterization of the average muon energy loss in the steel. It has a constant term corresponding to MIP loss and a term that depends on energy logarithmically to take catastrophic losses into account. In each step the intermediate value of p_μ is used to calculate the χ^2 function for track finding in the target and the toroid as well. This is done by comparing chamber hit positions and the predicted track. The toroid χ^2 function is formed via the formula:

$$\chi^2 = \sum_i \sum_j (x_i - x_i^p) M_{ij}^{-1} (x_j - x_j^p) \quad , \quad (86)$$

where the x_i are the chamber hit positions and the x_i^p are the fitted track positions. M^{-1} is the inverse of the error matrix M . The full error matrix M , including correlations among chamber hit positions, is defined as:

$$M_{ij} = \langle (x_i - x_i^p)(x_j - x_j^p) \rangle = \sum_{k=1}^i \sigma_k^2 \left[\frac{L_k^2}{3} + f L_k 2(z_{kj} + z_{ki}) + z_{kj} z_{ki} \right] + \sigma_0^2 \delta_{ij} \quad , \quad (87)$$

where L_k is the distance between the k_{th} and $(k+1)_{th}$ chamber plane and $z_{ki} = \sum_{m=1}^i L_m$ is the distance between the k_{th} and the i_{th} planes. $\sigma_0 = 225 \mu\text{m}$ is the intrinsic drift chamber resolution. To minimize the χ^2 function, the momentum is changed in each step. This continues until the momentum converges within 0.5%.

The momentum extracted from the toroid track fit determines the energy of the muon at the beginning of the toroid. This amount has to be added to the muon energy loss in the target calorimeter to get the total muon energy.

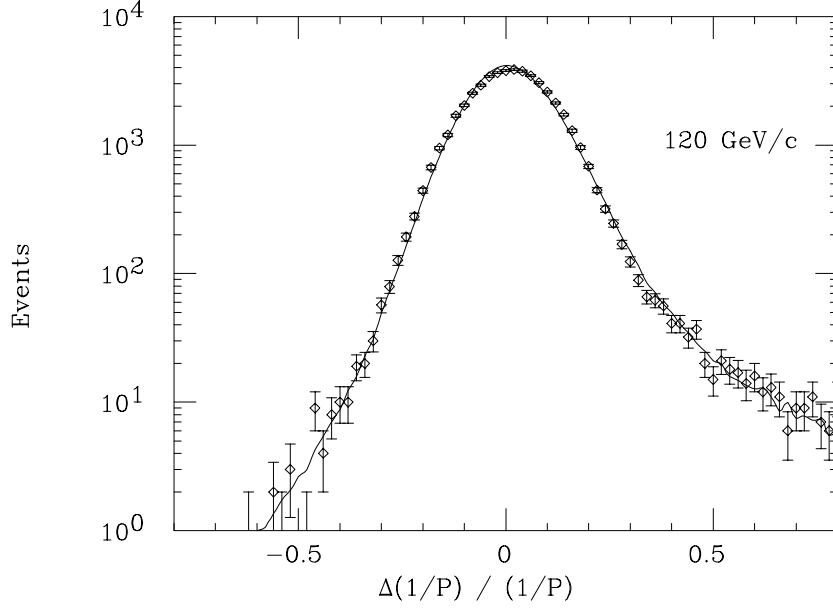


Figure 22: Experimental resolution function of the muon spectrometer for 120 GeV/c muons. The points are measurements of test beam muons, the solid line is an independent Monte Carlo prediction. The tail on the negative side is due to hard single scatters, and the tail on the positive side is due to catastrophic energy losses.

To determine the muon momentum resolution of the toroid spectrometer, test beam muons were used. The muons were momentum analyzed independently in the test beam spectrometer. Then their momenta were measured in the toroid spectrometer. The following resolution function was formed:

$$f_{res} = \frac{1/p_{toroid} - 1/p_{testbeam}}{1/p_{testbeam}} \quad , \quad (88)$$

where p_{toroid} is the muon momentum measured in the toroid spectrometer and $p_{testbeam}$ is the muon momentum measured in the test beam spectrometer.

Figure 22 shows the resolution function for 120 GeV/c test beam momentum. The shape is mostly Gaussian with a peak at zero and a width of $\sim 11\%$. The tail in the

negative side of the peak is due to MCS effects and causes the muon momentum to appear larger. The right side tail is from MCS plus muon catastrophic energy loss in the toroid spectrometer. This side of the curve causes the muon momentum to appear smaller.

4.4.3 Muon Energy Loss in Target

The muon energy loss in the target depends on the event vertex. Muons lose energy primarily through ionization, in which case, the deposited energy in each counter is about one MIP. High energy muons occasionally lose a greater amount of energy through bremsstrahlung and pair production. These are known as catastrophic energy losses. To calculate the muon energy loss in the target, first the energy loss after the hadronic shower is measured; the pulse-heights are added from counter (*SHEND-6*), the end of the hadronic shower, to the most downstream counter, counter number 1. If less than three MIP's is deposited in a counter, the amount is attributed to ionization loss and conversion factor $C_\mu = 0.158$ GeV/MIP is used. Anything more than three MIP energy deposition in a counter is attributed to catastrophic energy loss. Since the catastrophic losses are electromagnetic phenomena, they are treated as such and the conversion factor $C_e = 0.190$ GeV/MIP is used. The total muon energy loss, *ELOSS*, in the calorimeter after the hadronic shower is then:

$$ELOSS = \sum_{i=SHEND-6}^1 [\text{MIN}(3, \text{MIP}_i) \times C_\mu + \text{MAX}(0, \text{MIP}_i - 3) \times C_e] \quad . \quad (89)$$

Inside the hadronic shower, the muon energy loss cannot be observed. Instead an approximation, *RLOSS*, is made. This is based on an estimated muon energy and

angle, to account for different forms of energy loss. It is based on the parameterization of the “relativistic rise” in the muon energy loss spectrum:

$$RLOSS = \sum_{i=PLACE}^{SHEND-5} \left(0.9315 + 0.02359 \times \ln(E_i^{est}) \right) / \cos(\theta_\mu) \quad . \quad (90)$$

Here, the estimated muon energy is the sum of the E_{FF} from the toroid ¹⁰ and the estimated muon energy loss in the target:

$$E_i^{est} = E_{FF} + 0.1595 \times SHEND \quad , \quad (91)$$

where 0.1595 GeV is the average energy loss per counter. The muon energy loss is the sum of equations 89 and 90.

4.5 Reconstruction of Kinematics in the Data

All the kinematic variables are reconstructed from the hadronic energy, E_{had} , the muon momentum, P_μ , and the muon angle, θ_μ .

By conservation of energy, the neutrino energy is simply the sum of the hadronic and muon energies:

$$E_\nu = E_\mu + E_{HAD} \quad . \quad (92)$$

Other kinematic variables are reconstructed in terms of the measured quantities according to equations 12 through 19. In particular the Bjorken x is reconstructed as:

$$x = E_\mu \left(1 + \frac{E_\mu}{E_{HAD}} \right) \frac{2 \sin^2(\theta_\mu/2)}{M_N} \quad . \quad (93)$$

which is the same as equation 19 repeated here for convenience.

¹⁰FF stands for front face of the toroid.

4.6 Cuts

There are two different major types of cuts applied to the data for various CCFR analyses: the fiducial volume cuts and the kinematic cuts. The fiducial volume cuts make sure that the event is contained within the sensitive part of the detector. These cuts are common to all CCFR structure function analyses. The kinematic cuts in this analysis however are different from other structure function analyses. These cuts are much tighter here since the measurement of kinematic variables in the region of interest suffers from larger resolution errors.

4.6.1 Fiducial Volume Cuts

The fiducial volume cuts are designed to make sure the event occurs and is contained within the active part of the detector.

The cuts are the following: ¹¹

- $PLACE < 80$. This cut rejects incoming muons. Incoming muons are generated from neutrino interactions in the berm upstream of the detector. To avoid misidentifying these muons as low E_{had} charged current events, all the events that deposit more than 1/4 of a MIP energy in any of the first four counters are rejected.

- $PLACE > 20$. This cut contains the hadronic shower. The hadronic shower gets absorbed in a few counters. This is especially true for large x events since they have low hadronic energy. In order to contain the shower inside the downstream end of the detector, events that start within the last 20 counters are eliminated.

¹¹The 84 counters in the target calorimeter are counted backwards by convention. Counter 1 is the most downstream and 84 is the most upstream.

- $|V_i| < 127$ cm. V_i is the vertex position in either of the two transverse directions.

If the event vertex is too close to the edges of the detector, part of the hadronic shower might escape the detector. This cut prevents this from happening.

- $R_{FF} < 160$. R_{FF} is the muon radius at the front face of the toroid. This cut requires that the muon be inside the active region of the toroid chambers.

- Muon in Good Magnetic Field. The muon is required to stay inside the good magnetic field region in the toroid for 80% of its flight length . This assures a good muon momentum measurement.

- Fitted Muon Track. A good muon track is required in the target calorimeter and all segments of the toroid. These tracks are also required to be linked to each other to have one and only one muon track throughout the detector.

- The χ^2 of the toroid track fit is required to be less than 10 [13].

In addition to these geometric cuts, the following cuts are also applied to assure the event quality:

- Good Event Quality. This series of cuts eliminates all bad runs, requires the events to occur during the fast spill (section 3.2), and also reject events where more than one neutrino interaction occurred.

- No Dimuon Event. Dimuon events [10] are rejected by eliminating charged current events with a second track that either makes it to the toroid, or, penetrates more than 19 counters.

4.6.2 Kinematic Cuts

The kinematic cuts are engineered in this analysis to minimize the error of the reconstructed x (equation 93). The error in x is:

$$\left(\frac{\delta x}{x}\right)^2 = \left(\frac{E_{HAD} + 2E_\mu}{E_{HAD} + E_\mu}\right)^2 \left(\frac{\delta E_\mu}{E_\mu}\right)^2 + \left(\frac{E_\mu}{E_{HAD} + E_\mu}\right)^2 \left(\frac{\delta E_{HAD}}{E_{HAD}}\right)^2 + (\cot\theta/2)^2 (\delta\theta)^2 \quad (94)$$

where the three different terms come from the measurement error of muon energy, the hadronic energy, and the muon angle respectively.

The relative error in x resulting from the hadronic energy measurement can get as large as the relative error in the hadronic energy itself. Because the hadronic energy resolution (equation 75) gets worse with decreasing energy, the hadronic energy is required to be greater than 20 GeV.

The error on x from the muon energy measurement error can get twice as large as the relative error in the muon energy. This is very important in the high E_μ region since the measurement gets worse at very high muon energy. Even though this happens at near TeV energies (section 4.4.2), to avoid possible events with mismeasured momentum, an upper cut of 360 GeV is used for the muon energy.

There is also a 15 GeV lower cut on the muon energy. This cut is designed to make sure that the muon has enough energy to make it through the toroid.

In addition to these cuts on the muon energy, the muon is required to traverse the whole length of the toroid. This requirement makes sure the muon momentum is as well measured as it can be.

The muon angle measurement error tends to get very large at low θ_μ . A lower cut of 17 mrad is used to eliminate possible problem resulting from the muon angle error.

There is lower cut of $Q^2 > 50 \text{ (GeV)}^2$ on the momentum transfer to eliminate theoretical uncertainties. These are QCD “higher twist” effects [18] and fall off like M_N/Q^2 . The higher cut on Q^2 is 400 (GeV)^2 . There are very few events beyond this value.

Table 4 shows a summary of different cuts and their rejection percentages. The total rejection percentage is the percentage of events that do not pass the cut over all events. The exclusive rejection percentage is the percentage of events that pass all other cuts but fail that particular cut over all events. There were about two million charged current triggers in the E770 data sample. About ninety thousand of these events pass all the cuts. There are about 4500 events with $x > 0.6$ in this sample. Figure 23 shows the data x distribution between 0.6 and 1.2 after all the fiducial and kinematic cuts.

Cut	All Data		$0.6 < x < 1.2$	
	Total Rej.	Exclusive Rej.	Total Rej.	Exclusive Rej.
gate	2.73%	0.00591%	0.0401%	0.000%
in-time muon	1.67%	0.059%	0.302%	0.0131%
$20 < \text{PLACE} < 80$	33.2%	0.574%	23.2%	1.59%
vertex box	16.3%	0.396%	16.0%	1.56%
80% Steel	2.74%	0.134%	3.69%	0.319%
muon through toroid	43.8%	2.07%	39.2%	6.40%
$\chi^2 < 10$	18.9%	0.000106%	5.25%	0.00128%
$\theta_\mu > 17$ mrad	18.2%	0.000497%	22.9%	0.000%
$E_\mu > 15$ GeV	6.93%	0.0201%	0.450%	0.00422%
$E_\mu < 360$ GeV	5.33%	0.0325%	2.31%	0.300%
$E_{had} > 20$ GeV	39.5%	0.00363%	74.8%	0.000%
$E_{had} < 360$ GeV	0.288%	0.0817%	0.0169%	0.000%
$Q^2 > 50$ (GeV) ²	87.7%	20.0%	85.1%	6.22%

Table 4: Cuts and their rejections.

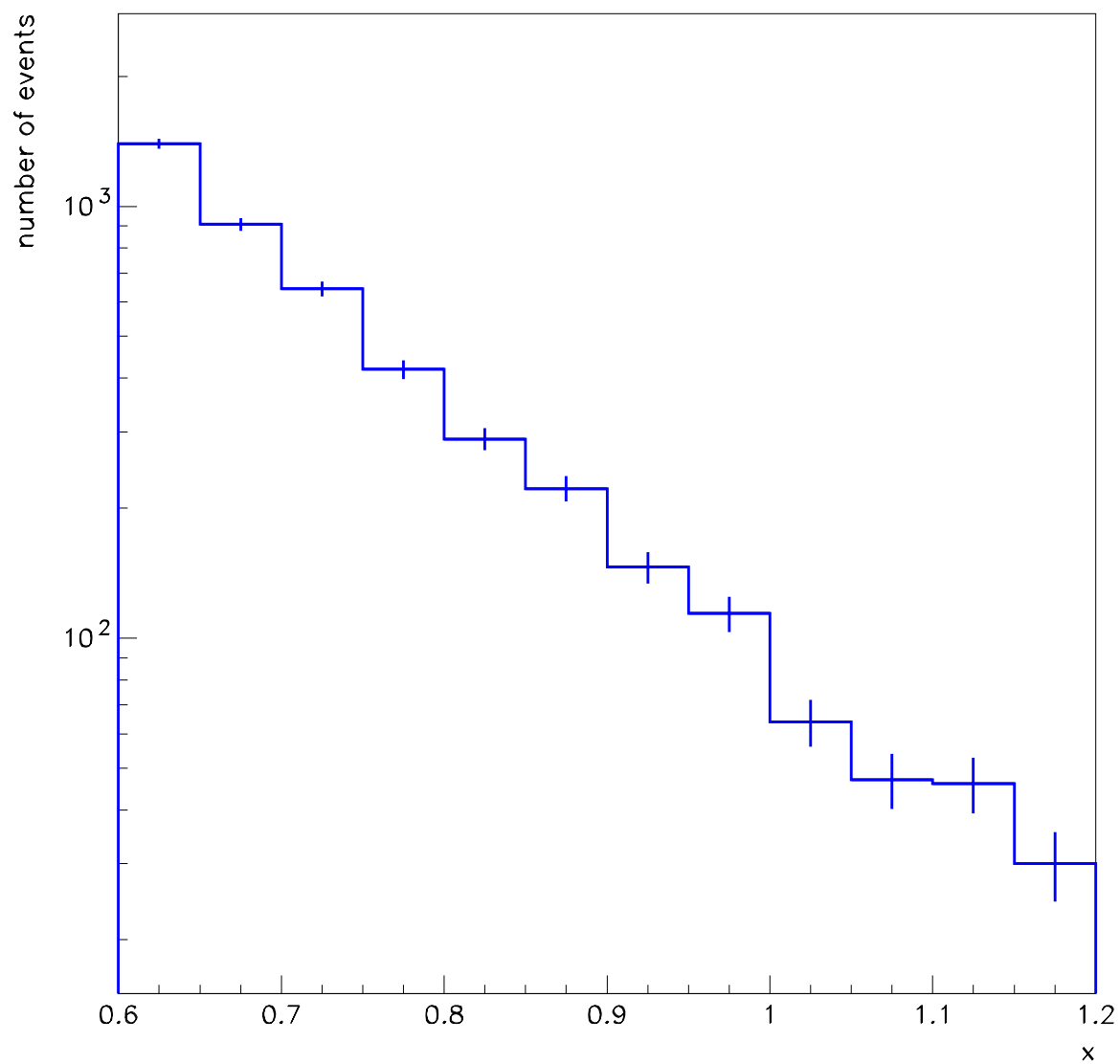


Figure 23: The x_{meas} distribution after all cuts.

5 Monte Carlo Simulation

The goal of an experimental physics measurement is to extract actual physical quantities. In this analysis these quantities are the nuclear structure functions. However, all measurements are subject to detector effects that alter true physical quantities. As a result, the distributions of observed physical quantities are different from the true ones.

To decipher true quantities from the observed ones, the detector resolution and acceptance effects have to be taken into account. Since it is impossible to find out everything about the evolution of the individual events in the detector, one has to account for these effects on a statistical basis. This is the main idea behind “Monte Carlo” simulations. A Monte Carlo simulation is basically a modeling of the physics of the interactions plus replication of the detector effects. These together are supposed to reproduce the data events on a statistical basis. The physics model generates event kinematics that correspond to the pure physics of interest. The detector simulation alters the generated event kinematics to produce observed quantities that mimic the real world.

Once one achieves a good detector simulation, one can either

1. try different models by comparing the observed data and Monte Carlo distributions (hypothesis testing) or,
2. find the best values of parameters within a model that make the data and Monte

Carlo observed quantities agree (parameter fitting).

Both types of analyses for different physical models are done in this thesis.

5.1 Event Generation

The event generation in the Monte Carlo of this analysis is done in the following steps:

- The neutrino energy E_ν is randomly generated from an input flux file extracted from the data.¹²

- The scaling variables x and y are generated with a flat distribution.

- Event kinematics are calculated from x , y , and E_ν .

- The event is thrown against the physics model cross section, as a function of event kinematic quantities.

- The event vertex coordinates in the detector are generated from a vertex flux distribution taken from the data events.¹³

- The longitudinal coordinate of the event is generated randomly with a flat distribution along the detector.

- The azimuthal angle of the outgoing muon is generated randomly.

The following three physical models are used for event generation:

¹²The flux extraction is based on low E_{had} (low y) charged current event rates in the data (section 3.2.1, figure 10). For low E_{had} (low y) events, the cross section does not vary much with E_{had} (y). Therefore these events are used for flux parameterization which is based on event rates, as a function of the total neutrino energy. This method is called “relative flux” extraction. It determines the relative flux between two energy bins, $\Phi(E_i)/\Phi(E_j)$ and the relative flux between neutrinos and anti-neutrinos. Due to its relative nature it is a systematically robust method. The absolute flux normalization is not needed in this analysis. The detailed flux extraction method is given in [13].

¹³The data sample used for the vertex generation has looser cuts on the event vertex. This allows the Monte Carlo simulation to mimic the same fiducial volume cut as in the data (section 4.6).

1. The Buras-Gaemers model [30].

This model is based on a parameterization of the iron structure functions up to $x = 0.8$ done by Buras and Gaemers (CERN). This parameterization is based on the best fit to CCFR data in the lower x kinematic region. Since it is parameterized for iron, it contains nuclear effects in the lower x region. However as $x \rightarrow 1$, it forces the structure functions to vanish. This is based on the assumption that the scattering occurs off isolated stationary nucleons. As such, it does not account for nuclear effects at high x (section 2.5).

2. The Buras-Gaemers model plus Fermi motion simulation.

Fermi motion (section 2.5.1) is simulated according to the reference [3] and [4]. Two different models are simulated. The first is Fermi gas motion where the nucleons are given a momentum according to the Fermi momentum distribution in the iron nucleus. The second model has a momentum distribution attributed to the formation of “quasi-deuterons” in the nucleus in addition to the Fermi gas motion. The latter generates higher momentum components inside the nucleus.

3. Exponentially falling F_2 at large x .

Certain theoretical models based on Few Nucleon Correlations or Multi-quark Clusters (Bags) predict an exponentially falling behavior for F_2 at large x (section 2.5). The model used in this analysis is based on a phenomenological parameterization of F_2 , used by the BCDMS collaboration [1].

5.2 Resolution Smearing Simulation

To account for detector measurement and acceptance errors in the data, the Monte Carlo should mimic the same type of errors. Generated kinematic variables are therefore smeared by a proper form to replicate the detector measurement and acceptance errors. The error on some of the kinematic variables is more drastic than others. For example the position resolution of the muon track is about 250 μm and therefore its error is not very large. On the other hand, resolution errors of the muon and hadronic energies are much more important.

The most prominent source of error in the large x data sample is the error on the muon momentum p_μ . Large x events have large muon momenta since x increases with E_μ almost quadratically (equation 19). The muon momentum resolution function, $f_{res} = \frac{1/p_{toroid} - 1/p_{testbeam}}{1/p_{testbeam}}$ (derived from the analysis of the muon test beam), was shown in figure 22. The Monte Carlo uses the exact same numerical values with bin-to-bin interpolation. For each event, a random value from this distribution is used to smear the generated muon momentum. Figure 24 shows a comparison between these random values of the smearing function for a large number of events and the function itself. The two forms are identical within errors.

The hadronic energy mismeasurement is another important source of error in the large x data. The hadronic energy resolution is given by equation 75. Unlike muon energy resolution, this resolution deteriorates at low hadronic energy. This is important since large x events have small hadronic energy (equation 19). Equation

75, which is extracted from test beam data, was used to smear the generated hadronic energy in the Monte Carlo. The comparison between the calorimeter hadronic energy and test beam measured momentum for 25 and 200 GeV/c test beam momenta was shown in figure 20. The resolution is understood better at higher energies and the Poisson fits match the data better for high E_{had} . The lowest hadronic energy in this analysis is 20 GeV (section 4.6).

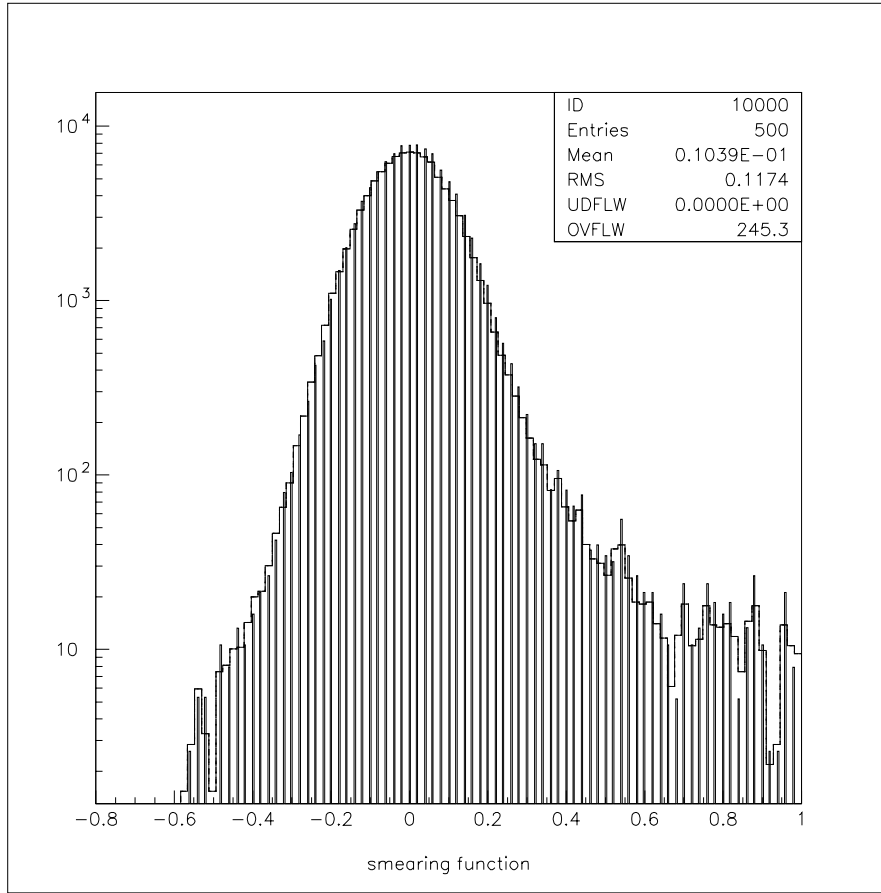


Figure 24: Comparison between The Monte Carlo modeling of the muon energy resolution function, $f_{res} = \frac{1/p_{toroid} - 1/p_{testbeam}}{1/p_{testbeam}}$ (the bar charts) and the Monte Carlo reconstructed resolution function (solid histogram).

Figures 27 to 31 (at the end of this chapter) show plots of different observed

quantities in the Monte Carlo and the data for the $x > 0.6$ data sample after all cuts.

5.3 Radiative Correction

The complete one-loop electroweak radiative correction for neutrino DIS has been calculated by D. Bardin *et. al.* [27]. This calculation is used in other CCFR analyses of the structure functions ([5], [8], and [13]). The major radiative effect in the charged current neutrino DIS, especially for the large x sample, is the muon bremsstrahlung¹⁴. This process is shown in figure 25. This radiative effect causes mismeasurements in the muon and hadronic energies. The energy of the emitted photon is absorbed inside the hadronic shower. Therefore this portion of energy is reduced from the actual muon energy and added to the actual hadron energy. According to equation 19 both these effects cause the observed x to appear less than its actual value. As such, the radiative correction is important in the high x region. However the size of the effect on the cross section is about 10% at the most and is not as crucial as other effects like resolution smearing.

The corrections are not done on an event by event basis in the Monte Carlo. Instead tables of corrections are prepared in advance. The correction for each event in a bin of E , x , and y are linearly interpolated to the kinematic coordinates of the event. Figure 26 shows the radiative correction for 200 GeV neutrino charged current events. The plot shows the percentage change of the cross section due to radiative

¹⁴In a muon DIS process the outgoing muon is drastically accelerated perpendicular to the direction of motion. For neutrino charged current DIS this is more drastic since the muon is actually created and the charge is accelerated from rest. This causes muon bremsstrahlung to dominate other radiative effects in neutrino charged current DIS events.

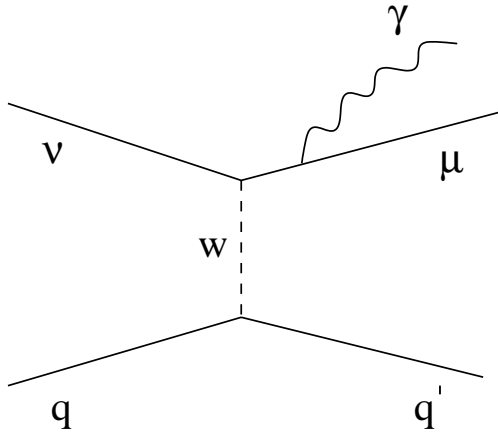


Figure 25: The muon bremsstrahlung radiative effect in charged current neutrino DIS. The radiated energy is absorbed inside the hadronic shower and causes a reduction in the observed muon energy and an increase in the observed hadronic energy.

corrections. It is plotted as a function of y for some different x bins.

Since the Monte Carlo accommodates multi-quark clusters and nucleon-nucleon correlations, it is assumed that events with large x might be caused by scattering off of a dinucleon or a 6-quark cluster, a unit of mass $2M_N$, where M_N is the mass of the nucleon. All events generated with $x > 1$ fall into this category. For events with $0.7 < x < 1.0$, a comparison with generated events in the model that is based on stationary nucleons and no nuclear effect, determines what fraction of events generated in each bin comes from $2M$ clusters or dinucleons. For the events that come from such a unit x is replaced by $x/2$ in the radiative correction formalism. One could envision

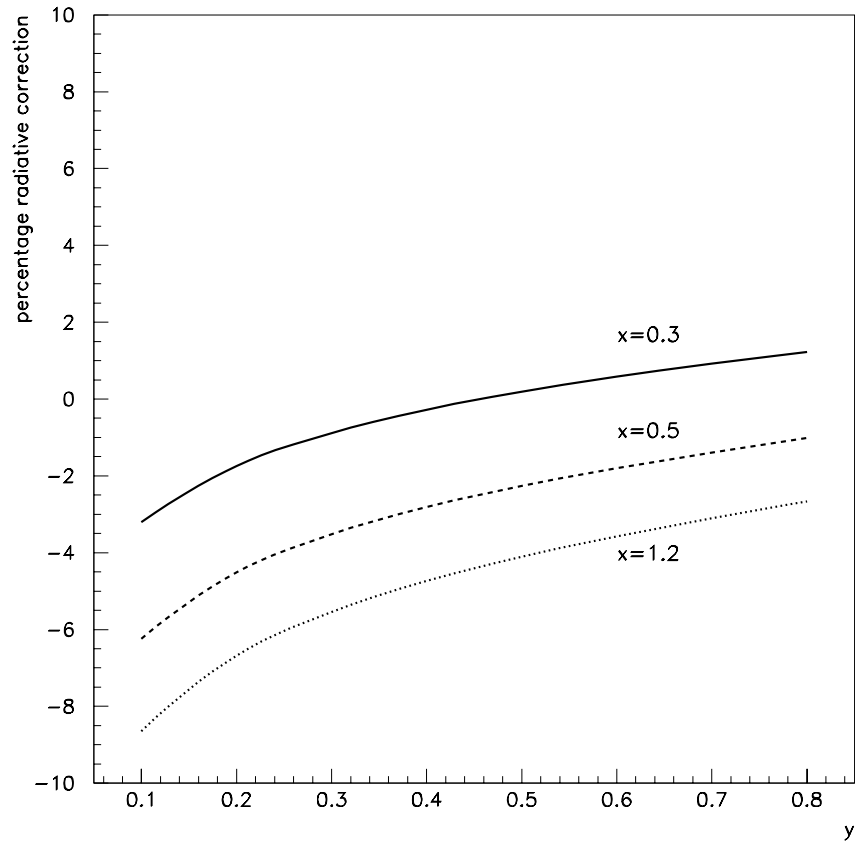


Figure 26: The percentage of the radiative correction as a function of y for different x bins, for 200 GeV neutrino charged current events. The radiative correction modifies the cross section by the percentage shown.

other models for the large x radiative corrections. A study of different models and a comparison between one-loop and leading-logarithm corrections shows that the radiative corrections of different models and schemes could vary by up to 2% only.

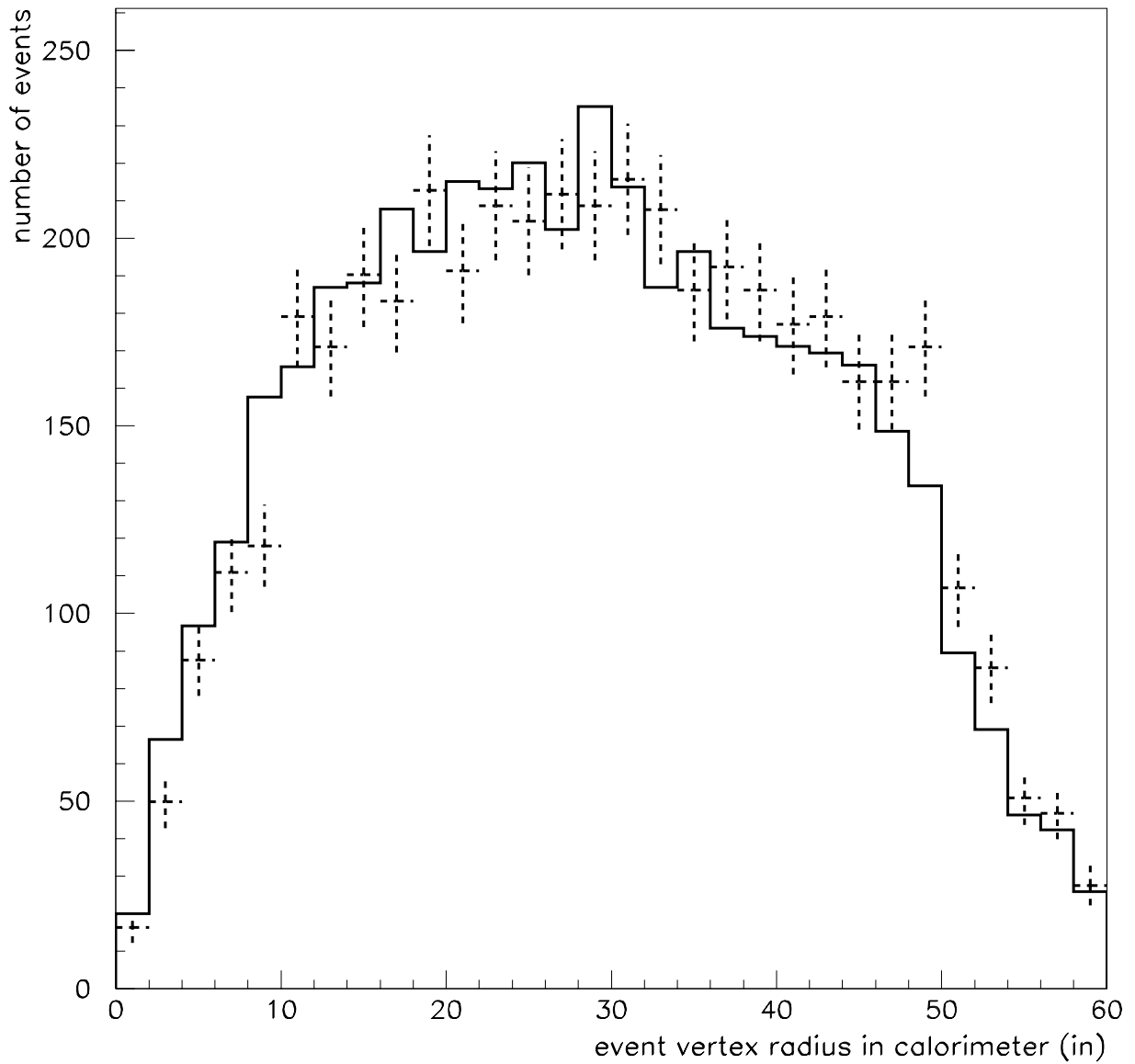


Figure 27: Event vertex radius in the data (solid histogram) and the Monte Carlo (discrete error bars). The horizontal axis is the vertex radius in inches.

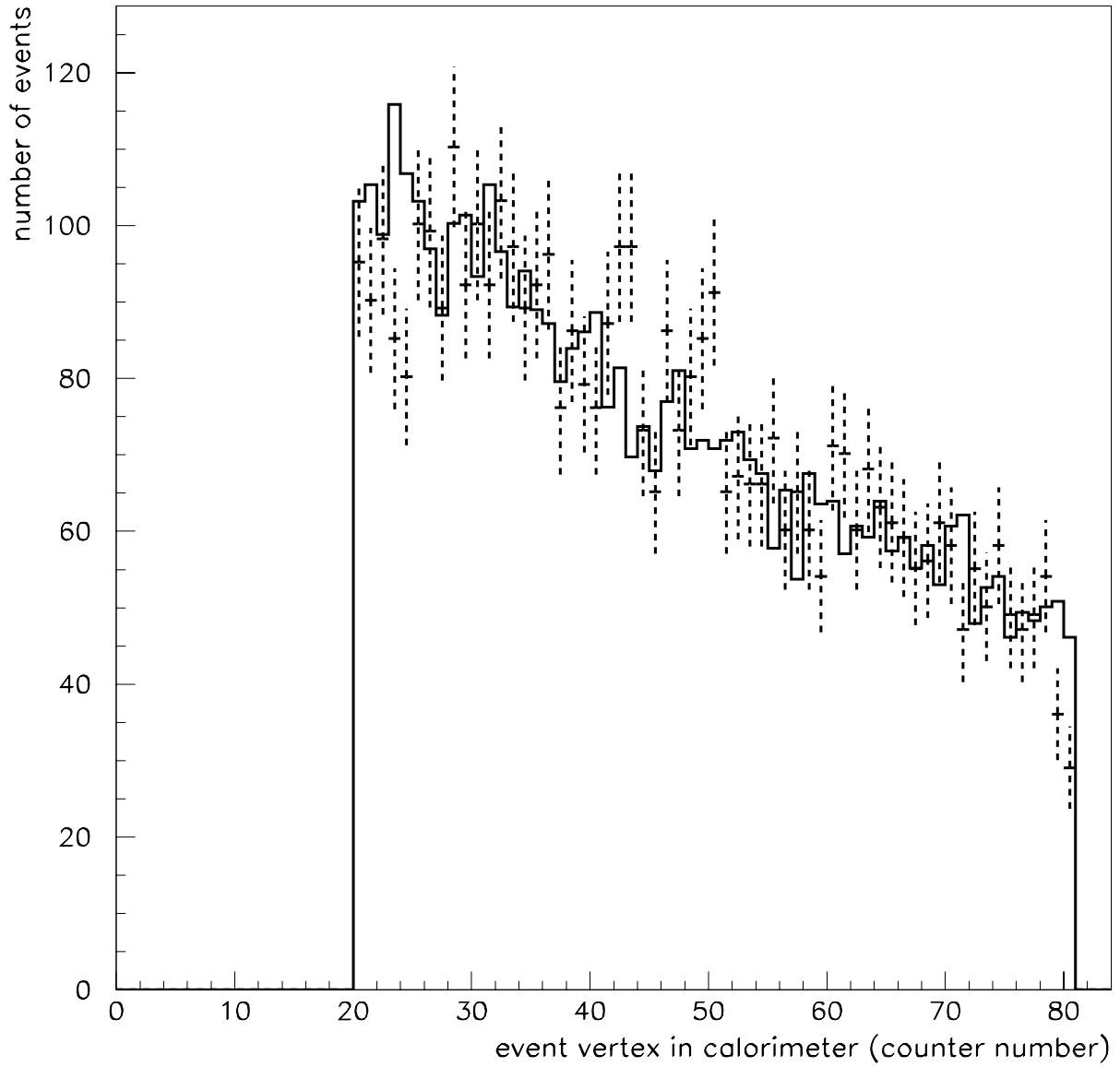


Figure 28: Event vertex longitudinal coordinate in the data (error bars) and the Monte Carlo (solid histogram). Counter 1 is the most downstream. The fiducial volume cuts eliminate 4 most upstream and 20 most downstream counters (section 4.6).

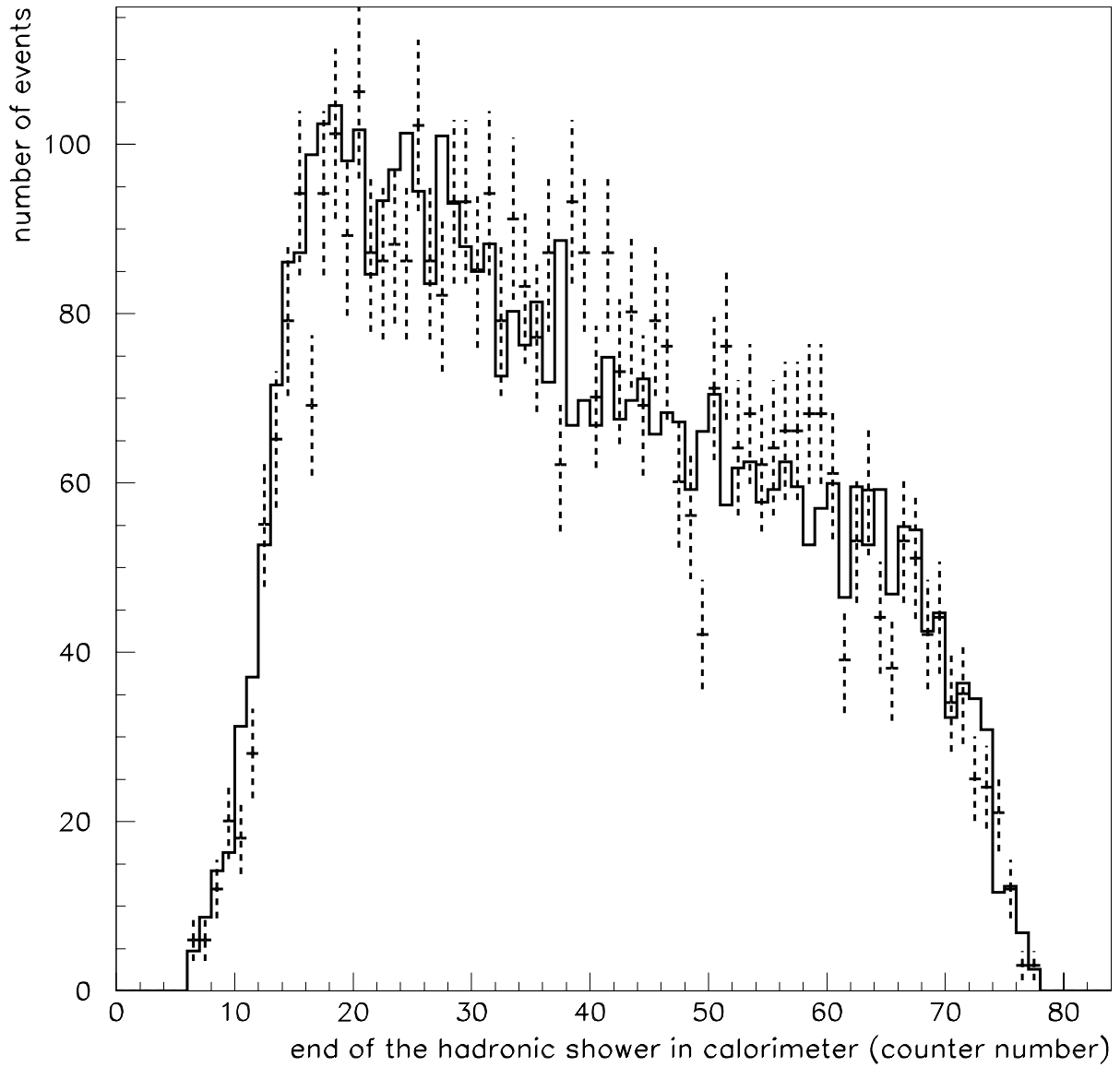


Figure 29: End of the hadronic shower in the data (error bars) and the Monte Carlo (solid histogram). Counter 1 is the most downstream. There is no shower passed counter 6 and the hadronic shower is completely contained in the target.

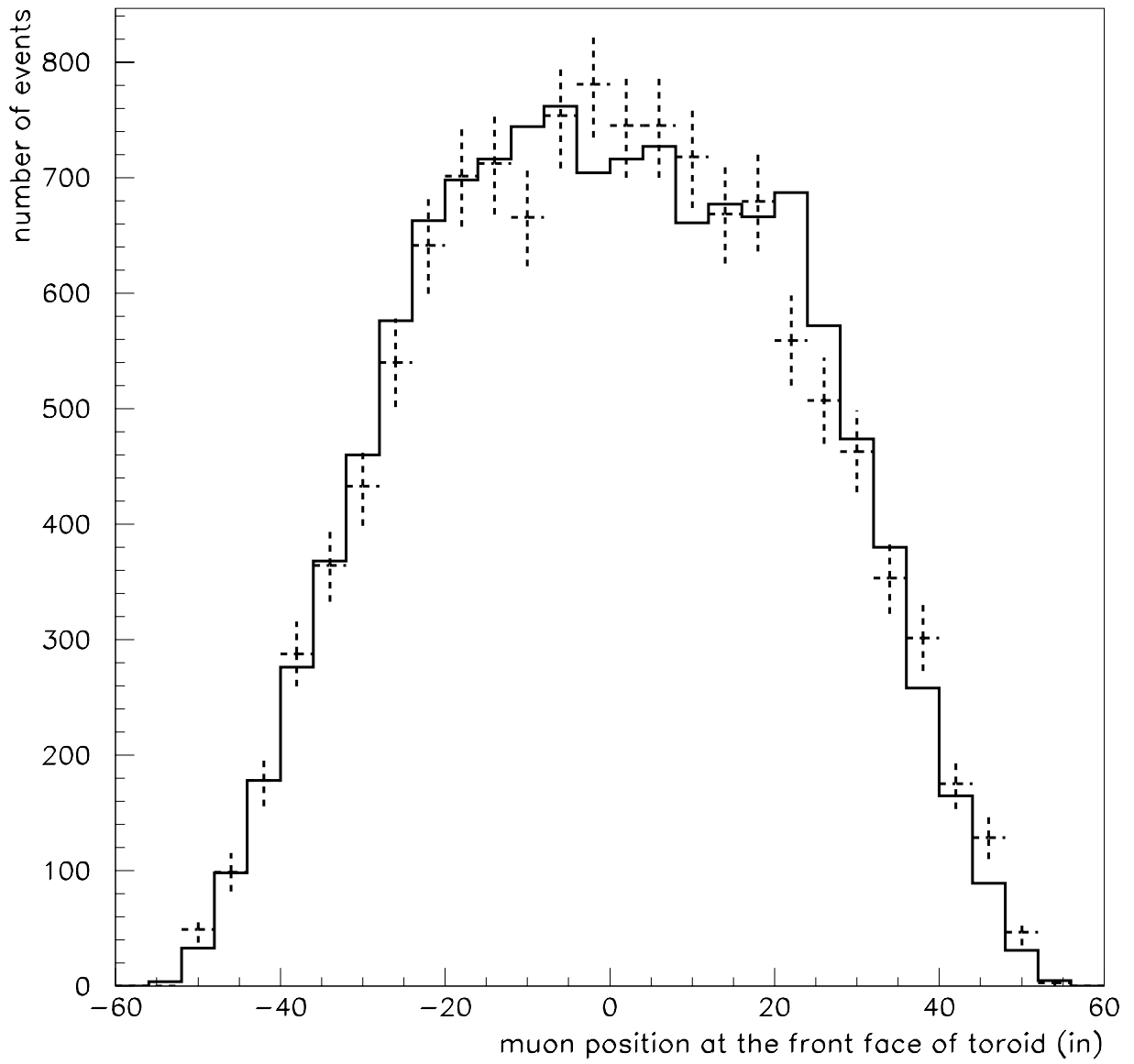


Figure 30: Muon position at front face of the toroid in the data (error bars) and the Monte Carlo (solid histogram).

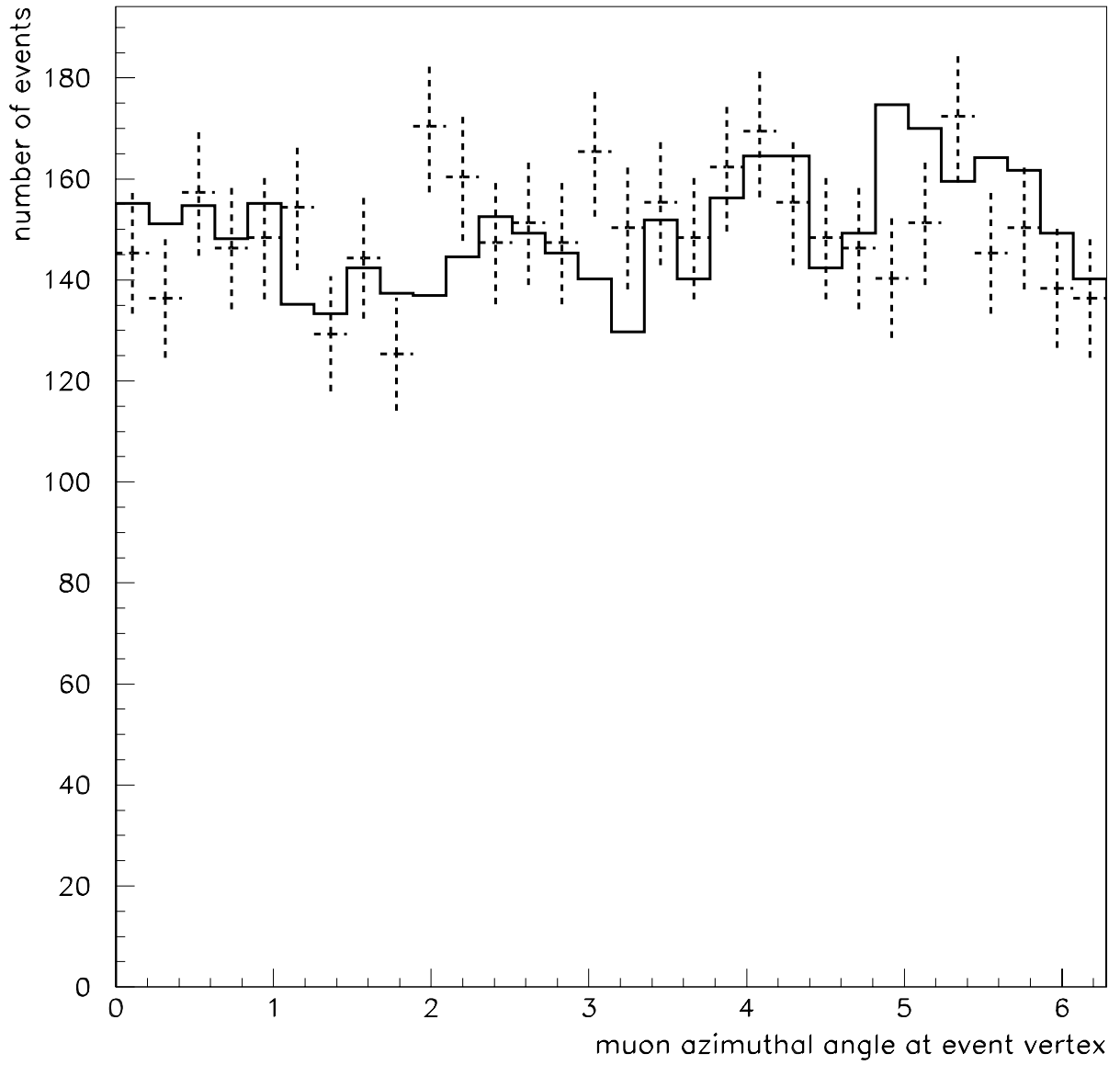


Figure 31: Muon track azimuthal angle at the event vertex in the data (error bars) and the Monte Carlo (solid histogram).

6 Results

6.1 Data-Monte Carlo Comparison

Three different models have been compared to the CCFR data. The Monte Carlo described in previous section was used to generate events for each of these models. All the cuts explained in section 4.6 are applied to both the data and the Monte Carlo events.

6.1.1 Comparison With the Buras-Gaemers Model

The first model is based on the Buras-Gaemers parameterization of the structure functions (section 5.1). The model's generated x_g distribution is shown in figure 32. The model's structure functions vanish as x_g approaches 1. As such the x_g distribution vanishes near $x_g = 1.0$ (notice the logarithmic scale). In particular there are no events generated with $x_g > 1.0$.

The reconstructed x distribution includes the effects of measurement errors. These errors do cause the tail of the reconstructed x distribution to expand beyond $x = 1.0$. This is illustrated in figure 33. Because of the steeply falling x distribution in the high x region, more events have migrated into a given bin from lower bins than from higher ones.

The resulting reconstructed x distribution is shown in figure 34. As established in previous CCFR analyses [13], there is good agreement in the $x < 0.8$ region. Beyond that however, there is a surplus of events in the data.

The Buras-Gaemers model deficit at large x is definitive; one cannot achieve an

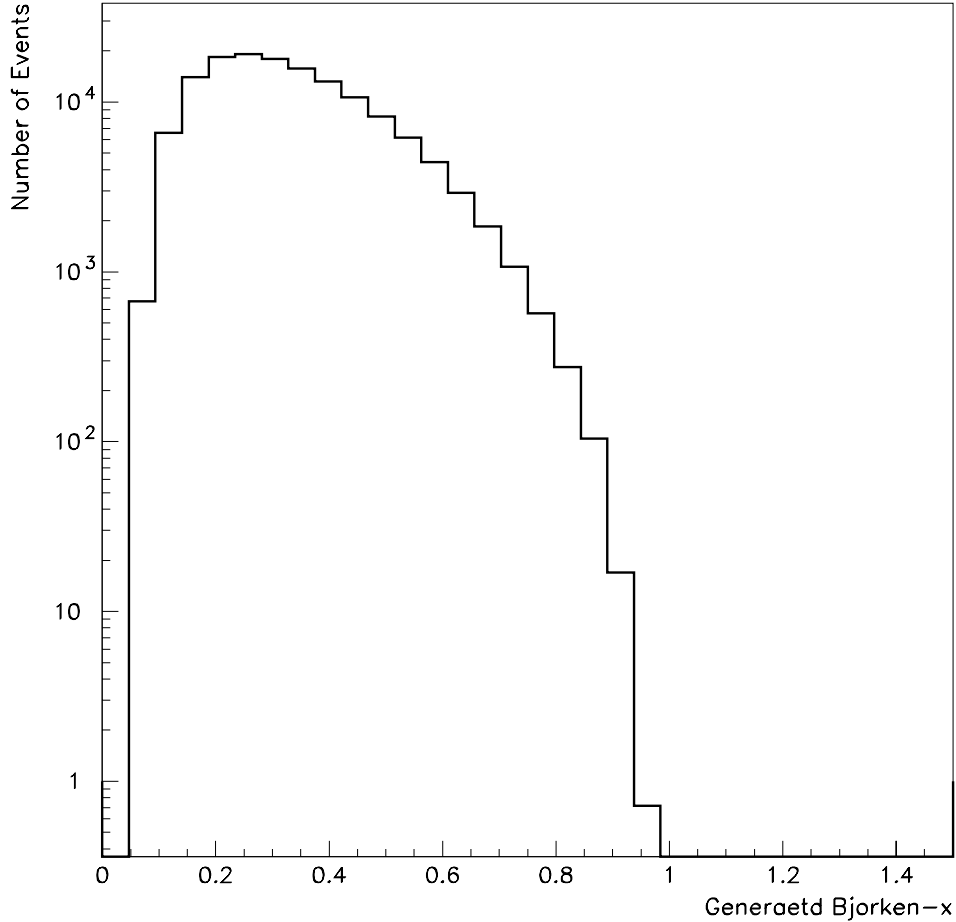


Figure 32: The generated x_g distribution in the the Buras-Gaemers model. This model forces the x_g distribution to go to zero at $x_g = 1.0$.

agreement between the data and a Monte Carlo with the assumption that the neutrinos scatter off free nucleons at rest in the laboratory frame. The Buras-Gaemers parameterization of the structure functions has been done for iron target and as such, carries some information about nuclear effects at lower x . However it does not accommodate any of the nuclear effects which affect the higher x kinematic region. As has been mentioned in previous CCFR structure function analyses ([8] and [13]), one cannot measure F_2 in the high x region with this model. This is because the analysis

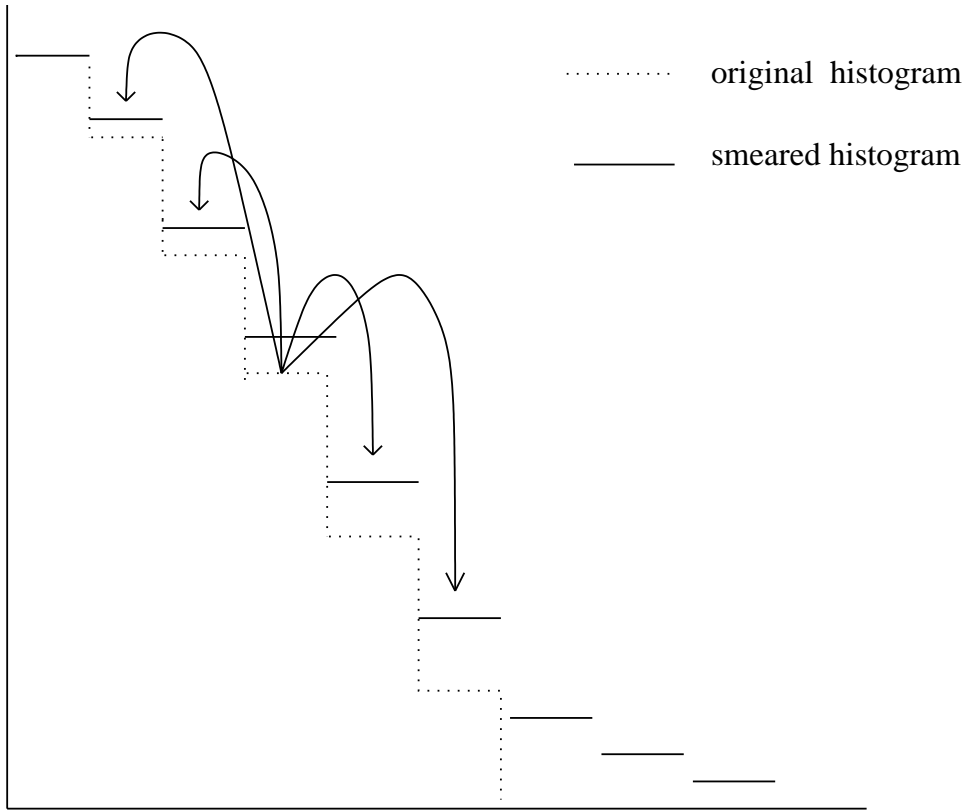


Figure 33: The effect of smearing on a steeply falling histogram. The original histogram is shown with dotted lines. More events migrate from more populous bins to less populous bins than vice versa. The resulting histogram is shown with solid lines.

depends on the comparison of data and Monte Carlo. A Monte Carlo, based on a model that does not contain high x event, cannot be used for this purpose.

6.1.2 Comparison with Buras-Gaemers Model Plus Fermi Motion

The next step is to see if the addition of Fermi Motion to the Buras-Gaemers model improves the agreement. The two different models explained in section 2.5.1 are used to generate nucleon momentum relative to the center of mass of the nucleus. Figure 35 shows how the addition of Fermi gas motion to the Buras-Gaemers mode alters the generated x_g distribution. The tail of the altered distribution reaches beyond

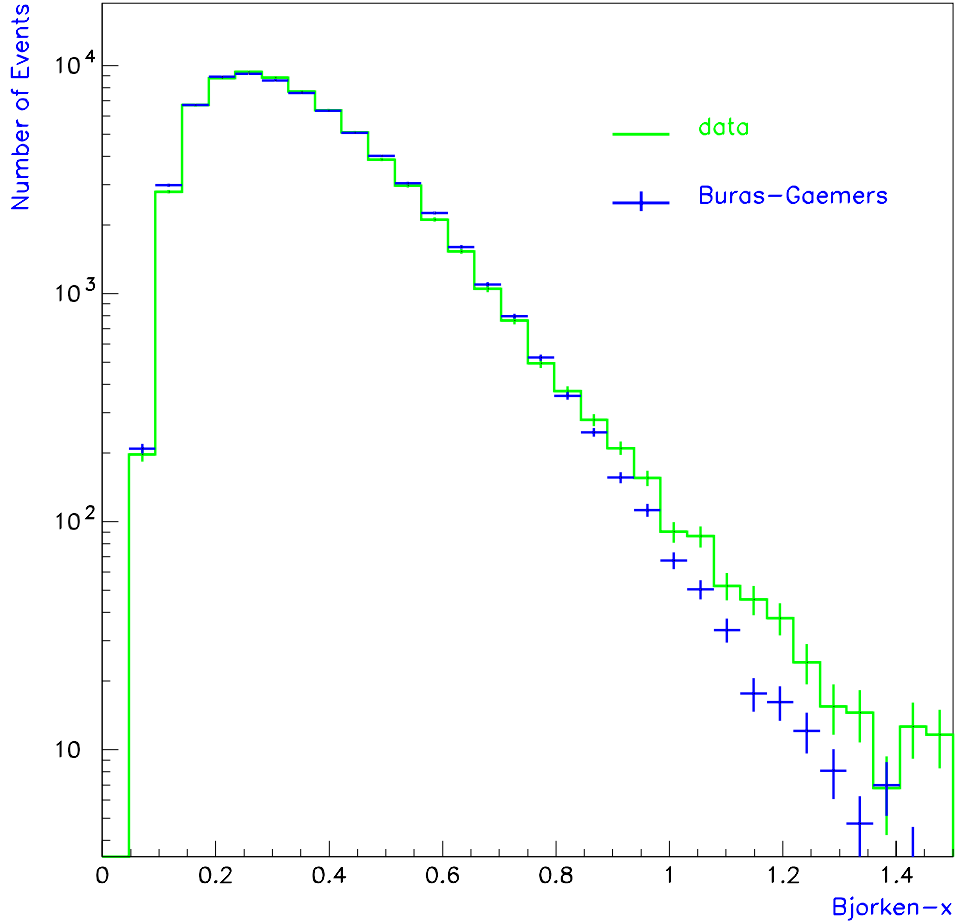


Figure 34: The observed x distribution in the data (solid histogram) and the Buras-Gaemers model (error bars).

$$x_g = 1.0$$

Figure 36 shows a comparison between the observed x distribution in the data and this model. This addition alters the Monte Carlo reconstructed x distribution ever so slightly from the Buras-Gaemers model. The addition of the nucleon Fermi gas momentum does not account for the model's deficit in the high x region.

In the second nuclear model quasi-deuteron states are added on top of the regular Fermi gas motion. Figure 37 shows the resulting generated x_g distribution compared

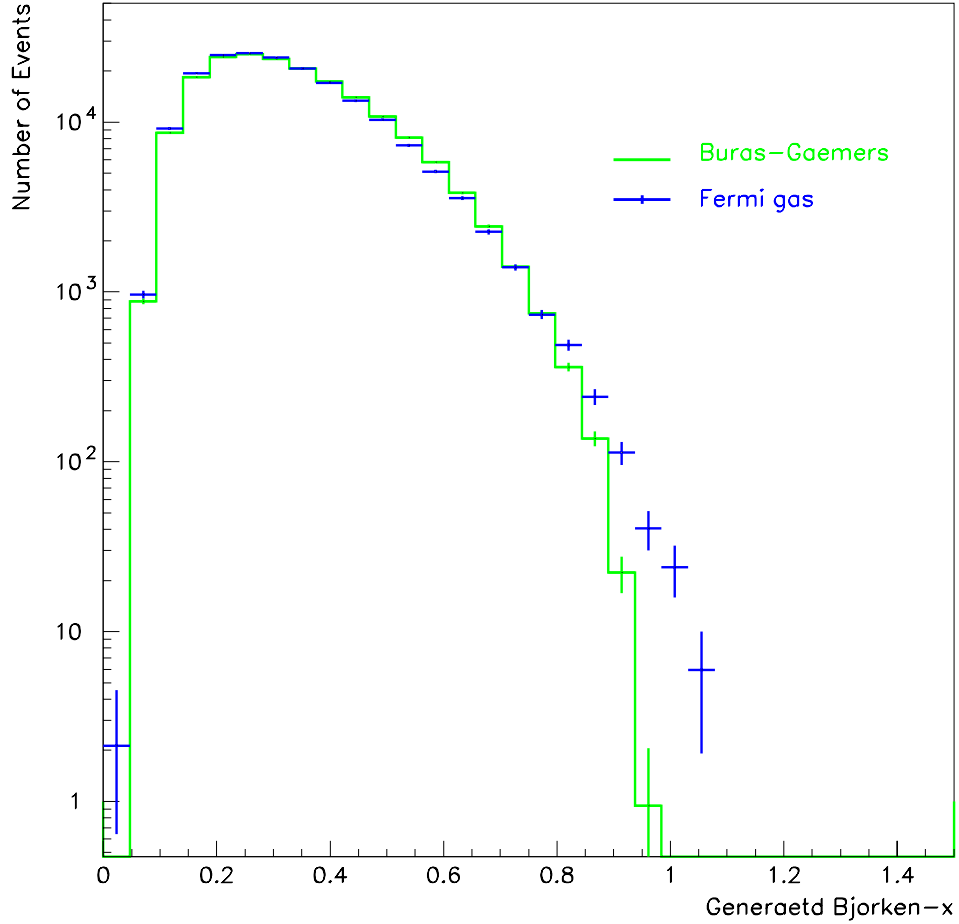


Figure 35: The generated x_g distribution in Buras-Gaemers with Fermi gas motion of the nucleons (discrete bars) and without Fermi motion (solid histogram).

with the Buras-Gaemers model. The addition of quasi-deuteron states generates higher momentum components. This causes the tail of the x_g distribution to expand further. The resulting reconstructed x distribution is shown in figure 38 in contrast to the data. The addition of the quasi-deuteron states causes better agreement between the data and the Monte Carlo up to $x = 1.0$. Beyond this region there is still some surplus of the data over the Monte Carlo.

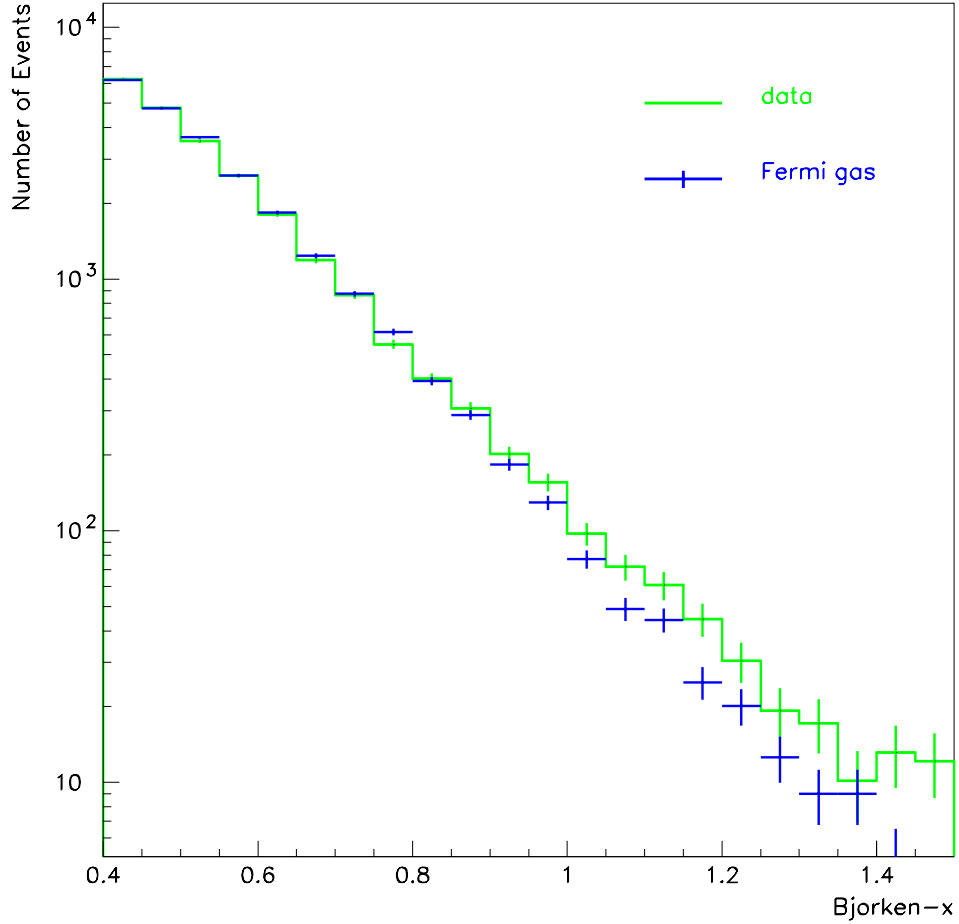


Figure 36: The observed x distribution in the data (solid histogram) and the Buras-Gaemers model with added nucleon Fermi gas distribution (error bars).

6.1.3 Comparison with Exponentially Falling F_2 Models

The structure function F_2 has been predicted to fall exponentially for the large x kinematic region by some theoretical models. These models are based on multi-quark clusters (bags) and few-nucleon correlations (sections 2.5.3 and 2.5.2). In this analysis

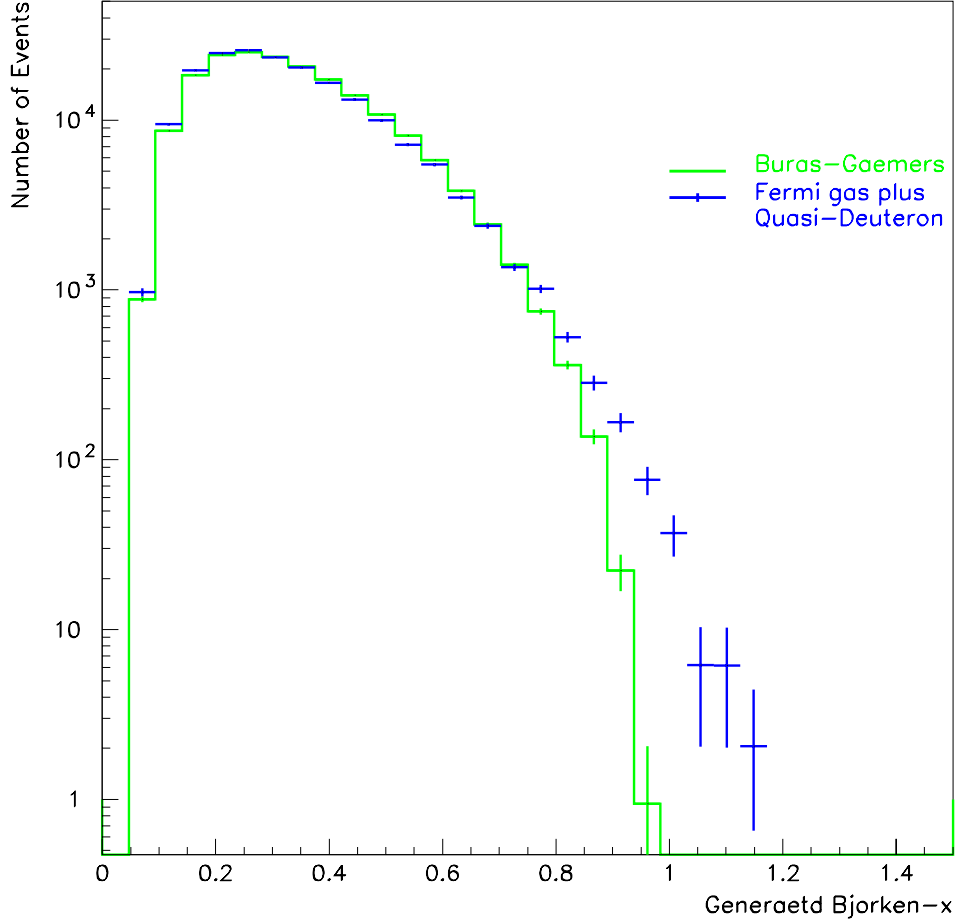


Figure 37: The generated x_g distribution in the Buras-Gaemers model with (discrete bars) and without (solid histogram) Fermi gas motion plus quasi-deuterons.

we use the following parameterization of F_2 in our Monte Carlo to fit the data:

$$\begin{aligned}
 \mathbf{F}_2(\mathbf{x}, \mathbf{Q}^2) = & \\
 & F_2^f(x, Q^2) = (1-x)^a (b + cx + dx^2 + ex^3) (Q^2)^{f+gx}, \quad x < 0.75; \\
 & F_2^f(x = 0.75, Q^2) \cdot \exp[-s(x - 0.75)], \quad x > 0.75; \quad (95)
 \end{aligned}$$

where

$$a = 2.5693 \quad ;$$

$$b = 0.2739 \quad , \quad c = 3.0437 \quad , \quad d = -5.5172 \quad , \quad e = 2.5790 \quad ;$$

$$f = -0.0303 \quad , \quad g = -0.2185 \quad .$$

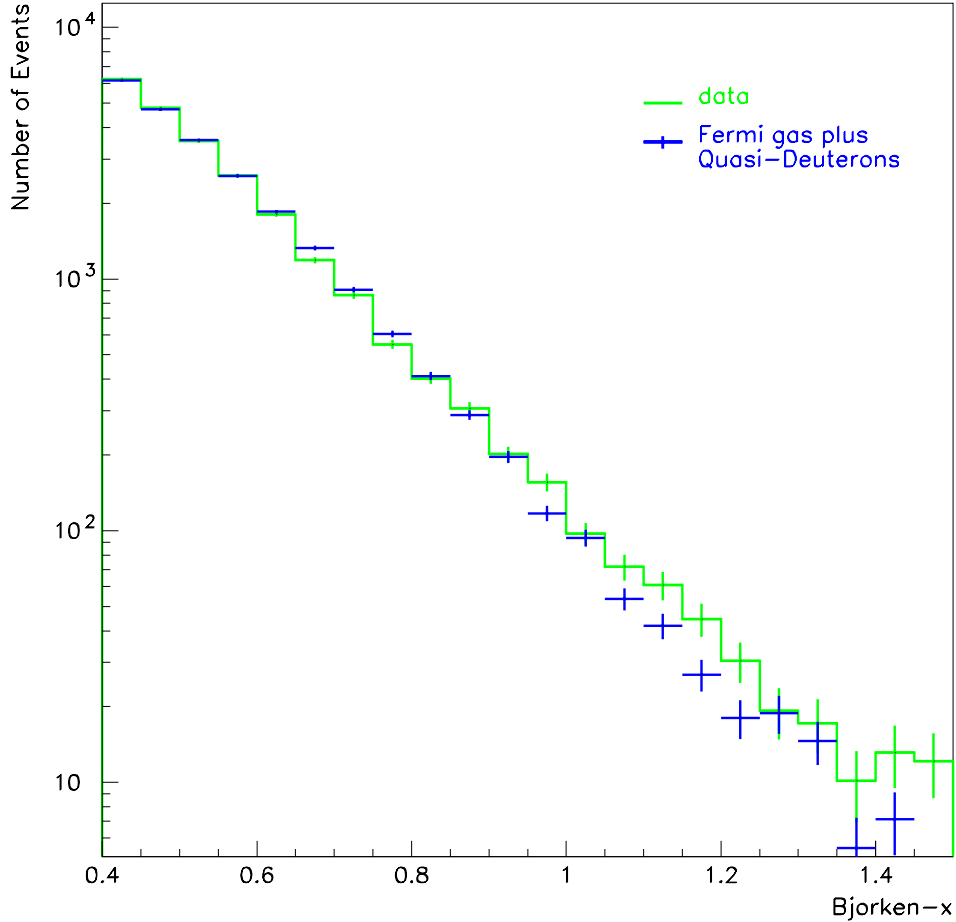


Figure 38: The observed x distribution in the data (solid histogram) and the Buras-Gaemers model with added nucleon Fermi gas distribution plus quasi-deuteron states (error bars).

This phenomenological model for F_2 is used by the BCDMS collaboration [1]. For the region $x < 0.75$, the parameterization consists of a polynomial in x and an extra factor which represents the scaling violation. This factor is a slowly falling function of Q^2 which depends on x . For $x > 0.75$, F_2 is the value of the same function at $x = 0.75$ multiplied by an exponentially falling function. This parameterization fits the CCFR data to within 5% in the $x < 0.75$ region.

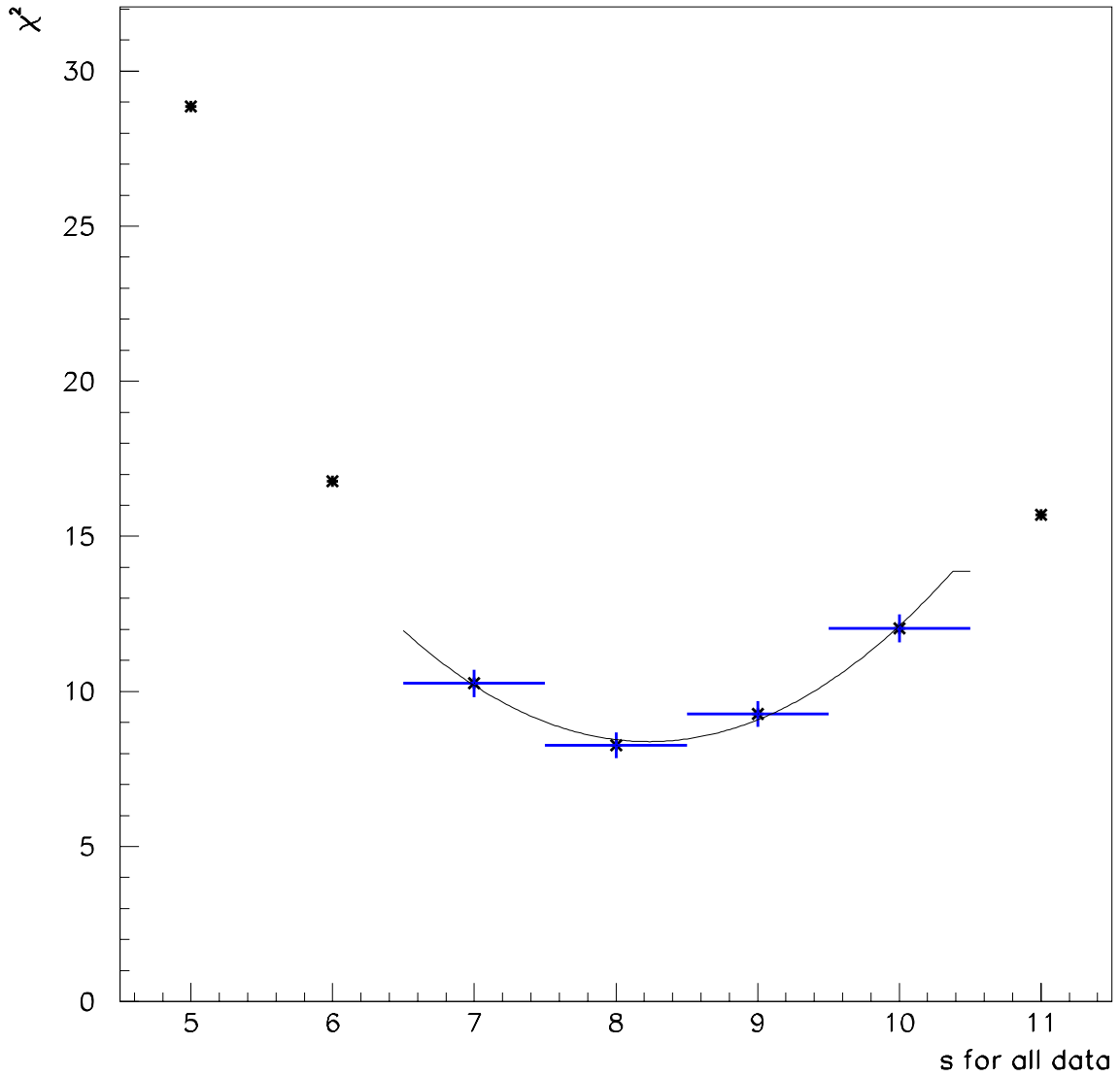


Figure 39: The χ^2 of the Monte Carlo fit to the data x distribution as a function of s , the exponent coefficient of the exponentially falling F_2 .

Values of $0 < x_g < 2$ are generated in the Monte Carlo and the observed x distribution is compared with the data. For the $x > 0.6$ region, the χ^2 of these Monte Carlo fits with different s values to the data are formed. This is done by reweighting the cross section by $\exp(-s(x - 0.75))$ corresponding to the desired s value. Figure 39 shows the resulting χ^2 as a function of s . The four best s in figure 39 are fitted to a quadratic function to determine s . The value of s that minimizes χ^2 is:

$$s = 8.3 \pm 0.7 \quad . \quad (96)$$

The error on s has been determined by one unit variations from the minimum χ^2 .

Figure 40 show the comparison between the data and the Monte Carlo for this s value. The distributions of other kinematic variables (figures 41, 42, 43, 44, and 45) show good agreements between data and the exponentially falling F_2 model.

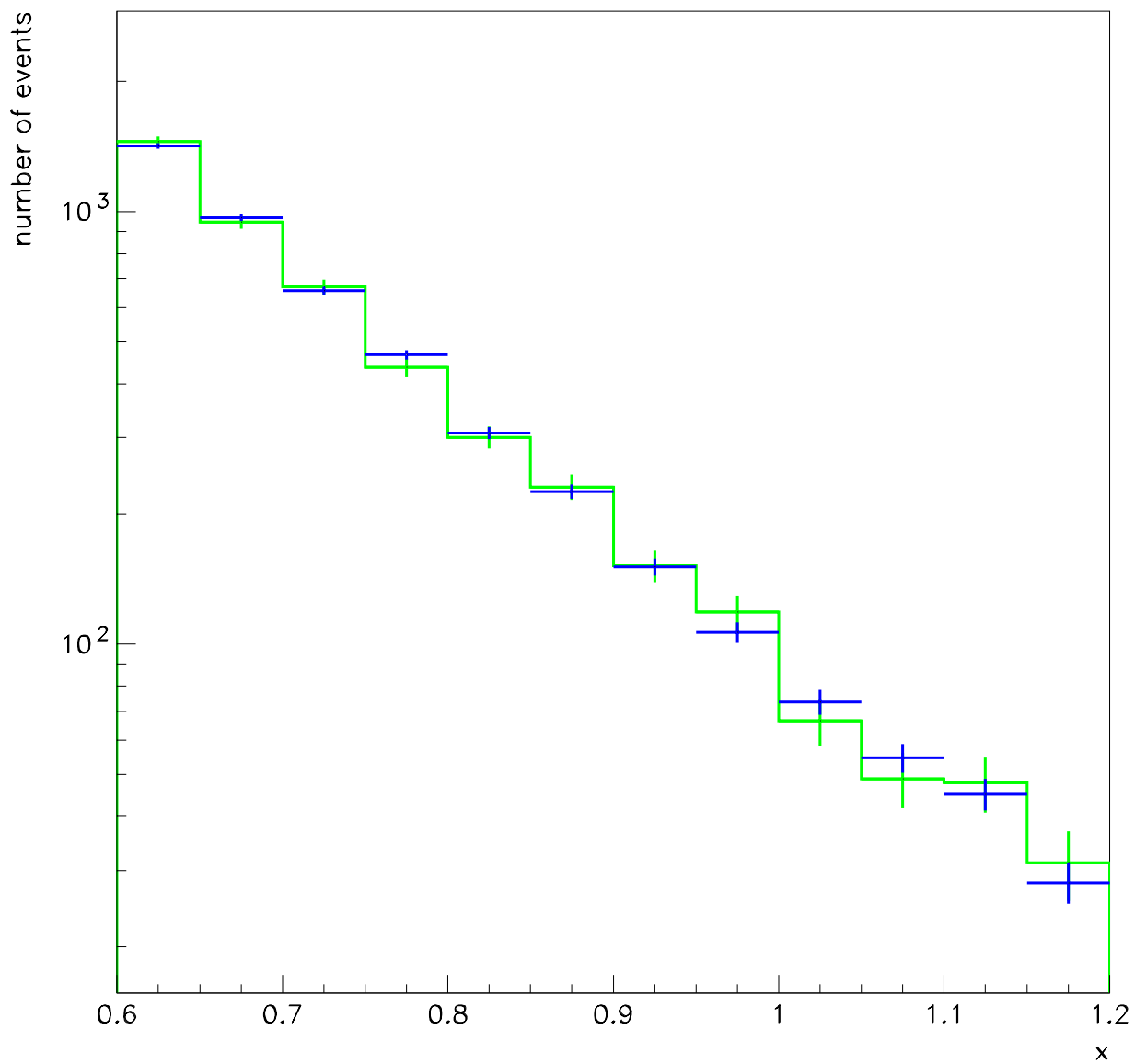


Figure 40: The x distribution in the data (solid histogram) and the exponentially falling F_2 model with input value of $s = 8$.

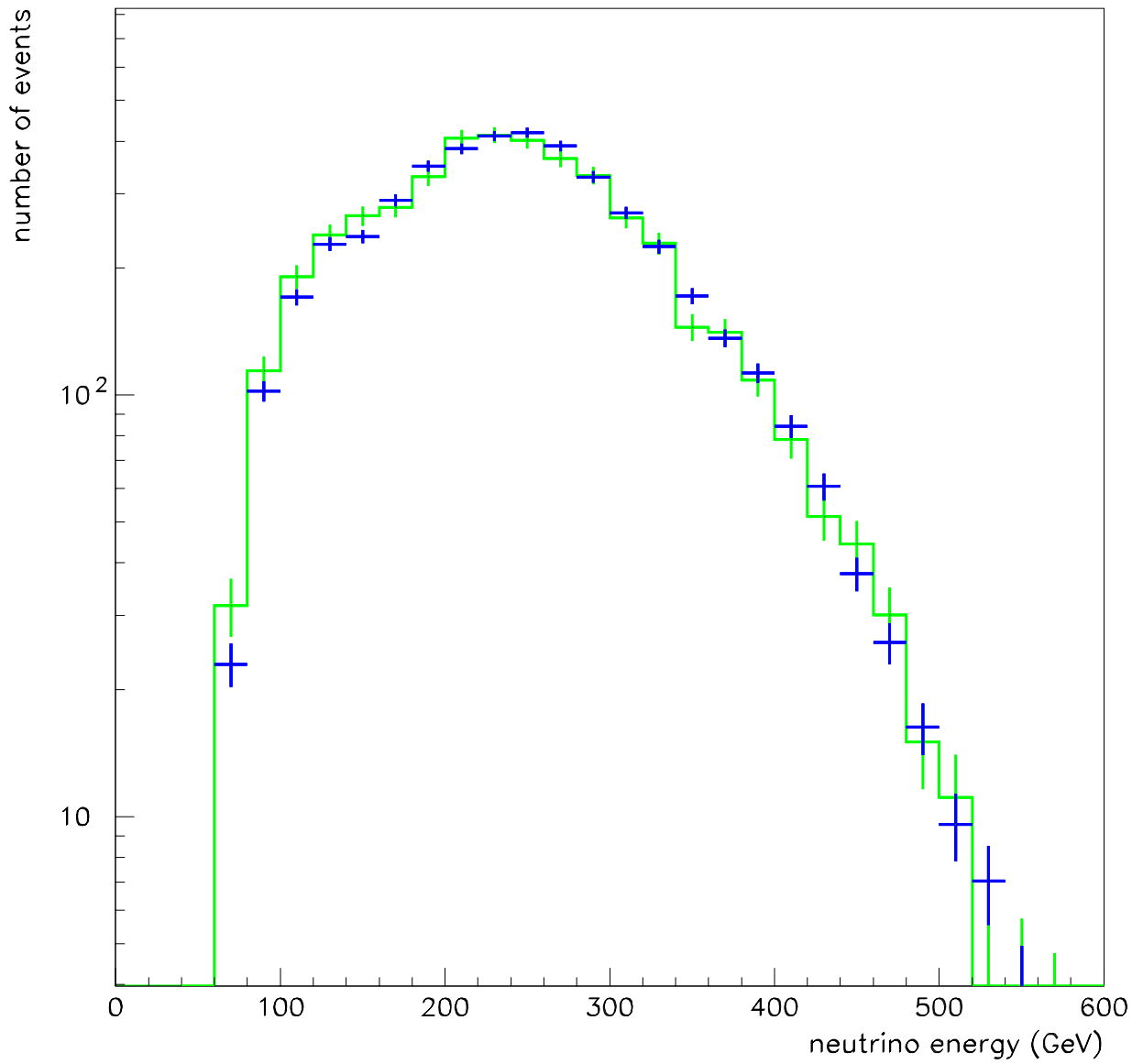


Figure 41: Neutrino energy in the data (solid histogram) and the exponentially falling F_2 model (discrete error bars) for the $x > 0.6$ region.

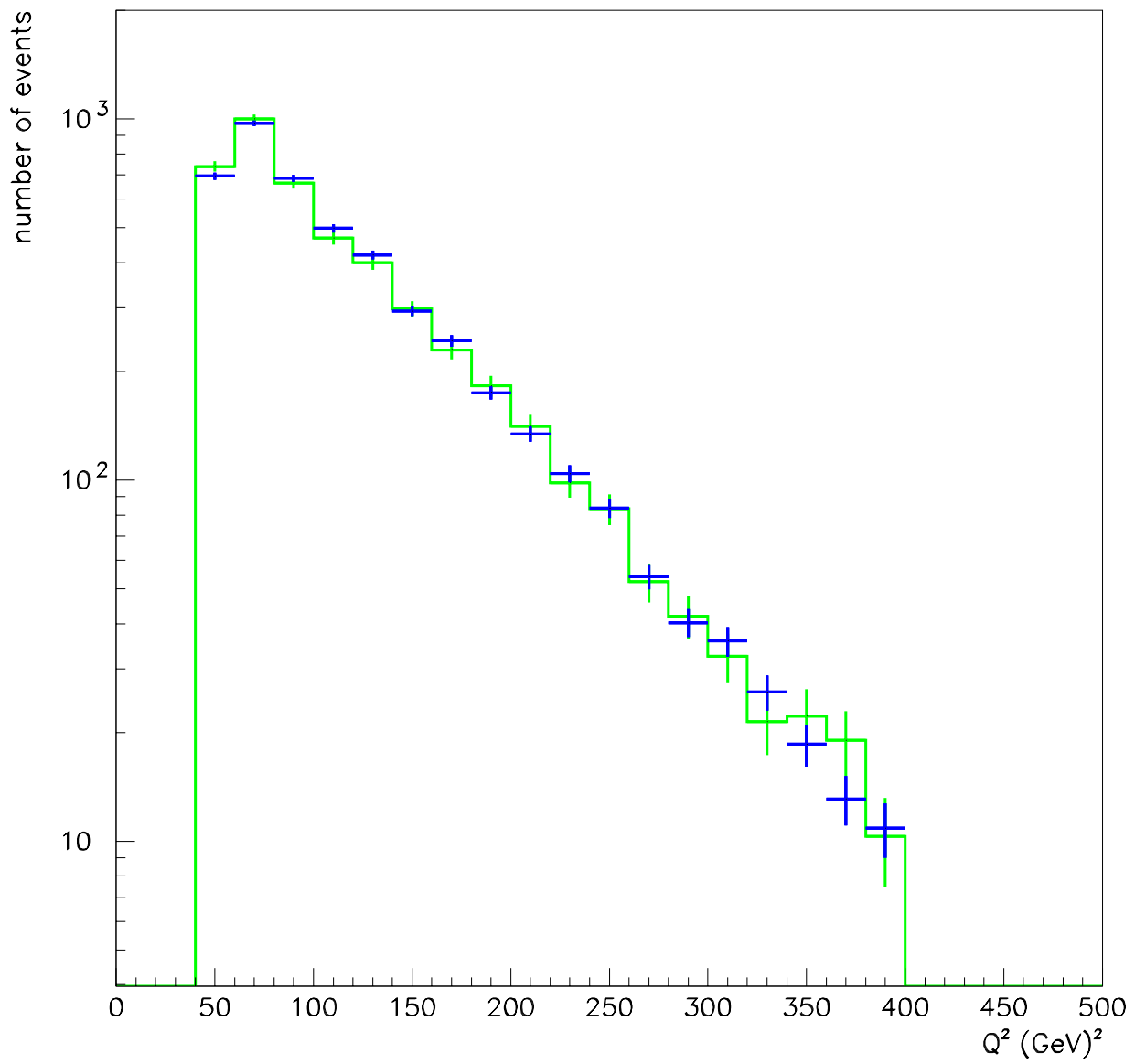


Figure 42: Q^2 in the data (solid histogram) and the exponentially falling F_2 model (discrete error bars) for the $x > 0.6$ region.

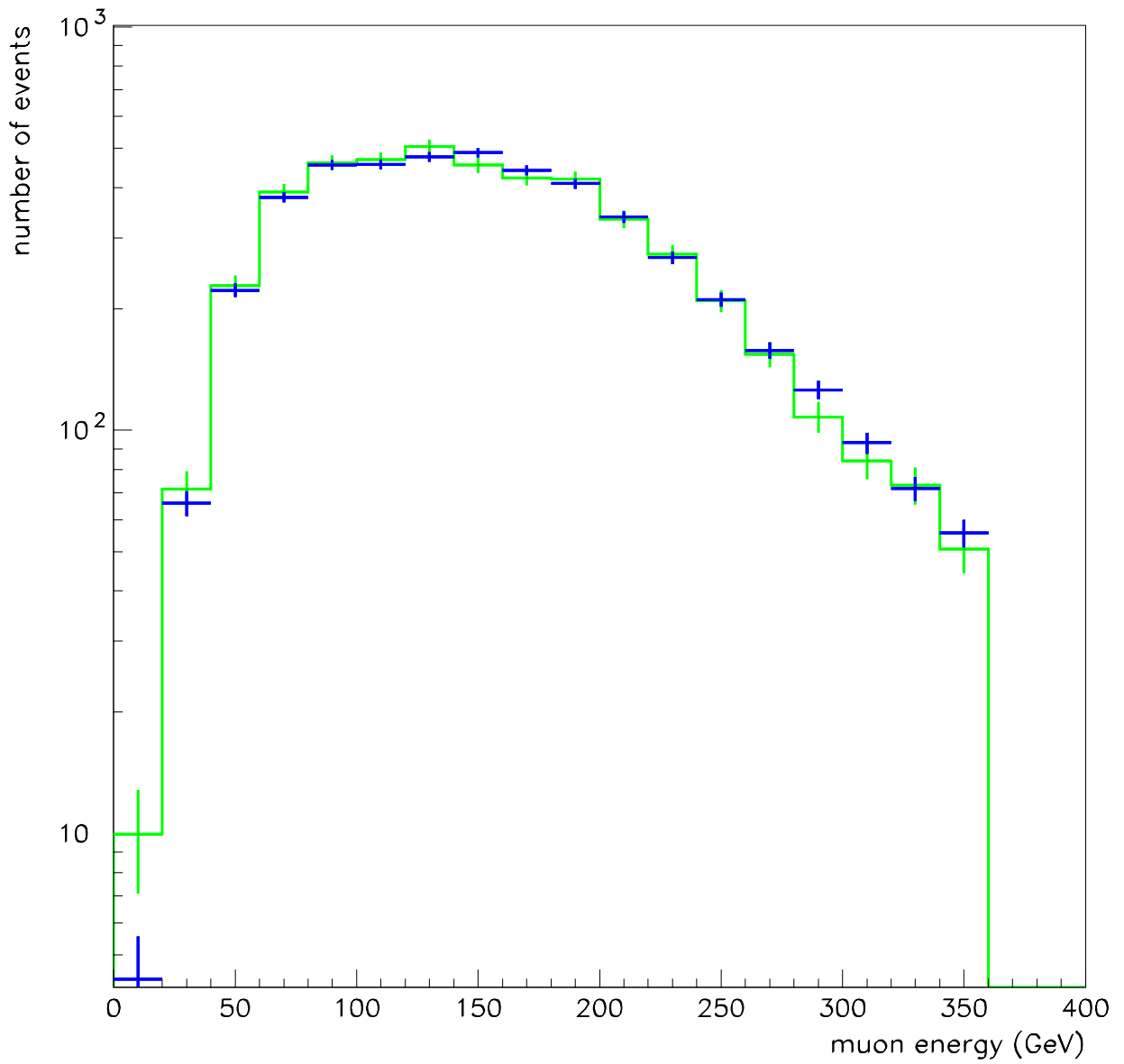


Figure 43: Muon energy in the data (solid histogram) and the exponentially falling F_2 model (discrete error bars) for the $x > 0.6$ region.

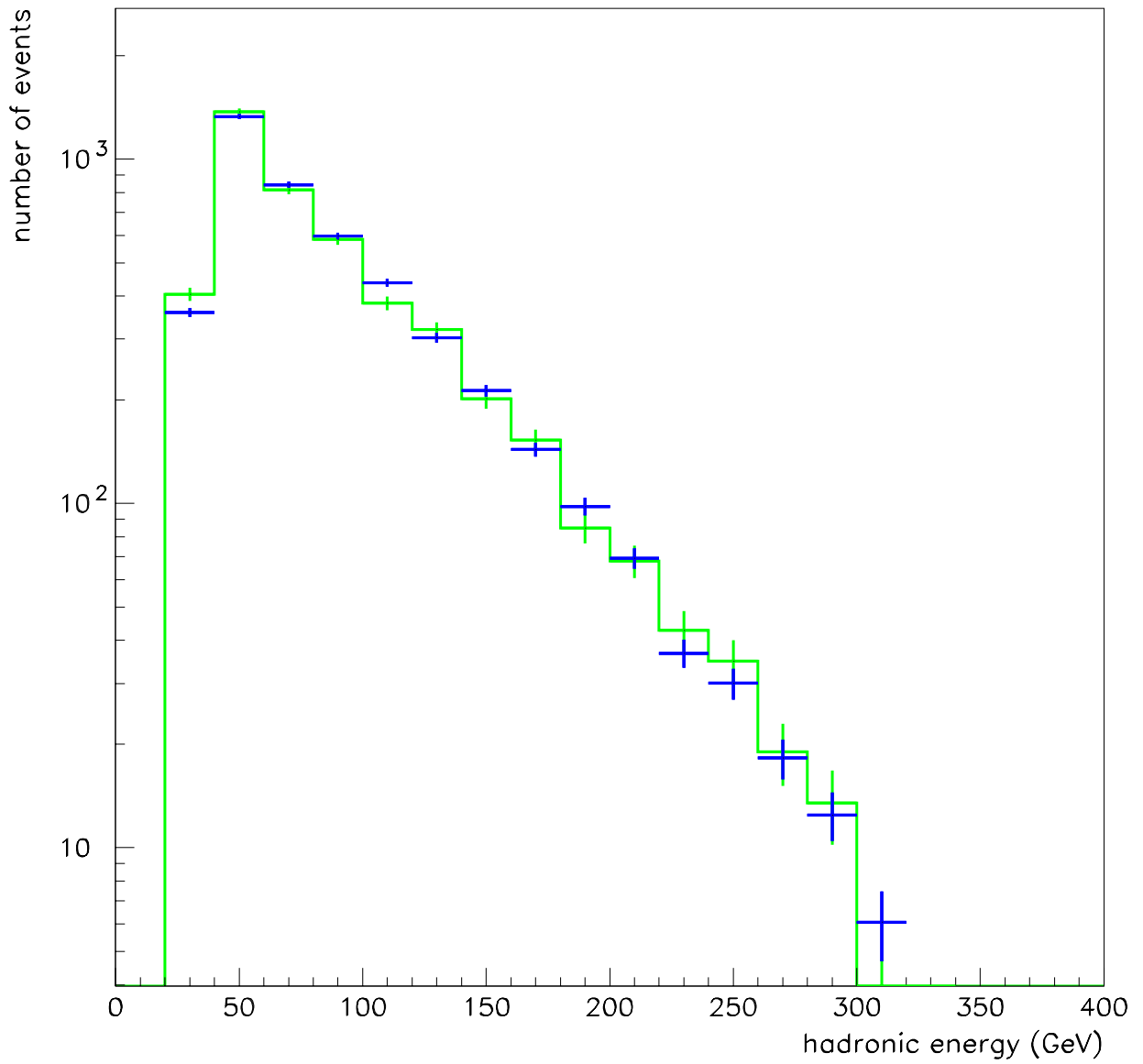


Figure 44: Hadronic energy in the data (solid histogram) and the exponentially falling F_2 model (discrete error bars) for the $x > 0.6$ region.

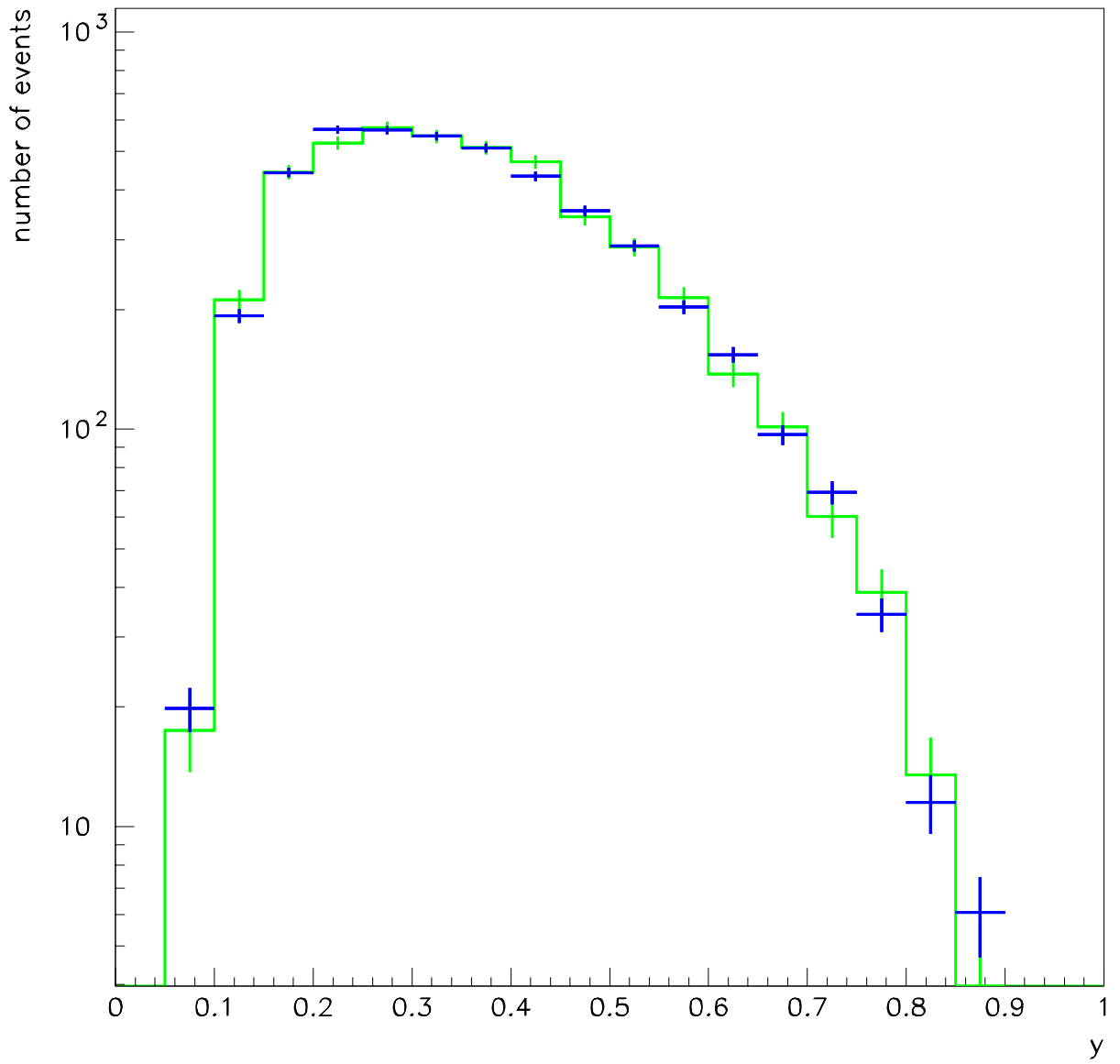


Figure 45: y distribution in the data (solid histogram) and the exponentially falling F_2 model (discrete error bars) for the $x > 0.6$ region.

6.1.4 Dependence of s on Q^2

The value of $s = 8.3 \pm 0.7$ was determined from x distributions integrated over all values of Q^2 above 50 (GeV)^2 . To understand the behavior of s as a function of Q^2 , the kinematic region of $Q^2 > 50 \text{ (GeV)}^2$ has been divided into two different regions.¹⁵ The same technique explained in the previous section is applied to find the value of s for each Q^2 region. There is less data in each individual region and one cannot do as precise a measurement as for the whole data sample. Table 5 shows the results for the determination of s with separate fits to the χ^2 distributions in each region. Figures 46 and 47 show the results of χ^2 fits for the two kinematic regions in table

Q^2 region	s
$50 < Q^2 < 100$	7.4 ± 0.9
$100 < Q^2 < 400$	8.7 ± 1.1

Table 5: The behavior of s with increasing Q^2 .

5. Even though the behavior of s seems to be consistent with no variations with Q^2 , one can see a slight increase of s with increasing Q^2 . This behavior is consistent with the logarithmic fall-off of F_2 with Q^2 at lower x region [13] due to scaling violation. The data and Monte Carlo x distributions for low and high Q^2 kinematic regions are shown in figures 48 and 49 for $s = 8$.

¹⁵This is in addition to the dependence on F_2 on Q^2 already explained in section 6.1.3.

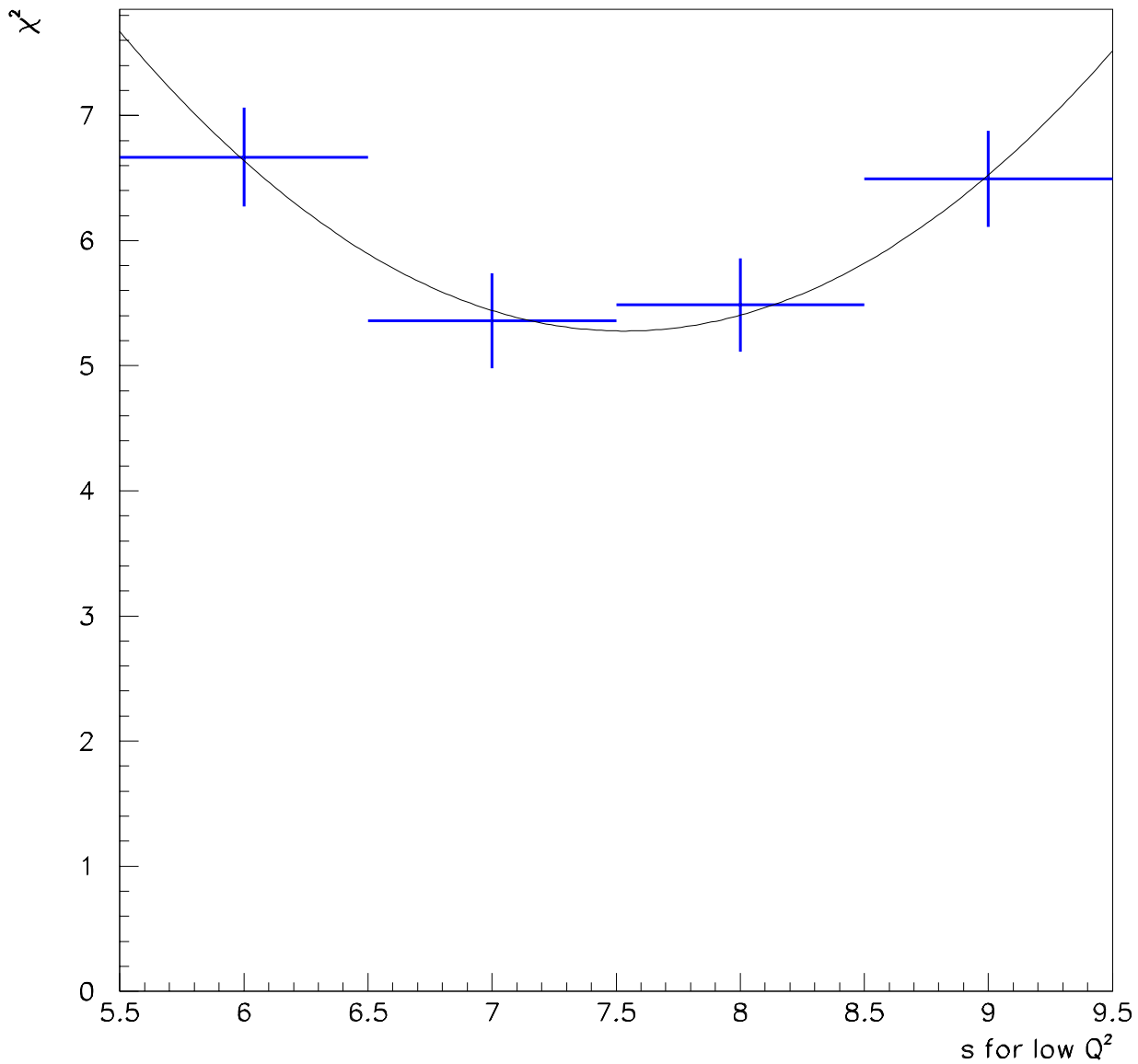


Figure 46: The χ^2 of the Monte Carlo fit to the data x distribution as a function of s for $50 < Q^2 < 100$.

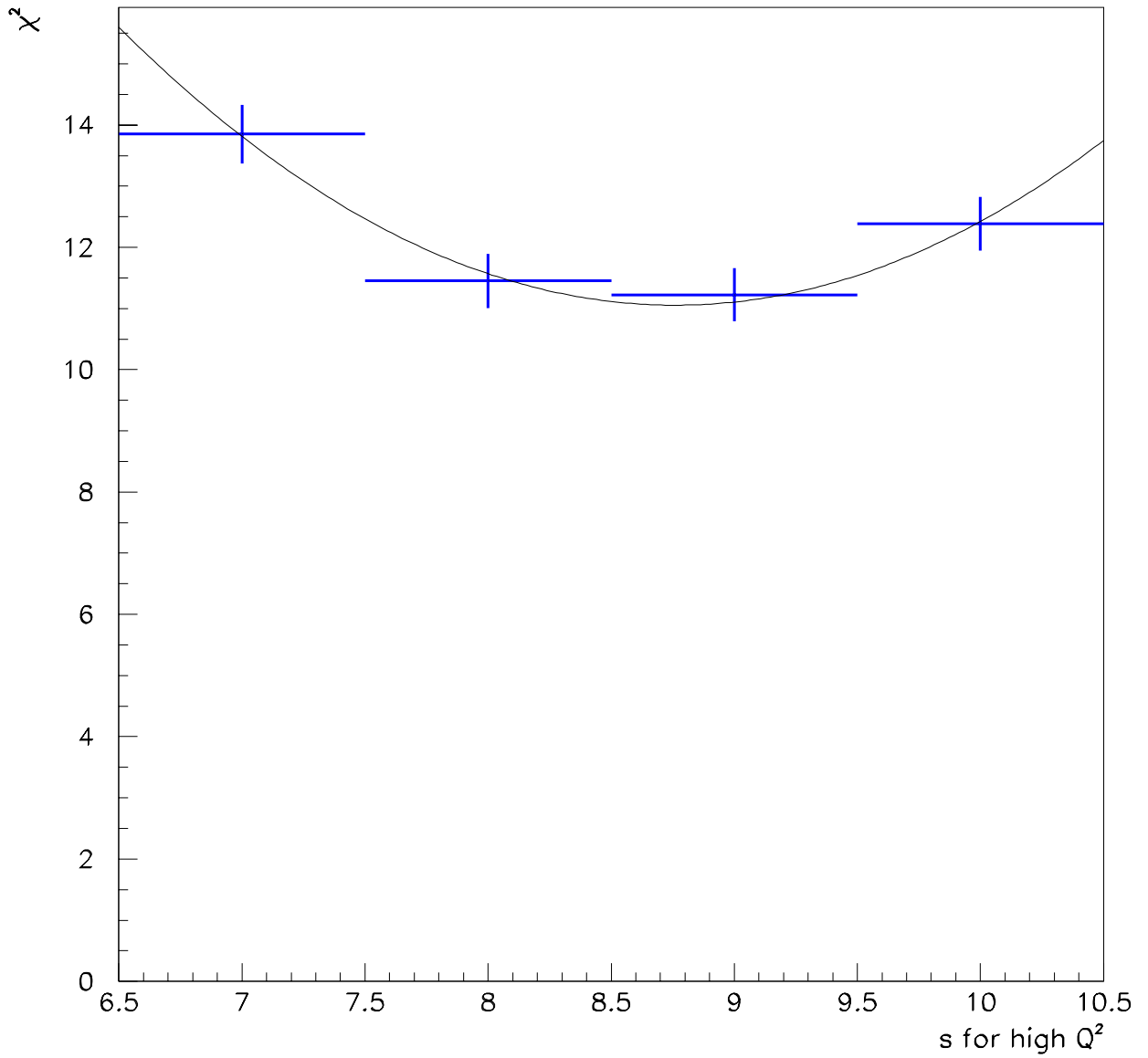


Figure 47: The χ^2 of the Monte Carlo fit to the data x distribution as a function of s for $100 < Q^2 < 400$.

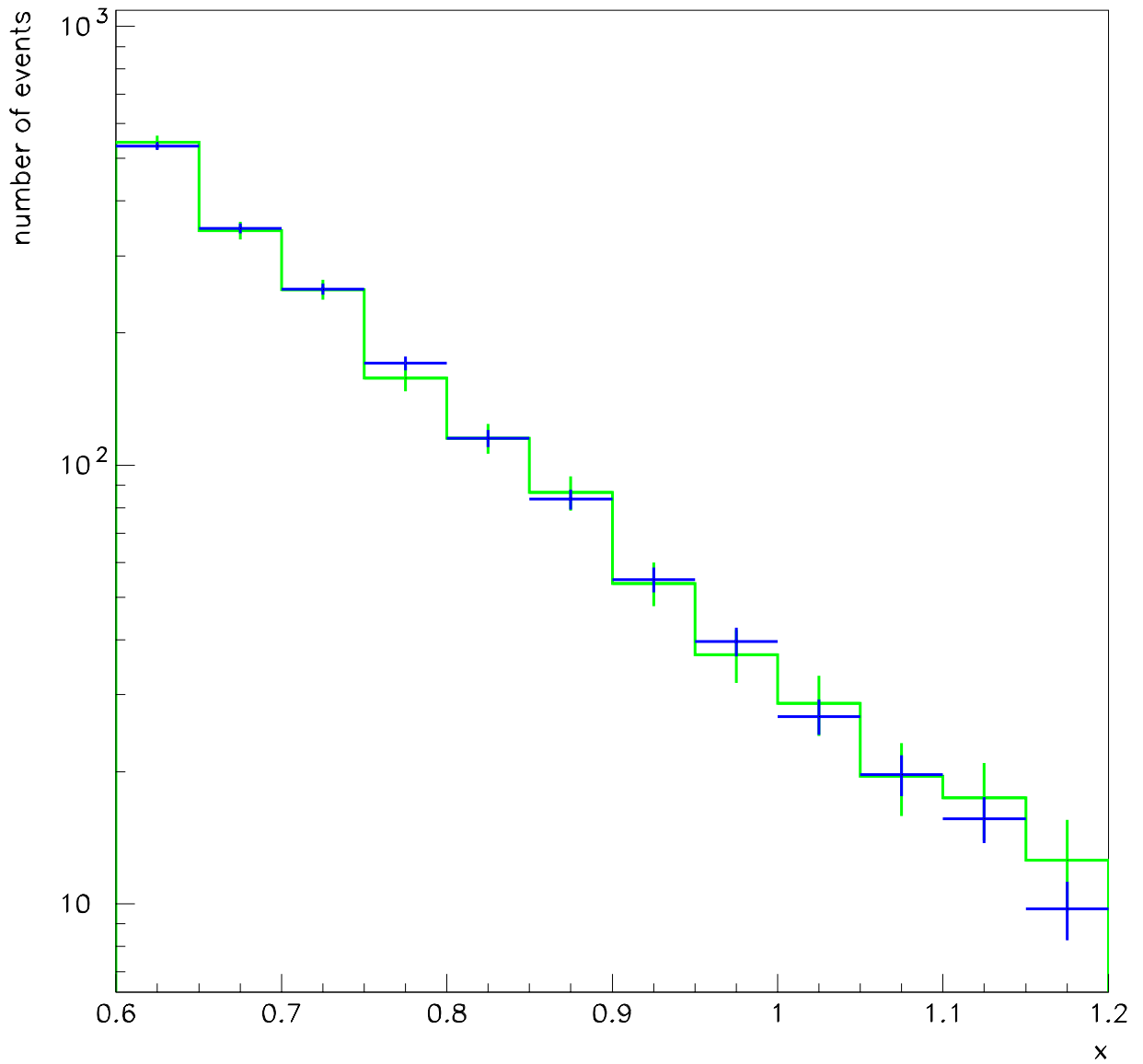


Figure 48: The x distribution in the data (solid histogram) and the exponentially falling F_2 model with input value of $s = 8$ for $50 < Q^2 < 100$ (GeV)².

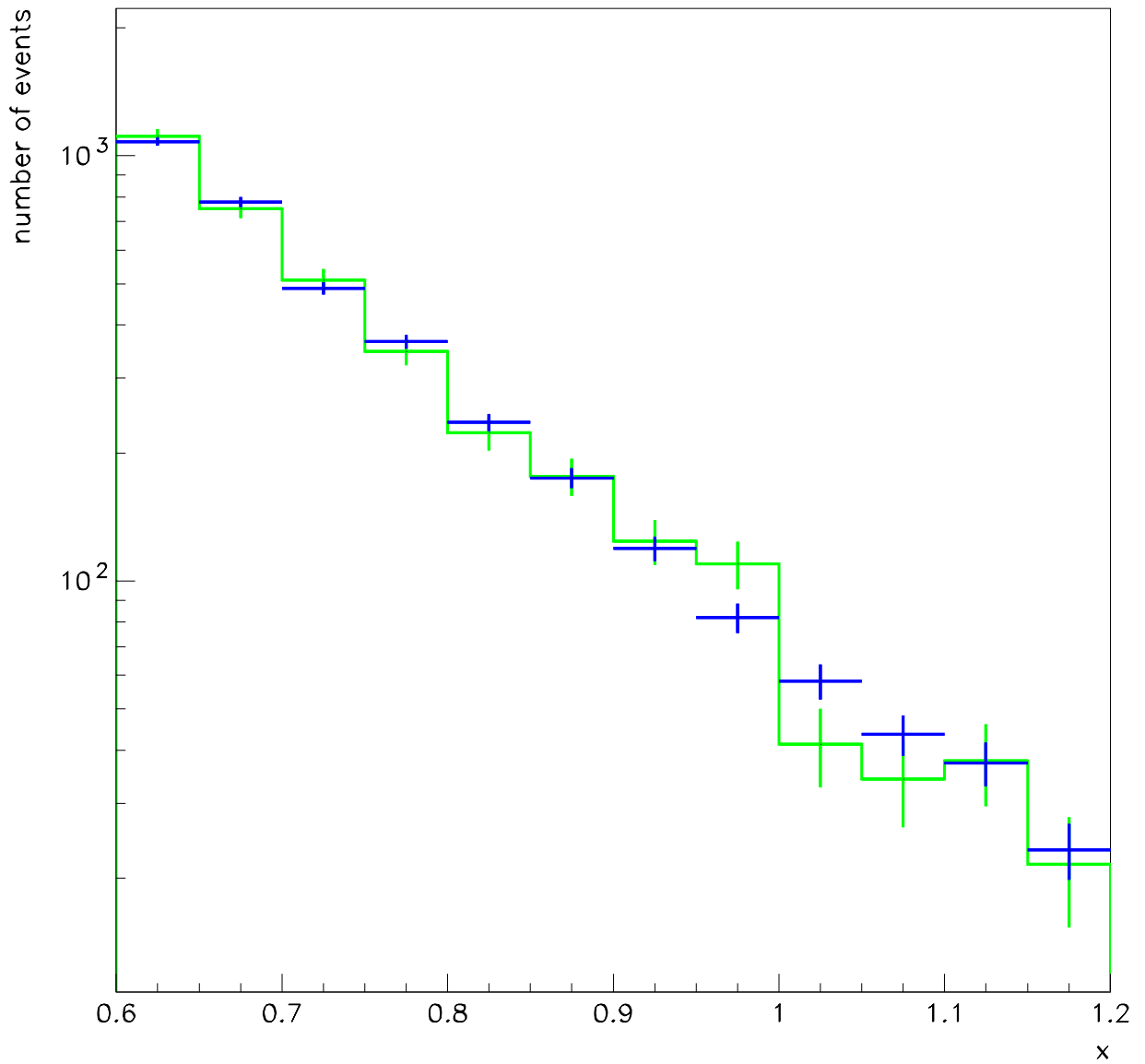


Figure 49: The x distribution in the data (solid histogram) and the exponentially falling F_2 model with input value of $s = 8$ for high $100 < Q^2 < 400$ (GeV)².

6.2 Systematic Errors

The measurement of s was described in the previous chapter. This measurement is based on a fit of the model explained in section 6.1.3 to the data x distribution. However, there are certain assumptions made to reconstruct x in the data events that are not simulated in the Monte Carlo. For example the energy scale of the experiment is assumed to be known exactly. The energy scale is determined from test beam measurements. However there is an uncertainty in the momentum of the test beam that stems from limited knowledge of the test beam magnets. These type of uncertainties affect the data entirely.

To estimate errors on the value of s , caused by these type of effects, first the source of the uncertainty, k , is identified. Then the following steps are taken to calculate the effect on s and F_2 .

- The spread, σ_k , on the variable k is estimated.
- The variable k is varied by $\pm r \times \sigma_k$ with different values of r in the data and the changed x distribution is reconstructed.
- The Monte Carlo x distribution with different values of s is fit to the changed data sample.
- The best fit s value for each r is found and $s(r)$ is fit to an appropriate functional form.

The error in s corresponding to the uncertainty in variable k is $s(\pm 1) - s(0)$.

6.2.1 Energy Scale Error

The muon and hadronic energies are normalized by comparing their measurement in the detector with the test beam momentum spectrometer. The energy scale uncertainty is therefore determined by the accuracy of test beam momentum measurement. The test beam momentum is known to within 1%. To measure the error on s from this uncertainty, the muon and hadronic energies in the data were simultaneously varied within $\pm 2\%$. The value of s for the best Monte Carlo fit was measured each time. The result of these fits is shown in figure 50.¹⁶ The function used to fit $s(\Delta E)$ is a third order polynomial. This allows for a turning point and accounts for asymmetric errors. The error in s for $\pm 1\%$ energy scale was found to be ± 0.2 .

6.2.2 Relative Calibration

The uncertainty in the relative calibration of the muon and hadronic energies is 0.6% [10]. To measure the error on s , a procedure similar to the previous section is followed but the muon and hadronic energies are varied with opposite signs. The error is calculated for a deviation of $\pm 0.3\%$ in the two energies. The error in s was found to be ± 0.1 .

6.2.3 Incoming Neutrino Angle

The incoming neutrino beam is assumed to be a parallel beam. This is because the longitudinal flight length of the neutrinos, $L > 1$ km, is much larger than the fiducial

¹⁶The errors are chosen just for the fit. The central value has no error to force the fit through this point.

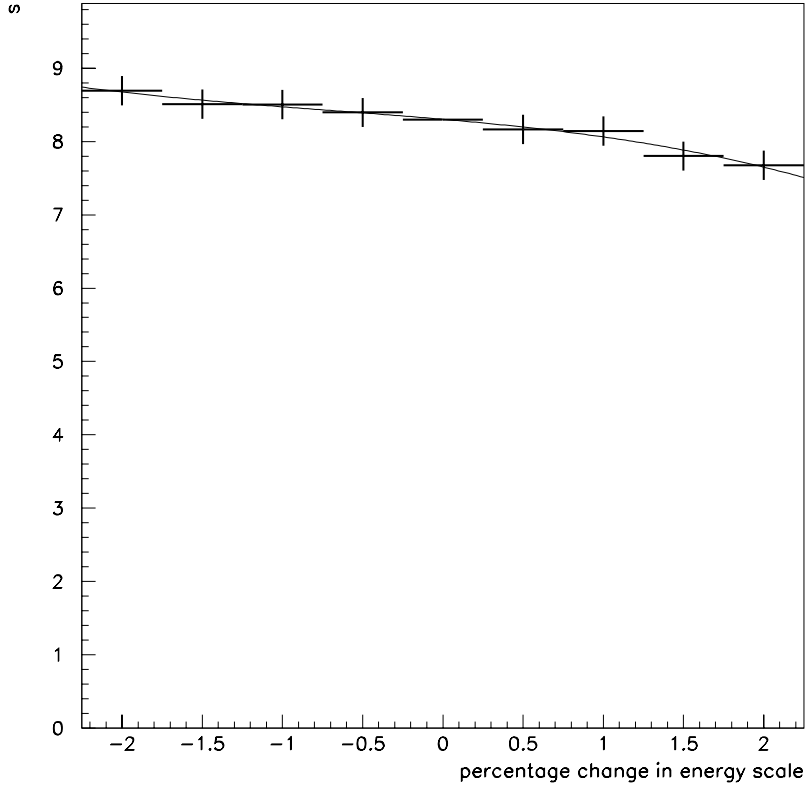


Figure 50: The value of s as a function of the percentage change in the energy scale.

volume of the detector, $R < 120$ cm. Therefore the angle of the incoming neutrinos is taken to be zero. To measure the effect of the small deviations in the neutrino angle, the average spread of the beam angle is estimated to be:

$$\bar{\theta}_\nu = \frac{0.6}{1000} = 0.6 \text{ mr} \quad (97)$$

which is the average neutrino transverse position divided by the minimum flight length.

To measure the uncertainty on s , the incoming neutrino angle was smeared by up to 0.2, 0.4, 0.6, 0.8, and 1 mr in the data. The s corresponding to the best fit was

determined and the value of s at 0.6 mr was used to find the systematic pull. This value was 8.2. The systematic error in s caused by this effect is therefore about ± 0.1 .

6.2.4 Outgoing Muon Angle

The detector resolution for the measurement of the outgoing muon angle is shown in table 3. This angle is known to better than 1 mrad. To estimate the uncertainty in s coming from the uncertainty in this angle, the angle was smeared in the data by 1 mrad and the new value of s was calculated. The error in parameter s was 0.1.

6.2.5 Hadronic Energy Mismeasurement

The hadronic energy measurement method, explained in section 4.2, was based on the deposited energy from counter number PLACE to counter number (SHEND-5). To measure possible mismeasurement, this method was compared with a formalism based on energy measurement in the 20 counters following PLACE. Figure 51 shows the difference in the energy from the two formalisms. We examined events with $x > 0.8$ which showed a difference of 11 GeV or more in E_{had} from the two formalisms. About 6% of events showed a difference. From the event display of chamber hits, about 60% of these proved to be mismeasurements. In these mismeasured events the hadronic shower seemed to be disjointed and a portion of it was after the counter (SHEND-5). The extra energy was therefore missed. These events were eliminated from the sample. For $0.6 < x < 0.8$, less than 2% showed a difference in E_{had} from the two formalisms. In this region, the number of events in each x bin was multiplied by 98.8% ($1 - 0.02 \times 0.6$) to correct for possible mismeasured events. The 98.8% correction

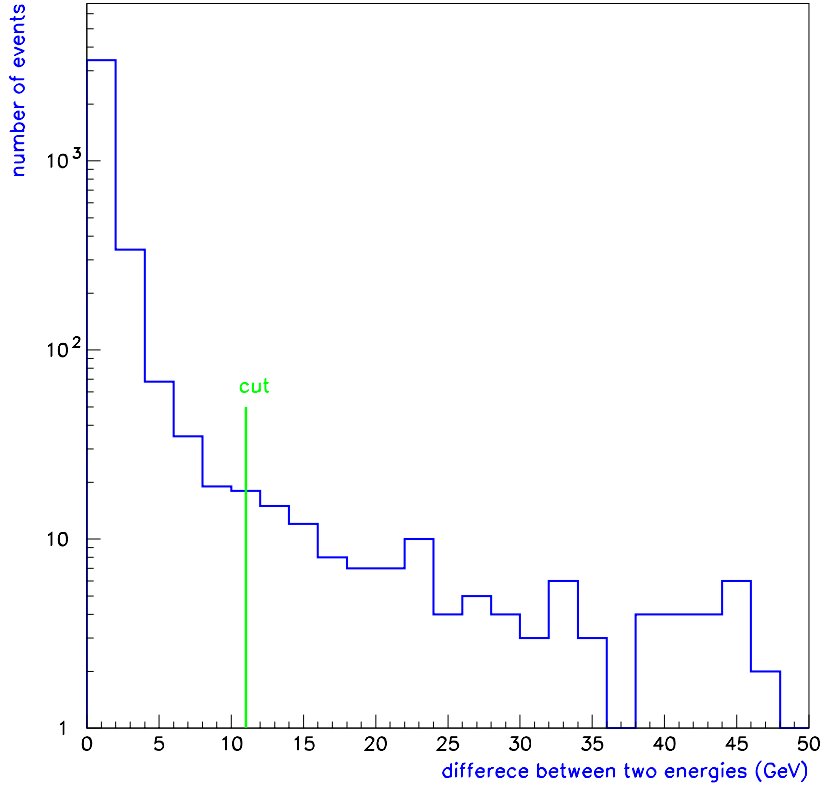


Figure 51: Difference between E_{had} measured in (SHEND-5) and 20-counter formalisms.

in these bins causes a change 0.04 in s . We use the corrected s and attribute an overestimated error of 0.1 in s from this procedure.

6.2.6 Radiative Corrections

The error from the radiative correction is determined by changing the amount of the correction by up to 2% for different x bins (section 5.3). The resulting error in s is 0.1.

6.2.7 Other Systematic Studies

The effect of bad hits on E_μ measurement.

A study was done to see if there are events where bad hits in the target or toroid chambers cause muon energy mismeasurement. The entire data sample in the kinematic region $x > 0.8$ was studied. Each individual chamber was eliminated from the data once and the momentum finding formalism was repeated without the chamber hit. This is done for the chambers in the target and the toroid. If the new momentum differed by more than 15% from the one determined using all chambers, that event was eliminated from the data sample. In more than four thousand events only 3 events were eliminated.

Large x events vs. run number.

During the course of the CCFR 1987-1988 run a few hundred runs were taken with a few thousands triggers in each run. A study was done to see if there are more large x events in certain runs than the others. If found this could have been an indication of bad measurement in that run. The run numbers for large x and all events are shown in figure 52. The ratio of the two plots is constant within error bars. There is no indication of a great number of large x events in a particular run.

Azimuthal distribution of large x events.

To see if the geometry of the beam line or the detector had any effect in x measurement, the muon azimuthal angle distribution at the event vertex was studied. This distribution was compared for large x events and for all events. The comparison is

shown in figure 53. The ratio plot shows that the muon azimuthal angle distribution of the large x events is the same as the rest of the events within errors.

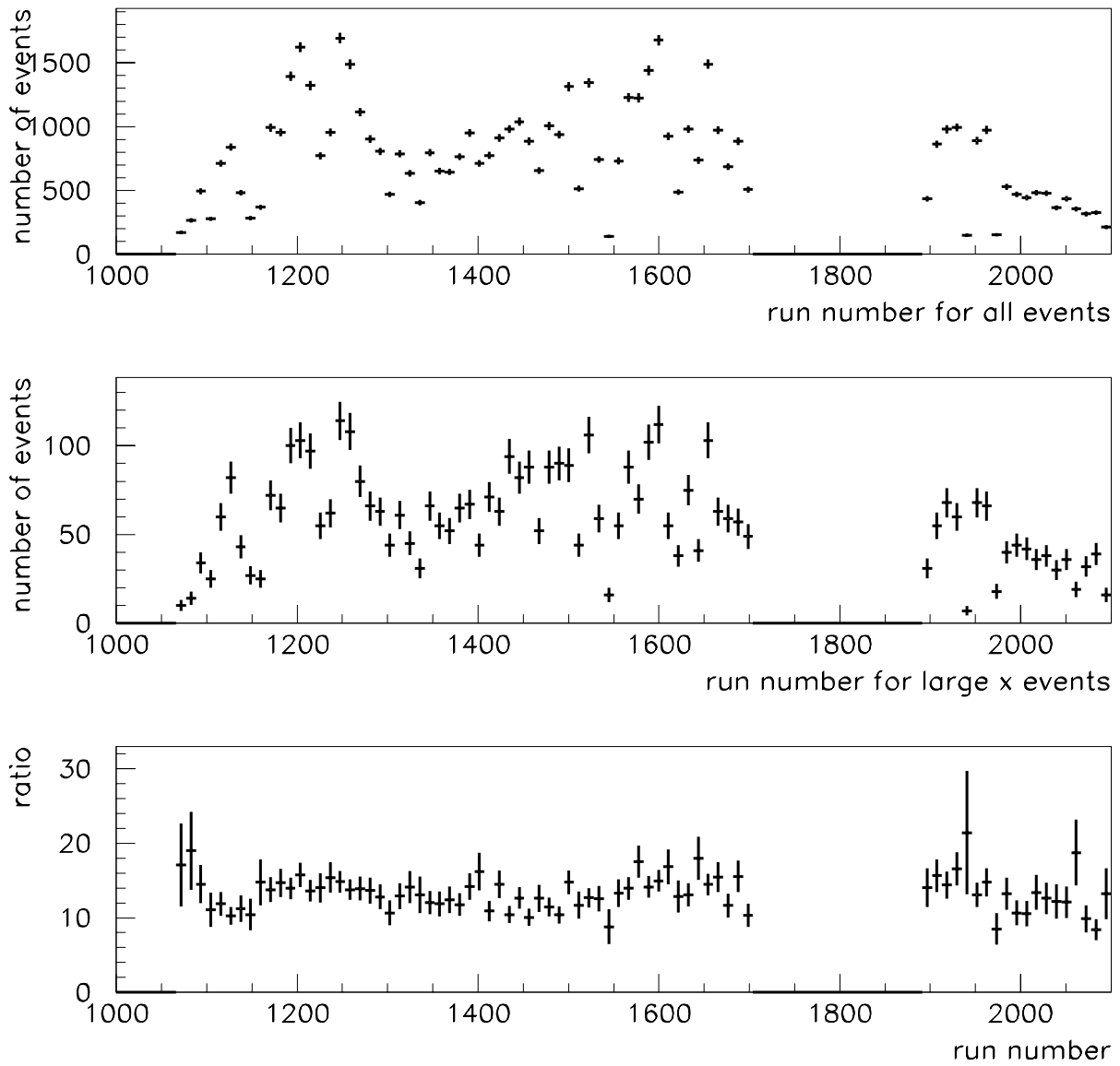


Figure 52: Number of event in run blocks for all events (top), for large x events (middle), and the ratio of the two (bottom).

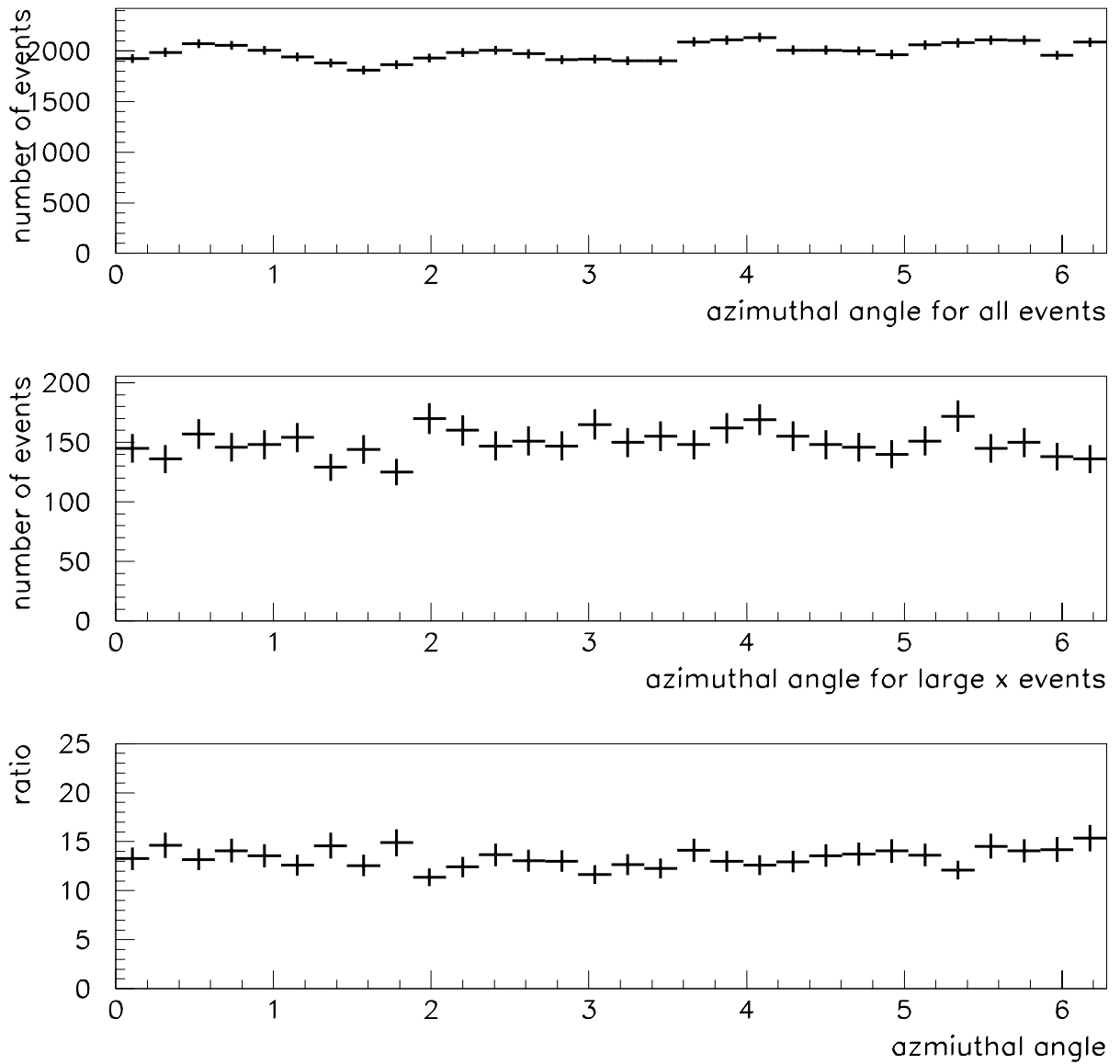


Figure 53: Muon azimuthal angle for all events (top) and for large x events (middle) and the ratio of the two (bottom).

6.2.8 Final Value of s

Table 6 shows all the the systematic errors on s . The total systematic error is obtained

Systematic Factor	error in s
energy scale	0.2
relative calibration	0.1
incoming neutrino angle	0.1
outgoing muon angle	0.1
hadronic energy mismeasurement	0.1
radiative corrections	0.1
TOTAL SYSTEMATIC ERROR	0.3

Table 6: Systematic errors.

by adding different errors in quadratures. The final value of s from the CCFR neutrino DIS data with all errors is:

$$s = 8.3 \pm 0.7 (stat.) \pm 0.3 (sys.). \quad (98)$$

6.2.9 Calculation of F_2

The parameter s and its errors in the exponentially falling F_2 model were determined in previous chapters. Once s is determined, the structure function F_2 can be calculated within the model. To do this, for $x < 0.75$, F_2 is considered as the following function:

$$F_2 = N f(x = 0.75, Q^2) \exp[-s(x - 0.75)] \quad (99)$$

This is the same function as equation 95 times a factor N representing the Monte Carlo normalization. Normally, the Monte Carlo is normalized to the same number of events in the data to find the value of s that minimizes the χ^2 of the fit to the

data. However to find out the error from this normalization and its correlation with the error in s , it is allowed to vary here. The χ^2 will then be a function of both s and N . At its minimum, the χ^2 can be expanded as a function of these two variables:

$$\chi^2 = \chi_0^2 + \frac{1}{2} \left[\frac{\partial^2 \chi^2}{\partial s^2} (\delta s)^2 + 2 \frac{\partial^2 \chi^2}{\partial s \partial N} (\delta s)(\delta N) + \frac{\partial^2 \chi^2}{\partial N^2} (\delta N)^2 \right] . \quad (100)$$

This expression can be written in matrix form as:

$$\chi^2 = \chi_0^2 + [\delta S_1 \quad \delta S_2] \left[\frac{1}{2} \frac{\partial^2 \chi^2}{\partial S_i \partial S_j} \right] \begin{bmatrix} \delta S_1 \\ \delta S_2 \end{bmatrix} , \quad (101)$$

where $S_1 \equiv s$ and $S_2 \equiv N$. The error matrix is:

$$M = \left[\frac{1}{2} \frac{\partial^2 \chi^2}{\partial S_i \partial S_j} \right]^{-1} . \quad (102)$$

The error in F_2 is then calculated as:

$$\delta F_2 = \sqrt{\left[\frac{\partial F_2}{\partial S_i} \right] [M_{ij}] \left[\frac{\partial F_2}{\partial S_j} \right]} . \quad (103)$$

There is very little correlation between errors in s and N . The dominant term in the error in F_2 comes from the error in s . Contour plots of χ^2 as a function of the change in s and the percentage change in N are shown in figure 54. The marked contour corresponds to about one unit of χ^2 which determines the errors in s and N . Plots of F_2 for $Q^2 = 80, 125(\text{GeV})^2$ are shown in figures 55 and 56. The bands show the value of F_2 calculated within the exponentially falling model. Two values of F_2 at $x = 0.65$ and 0.75 from the previous CCFR structure function analysis [13] are shown also. In both cases the large F_2 has been normalized to its value at $x = 0.65$ from [13]. The value of $F_2(x = 0.75)$ from [13] is about 5% lower than this analysis. This is mainly due to the fact that large x events are not generated in this reference.

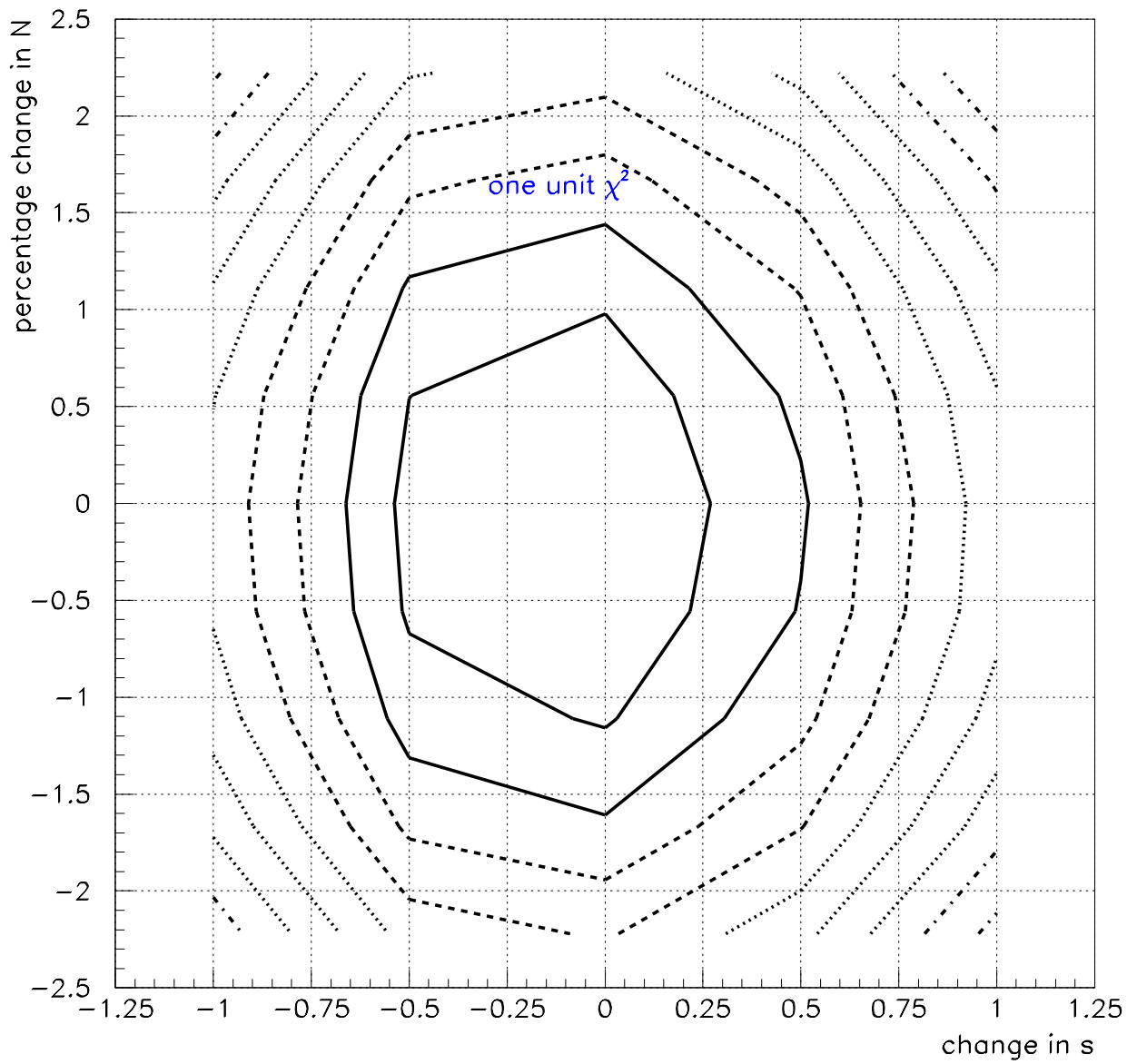


Figure 54: Contour plots of χ^2 as a function of the change in s and the percentage change in N .

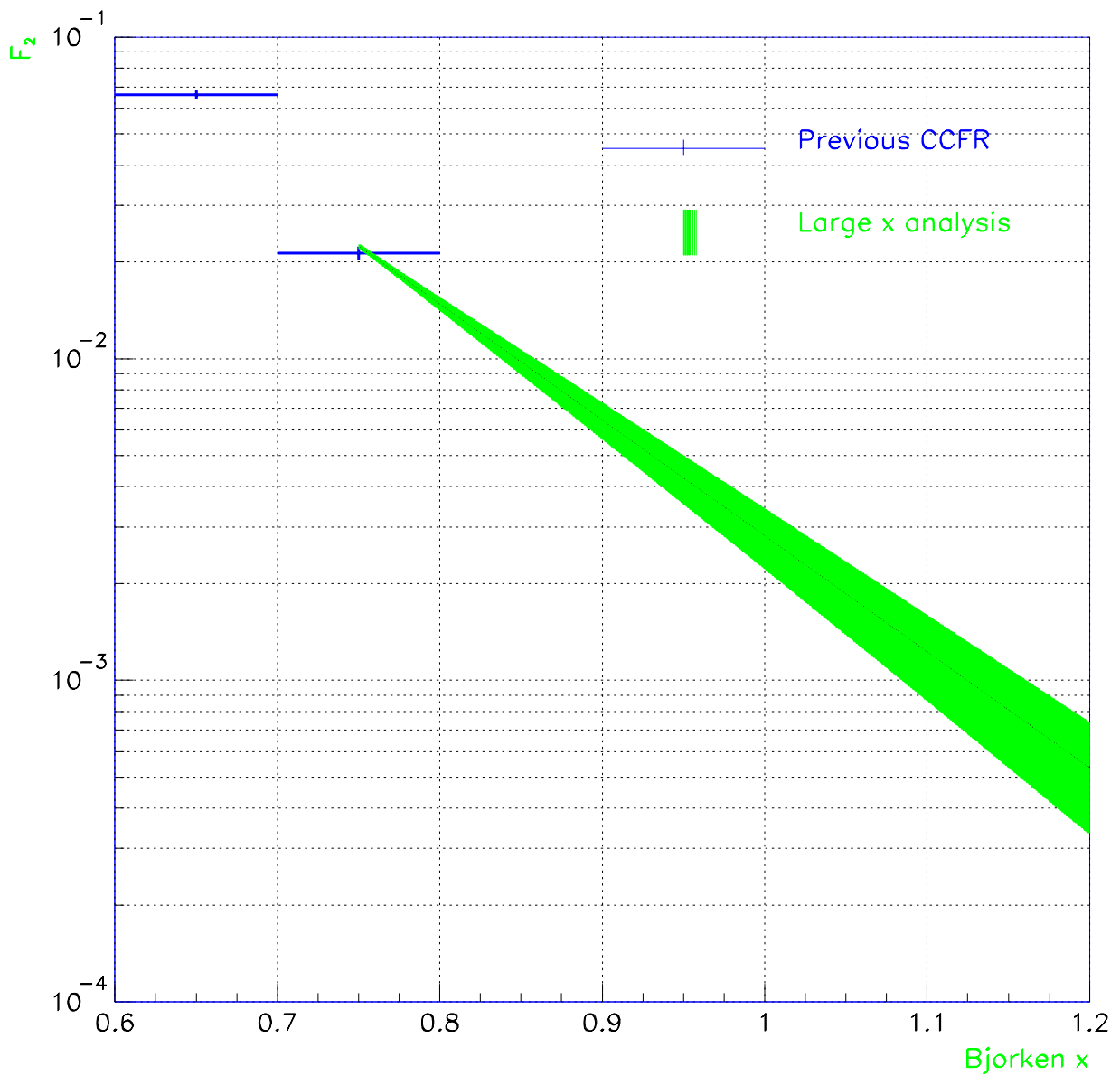


Figure 55: Calculated F_2 within the exponentially falling model. The band shows the prediction of the model for $x > 0.75$ and $Q^2 = 80 \text{ (GeV)}^2$.

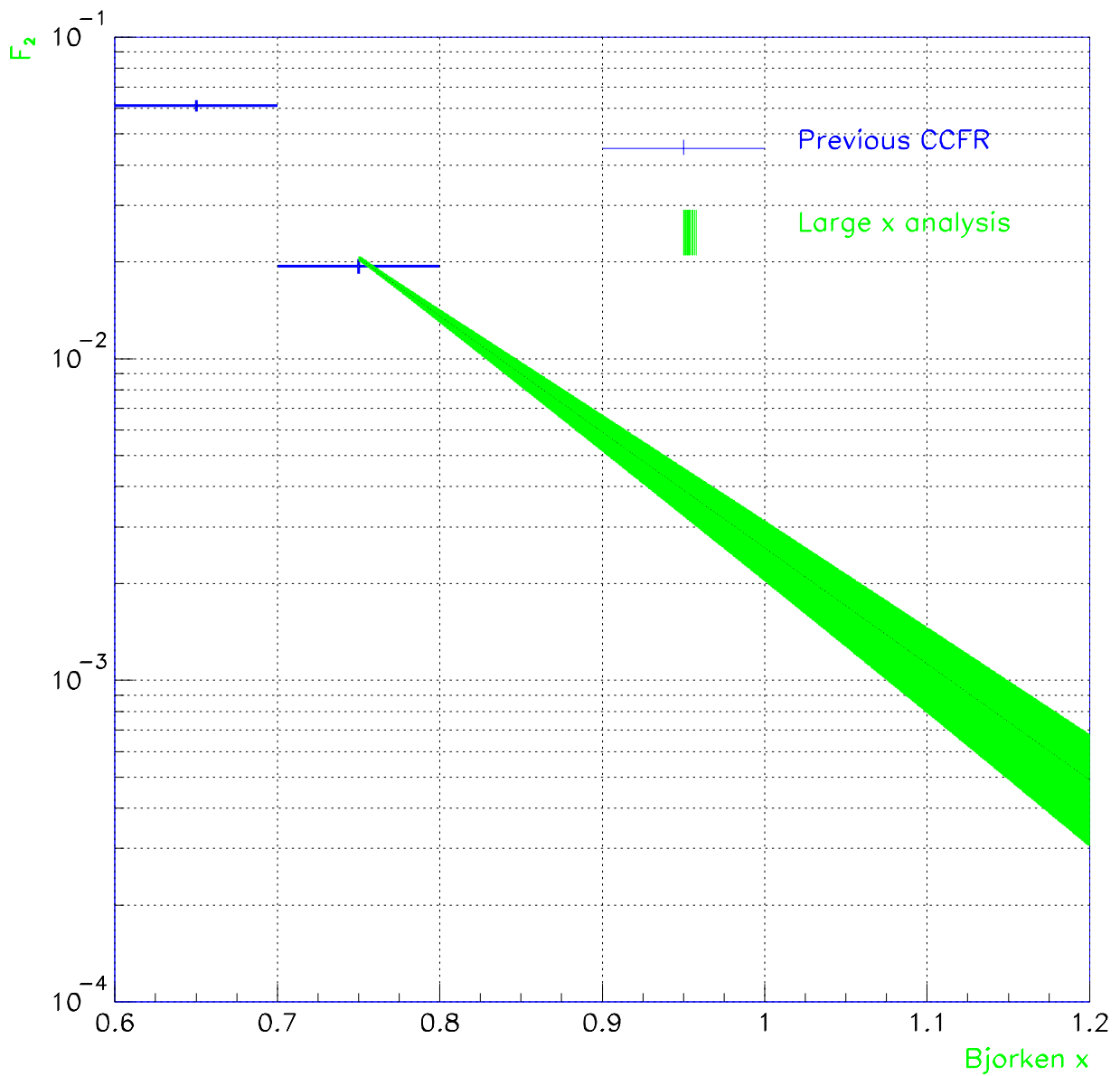


Figure 56: Calculated F_2 within the exponentially falling model. The band shows the prediction of the model for $x > 0.75$ and $Q^2 = 125 \text{ (GeV)}^2$.

6.3 Comparison With Theory and Other Measurements

6.3.1 Comparison of s

The value of the exponential slope, s , measured in this analysis has been predicted by some theoretical models and measured in two other experiments. Strikman and Frankfurt [22] predict this slope to be $s \approx 8 - 9$ based on few-nucleon correlations models (FNCM). This is in agreement with our data. Baldin *et al.* [24] predict a less steep slope of $s \approx 6$. This prediction is based on a fit to the Dubna data on pion production at $x_F > 1$ using the “cumulative number” as a scaling variable. The same value of $s \approx 6$ is predicted by Nikoiforov *et al.* [26] based on the extreme assumption that a heavy nucleus, with atomic number A , can be considered as a bag of $3A$ quarks. These two models do not agree with our data.

Measurement of s based on electron scattering off aluminum target at $Q^2 = 8, 10$ (GeV)², from SLAC E133 data [2], indicates $s \approx 7 - 8$. This result is in agreement with our measured value.

The BCDMS collaboration reports a value of $s = 16.5 \pm 0.5$ in muon on carbon DIS at $Q^2 > 50$ (GeV)². Our measured s is different from this result.

6.3.2 Comparison of F_2

In this analysis the measurement of s corresponds to a value of $F_2^{\nu Fe}(x = 1) \sim 2 \times 10^{-3}$. Scaled down to account for the $\frac{5}{18}$ th rule (equation 60) to compare with the charged lepton F_2 , this corresponds to $\sim 6 \times 10^{-4}$.

The value of $F_2(x = 1)$ from the SLAC E133 [2] measurement is about $\sim 1.2 \times 10^{-3}$

for $Q^2 = 10 \text{ (GeV)}^2$. To compare this with our result, one should correct for the scaling violation that causes F_2 to drop from its value at $Q^2 = 10 \text{ (GeV)}^2$ to that at $Q^2 > 50 \text{ (GeV)}^2$. The extrapolation of the SLAC $F_2(x = 1, Q^2 = 10)$ via the factor, $(Q^2)^{f+g_x}$ (section 6.1.3), gives $F_2(x = 1) \sim 7 \times 10^{-4}$. The errors on F_2 from both experiments are about 15-20%. The agreement is not surprising since the s values are consistent.

In the BCDMS analysis [1], F_2 is reported to be $F_2^{\mu C}(x = 1) \approx 1.2 \times 10^{-4}$. The errors on F_2 from both experiments are about 15-20%. Nuclear effects are believed to cause, at the most, a 20% difference in different heavy nuclei. The value from this thesis seems to be different from that of BCDMS.

References

- [1] BCDMS collaboration, *Z. Phys.* C63 29 (1994).
- [2] S. Rock, et al, *PR D*46, 24(1992).
- [3] E. J. Monitz, *Phys. Rev.* 26, 445 (1971).
- [4] A. Bodek and J. L. Ritchie, *Phys. Rev.* D24(1981) 1200.
- [5] W.C. Leung, *Nucleon Structure Functions from High Energy ν -Iron Interactions at the Fermilab Tevatron*, PHD thesis, Columbia University, 1992.
- [6] S.A. Rabinowitz, *Opposite Sign Dimuon Production in Neutrino Interactions at the Fermilab Tevatron*, PHD thesis, Columbia University, 1992.
- [7] S.A. Rabinowitz, *et al.*, *Phys. Rev. Lett.* 70 134 (1993).
- [8] P.Z. Quintas, *A Nucleon Structure Functions from ν -Fe Interactions and a Study of Valence Quark Distribution*, PHD thesis, Columbia University, 1992.
- [9] P.Z. Quintas, *et al.*, *Phys. Rev. Lett.* 71 1307 (1993).
- [10] A.O. Bazarko, *Determination of the Strange Quark Distribution from a Next-to-Leading-Order QCD Analysis of Neutrino and Antineutrino Production of Charm*, PHD thesis, Columbia University, 1994.
- [11] A.O. Bazarko, *et al.*, *Z. Phys.* C65 189 (1995).

- [12] B.J. King, *A Precise Measurement of the Weak Mixing Angle in Neutrino-Nucleon Scattering*, PHD thesis, Columbia University, 1994.
- [13] W.G. Seligman, *A Next-to-Leading order QCD Analysis of Neutrino-Iron Structure Functions at The Tevatron*, PHD thesis, Columbia University, 1997.
- [14] W.G. Seligman, *et al.*, Accepted by Phys. Rev. Lett. (1997).
- [15] A. Romosan, *High Statistics Search for $\nu_\mu(\bar{\nu}_\mu) \rightarrow \nu_e(\bar{\nu}_e)$ Oscillations in the Small Mixing Angle Regime*, PHD thesis, Columbia University, 1997.
- [16] A. Romosan *et al.*, Phys. Rev. Lett. 78 2912 (1997).
- [17] K.S. McFarland *et al.*, Phys. Rev. Lett. 75 3993 (1995).
- [18] Greiner and Schafer, *Quantum Chromodynamics*, Springer 1995.
- [19] W.Greiner and J.A. Maruhn, *Nuclear Models.*, Springer 1995.
- [20] C. Itzikson and J.B. Zuber, *Quantum Field Theory*, McGraw-Hill, 1987.
- [21] D.F. Geesaman, K. Saito, and, A.W. Thomas, *Quantum Field Theory The Nuclear EMC Effect*, Annu. ReV. Part. Sci. 1995. 45:337-90
- [22] L. Frankfurt and M.Strikman, Phys. Rep. 76 (1981) 215
- [23] L.A. Kondratyuk and M.Zh. Shmatikov, Yad. Fiz. 41(1985) 222
- [24] A.M. Baldin, proc. conf. on Extreme States in Nuclear States (Dresden, 1980), vol. 2, p. 1.

- [25] A.M. Baldin, *et al.*, Sov. J. Nucl. Phys. 18 (1974) 41
- [26] Nikoiforov, *et al.*, Phys. Rev. C 22 (1980) 700.
- [27] D. Yu. Bardin, *et al.*, JINR-E2-86-260.
- [28] R. M. Barnett *et al.* (Particle Data Group), Phys. Rev. Lett. D54 (1996).
- [29] CDHSW collaboration, P. Berg *et al.*, Z. Phys. C49 187 (1991).
- [30] A.J. Buras and K.J.F. Gaemers (CERN), Nucl. Phys. B132, 249 (1978)
- [31] F. Halzen and A.D. Martin, *Quarks and Leptons* John Wiley & Sons (1984).
- [32] B.J. King, *et al.*, Nucl. Instrum. Methods A302: 254-260.
- [33] W.K. Sakumoto, *et al.*, Nucl. Instrum. Methods A294: 179-192.
- [34] G. Koizumi; FERMILAB-TM-0780 (1987).
- [35] A. Chikatur, *et al.* (CCFR Collaboration), Z. Phys. C74 279 (1997).